


Winter 2007

# Development of Fast, Distributed Computational Schemes for Full Body Bio-Models and Their Application to Novel Action Potential Block in Nerves Using Ultra-Short, High Intensity Electric Pulses

Ashutosh Mishra  
*Old Dominion University*

Follow this and additional works at: [https://digitalcommons.odu.edu/ece\\_etds](https://digitalcommons.odu.edu/ece_etds)

 Part of the [Biomedical Engineering and Bioengineering Commons](#), and the [Electrical and Computer Engineering Commons](#)

---

## Recommended Citation

Mishra, Ashutosh. "Development of Fast, Distributed Computational Schemes for Full Body Bio-Models and Their Application to Novel Action Potential Block in Nerves Using Ultra-Short, High Intensity Electric Pulses" (2007). Doctor of Philosophy (PhD), dissertation, Electrical/Computer Engineering, Old Dominion University, DOI: 10.25777/vegt-r564  
[https://digitalcommons.odu.edu/ece\\_etds/112](https://digitalcommons.odu.edu/ece_etds/112)

This Dissertation is brought to you for free and open access by the Electrical & Computer Engineering at ODU Digital Commons. It has been accepted for inclusion in Electrical & Computer Engineering Theses & Dissertations by an authorized administrator of ODU Digital Commons. For more information, please contact [digitalcommons@odu.edu](mailto:digitalcommons@odu.edu).

DEVELOPMENT OF FAST, DISTRIBUTED COMPUTATIONAL  
SCHEMES FOR FULL BODY BIO-MODELS AND THEIR  
APPLICATION TO NOVEL ACTION POTENTIAL BLOCK IN  
NERVES USING ULTRA-SHORT, HIGH INTENSITY ELECTRIC  
PULSES

by

Ashutosh Mishra  
M.S. May 2003, Old Dominion University

A Dissertation Submitted to the Faculty of Old Dominion University in Partial  
Fulfillment of the Requirements for the Degree of

DOCTOR OF PHILOSOPHY  
ELECTRICAL AND COMPUTER ENGINEERING  
OLD DOMINION UNIVERSITY  
December 2007

Approved by:

\_\_\_\_\_  
Ravindra P. Joshi (Director)

\_\_\_\_\_  
Linda Vahala (Member)

\_\_\_\_\_  
Frederic D. McKenzie (Member)

\_\_\_\_\_  
Mujde Erten-Unal (Member)

## Abstract

DEVELOPMENT OF FAST, DISTRIBUTED COMPUTATIONAL SCHEMES FOR FULL BODY BIO-MODELS AND THEIR APPLICATION TO NOVEL ACTION POTENTIAL BLOCK IN NERVES USING ULTRA-SHORT, HIGH INTENSITY ELECTRIC PULSES

Ashutosh Mishra  
Old Dominion University, 2007  
Director: Dr. R.P. Joshi

An extremely robust and novel scheme for computing three-dimensional, time-dependent potential distributions in full body bio-models is proposed, which, to the best of our knowledge, is the first of its kind. This simulation scheme has been developed to employ distributed computation resources, to achieve a parallelized numerical implementation for enhanced speed and memory capability. The other features of the numerical bio-model included in this dissertation research, are the ability to incorporate multiple electrodes of varying shapes and arbitrary locations. The parallel numerical tool also allows for user defined, *current or potential* stimuli as the excitation input. Using the available computation resources at the university, a strong capability for extremely large bio-models was developed. So far a maximum simulation comprised of 6.7 million nodes has been achieved for a “full rat bio-model” with a 1 mm spatial resolution at an average of 30 seconds per iteration.

The ability to compute the resulting potential distribution in a full animal body allows for realistic and accurate studies of bio-responses to electrical stimuli. For example, the voltages computed from the full-body models at various sites and tissue locations could be used to examine the potential for using nanosecond, high-intensity, pulsed electric fields for blocking neural action or action potential (AP) propagation. This would be a novel, localized, and reversible method of controlling neural function without tissue damage. It could potentially be used in “electrically managed pain relief,” non-lethal incapacitation, and neural/muscular therapy.

The above concept has quantitatively been evaluated in this dissertation. Specifically, the effects of high-intensity (kilo-Volt), ultra-short (~100 nanosecond) electrical pulses have been evaluated, and compared with available experimental data. Good agreement with available data is demonstrated. It is also shown that nerve membrane electroporation, brought about by the high-intensity, external pulsing, could indeed be instrumental in halting AP propagation. Simulations based on a modified distributed cable model to represent nerve segments have been used to demonstrate a numerical “proof-of-concept.”

This dissertation is humbly dedicated to my parents – Asha & Anjani. You are the world I know, the name I worship and all the love I need. My darling sister – Anubha, who means the life to me and has shown resilience and personal strength rarely found in mere mortals! I thank you for your unconditional acceptance, patience and my being.

-Ashutosh, 2007

## ACKNOWLEDGEMENTS

This dissertation would not be complete without the acknowledgement of significantly superior individuals that have given me their time. The first and foremost of this group is my advisor – Dr. R.P. Joshi. His faith in my abilities, generosity and the relentless drive that helped me push my own envelop are the prime-movers of this dissertation. Nothing would have been possible without his patience, understanding and the sense of humor. I shall remain forever in awe of his stature.

I would also like to express my profuse gratitude to Dr. L. Vahala, Dr. R. McKenzie, and Dr. M. Erten-Unal, for consenting to be on my dissertation advisory committee. This is also an opportune moment to thank Dr. V. Lakdawala for his words of encouragement and guidance and members of the staff – Linda and Hero – for all their support help and the food!

Outside the environs of the campus there is an active group of people who kept me laughing and driven. They are: Steve Corson, Tim Goodale, Jack Bloom, Noreen, Vissu and Rebekka Althouse and all the regulars at O’Sullivans. Ladies and gentlemen, you are my friends for life and I am a better man due to you.

Finally, I bow my head to Dr. D. K Pandey and Mrs. Snehlata Pandey, who have been my family away from home.

Thank you everyone!

## TABLE OF CONTENTS

LIST OF FIGURES .....	ix
LIST OF TABLES.....	xii
CHAPTER I.....	1
INTRODUCTION .....	1
1.1 BIOELECTRICS – AN OVERVIEW .....	1
1.2 THE ROLE AND ADVANTAGES OF BIO-MODELING.....	2
1.3 OVERALL SCOPE AND SPECIFIC GOALS OF THIS RESEARCH WORK .....	2
CHAPTER II .....	5
LITERATURE REVIEW AND PERTINENT BACKGROUND.....	5
2.1 OVERVIEW .....	5
2.2 FULL BODY MODELING SCHEME .....	6
2.2.1 Intrinsic hurdles in full body modeling.....	9
2.2.1.1 Model resolution.....	11
2.2.1.2 Tissue parameters .....	11
2.2.1.3 Excitation (stimulus) locations and form.....	11
2.3 NEURAL SIGNALS AND BLOCK SCHEMES.....	14
2.3.1 Nerve segment structure and key terms .....	15
2.3.1 Action Potential .....	16
2.3.2 Action Potential conduction block.....	18
2.3.2.1 Electroporation .....	21
2.3.3 Proposed Action Potential conduction block scheme .....	22
2.3.4 Synaptic process and possible AP block site .....	24
2.3.5 More recent modes and studies.....	25
CHAPTER III.....	27
MODELING DETAILS AND NUMERICAL IMPLEMENTATION .....	27
3.1 FULL-BODY MODELING SCHEME.....	27
3.1.1 Input Format Details .....	27
3.1.2 Proposed Modeling Scheme.....	31
3.1.2.1 Matrix Sparsity and its Significance.....	37
3.1.2.2 Solution Scheme Overview for the Full Body Models.....	39
3.1.3 Distributed Algorithm Details.....	42

3.1.3.1 Algorithm Process Flow Diagram .....	43
3.1.3.2 Coefficient Matrix Setup in Compressed Row Storage Scheme .....	43
3.2 MODELING NEURAL TRAFFIC INTERRUPTION METHODS.....	47
3.2.1 Distributed Cable Model for Representing the Unmyelinated Nerve Segment .....	47
3.2.2 Distributed Cable Model for Representing the Myelinated Nerve Segment .....	49
3.2.2 Modified HH Model for Membrane Conductance Modulation .....	53
3.2.3 Membrane Electroporation Effects .....	54
CHAPTER IV .....	58
RESULTS AND DISCUSSION.....	58
4.1 DISTRIBUTED MODELING SCHEME.....	58
4.1.1 Input data visualization methods.....	58
4.1.2 Validating the full-body modeling scheme.....	61
4.1.2.1 Saline sphere with two parallel planar disc electrodes.....	61
4.1.2.2 Saline sphere with symmetric axially located electrodes.....	63
4.1.2.3 Saline brick with an air pocket.....	64
4.1.3 Preliminary results highlighting current density computations.....	65
4.1.4 Distributed process grid size and cluster load impact.....	68
4.1.5 Reducing fill-in during coefficient matrix factorization.....	70
4.1.6 Simulation results for a complex multi-tissue whole body model.....	71
4.1.6.1 Rat model with cross-diagonally grounded paws.....	72
4.1.6.2 Monkey head with planar electrodes.....	78
4.1.6.3 Significantly larger rat model.....	80
4.1.7 Comparing the symmetric and asymmetric modeling schemes.....	81
4.2 NERVE SEGMENT MODELING AND ACTION POTENTIAL (AP) BLOCK.....	84
4.2.1 Visualizing the action potential.....	84
4.2.2 AP propagation velocity.....	86
4.2.3 Conduction block using continuous electric stimuli (DC/AC).....	87
4.2.4 Modifying the shunt conductance.....	90
4.2.5 Application to multi-branch nerve segments.....	94
4.2.6 Experimental AP inhibition and validation.....	95
4.2.7 More recent observations that may support alternative AP block mechanisms.....	98
CHAPTER V .....	99
CONCLUSIONS AND SUGGESTIONS FOR FUTURE WORK.....	99
5.1 INTRODUCTION .....	99

5.2 FULL BODY MODELING .....	99
5.3 MODELING ACTION POTENTIAL AND CONDUCTION BLOCK .....	102
5.4 SCOPE FOR FUTURE WORK AND EXTENSION .....	104
5.5 EXTENDING TO MICRO-LEVEL SYSTEMS (E.G., CELL CLUSTERS) .....	107
5.5.1 Low intensity electric field cases .....	109
5.5.2 High intensity electric field cases .....	111
5.5.2 Summarizing the cell cluster .....	112
REFERENCES .....	114
APPENDIX .....	122
A.1 CONVERTING INDEX TO COORDINATES: .....	122
A.2 SYMMETRIC MODELING SCHEME: .....	123
A.3 SPARSE MATRIX STORAGE (COMPRESSED ROW FORMAT) .....	125
A.4 THE COEFFICIENT MATRIX IN COMPRESSED ROW FORMAT .....	126
CURRICULUM VITA .....	128



## LIST OF FIGURES

1.	Illustration showing the entry of PI into the PNM .....	8
2.	Cross-sectional representation of human skin tissue .....	10
3.	Typical Mammalian neuron (myelinated).....	16
4.	Typical Mammalian neuron (unmyelinated).....	16
5.	Representation of a cell membrane section.....	22
6.	Snapshots of pore formation in the DOPC bilayer.....	23
7.	Major elements in prototypical synaptic process.....	24
8.	Sample volumetric data set with the tissue cell indexing scheme.....	28
9.	Visualization of a sample raw data file of a rat.....	29
10.	Cross-sections of the rat at different depths.....	31
11.	Schematic of the discretized electrical model.....	32
12.	Simplified schematic to highlight the nodal links and node indexing.....	34
13.	Non-zero entries in case of a 1000 node, saline brick model.....	37
14.	Example of fill-in with and without reordering .....	41
15.	Process flow diagram for the distributed scheme of full body modeling .....	45
16.	Equivalent circuit representing the cable line model for the unmyelinated nerve segment.. .....	48
17.	Physical structure and Equivalent circuit of a myelinated nerve segment .....	50
18.	Action potential propagation in a 23.8 $\mu$ m diameter nerve segment .....	52
19.	Schematic for the modified cable model .....	54
20.	Action potential propagation block a 23.8 $\mu$ m diameter nerve segment .....	55
21.	Sketch of pores created on the nerve membrane by the external voltage.....	56
22.	Two forms of volumetric representation of the data.....	58
23.	Tissue layout present at different depths.....	59
24.	Tissue layout in a human head as visible in three orientations.....	60
25.	Two-Dimensional projection for the geometry used in the second validation case .....	61
26.	Current response and Potential profile to the FIRST validation test case .....	62
27.	Solid rendered saline sphere .....	63
28.	Potential profile & current response for the second validation case .....	64
29.	Saline Brick with air slab and the its response .....	64
30.	Potential profile for layer 11 in the x-y orientation for saline sphere .....	65

31.	Potential profile for layer 11 in the Y-Z orientation for saline sphere.....	66
32.	Current density components for saline sphere .....	67
33.	Timing diagram for the rat model for different process grid sizes during peak load hour.....	68
34.	Timing diagram for the rat model for different process grid sizes during off peak hour.....	69
35.	Profile for the applied potential pulse for the rat model.....	72
36.	Wire mesh rendered rat model.....	73
37.	Simulated potential profile at two slices for small rat model.....	75
38.	Computed conduction current density for small rat model.....	76
39.	Central slice conduction current density in each orientation.....	77
40.	A semi-transparent solid rendered plot showing the outer geometry in the monkey head model.....	78
41.	Potential contours for the monkey head model.....	79
42.	Potential contours for the LARGE rat model.....	80
43.	Average computation time per time iteration with symmetric method.....	81
44.	Three forms of visual representation of the action potential.....	84
45.	Computed velocity dependence upon the axon diameter for unmyelinated nerves.....	85
46.	AP block with DC pulse .....	87
47.	AP block with AC interrupt signal .....	88
48.	Minimum shunt conductance required for AP block in unmyelinated nerve segments as a function of number of nodes where the conductance was modulated.....	89
49.	Minimum shunt conductance required for AP block in myelinated nerve segments as a function of number of nodes where the conductance was modulated.....	90
50.	Angular pore density variation to e-fields.....	91
51.	Strength-duration curves for axon of different diameters for achieving minimum $G_{shunt}$ .....	92
52.	A sample multi-branch layout.....	93
53.	AP initiation and block using electroporation in a multi-segment unmyelinated nerve .....	94
54.	Schematic of experimental rat setup that was simulated .....	95
55.	Computed electric field along the spinal region along the entire length of the rat model .....	96

56.	Alternative physical model for Na <sup>+</sup> channels .....	102
57.	Voronoi networks with different disorder parameter.....	107
58.	Distributed representation for the electrical analysis at cellular level.....	107
59.	Simulation schematic showing an all-tissue and cell clusters .....	108
60.	Membrane Potential and Electric field for homogenous tissue system.....	109
61.	A 550 ns snapshot of the cell cluster indicating porated cells .....	109
62.	S-D curves for cell clusters with various distortion parameters and that for a single spherical cell.....	111

## LIST OF TABLES

1. AC block frequency range for good and fail AP block in an unmyelinated nerve segment .....	20
2. Electrical parameters for various constituent tissues .....	33
3. Comparative figures for fill-in with and without reordering .....	70
4. Computational statistics for the symmetric solution scheme .....	82
5. Shunt conductance with standard electric field and pulse width combinations .....	92

# Chapter I

## Introduction

### 1.1 Bioelectrics – an overview

Study of biological systems and their response to electrical and magnetic stimuli has been of interest for over a century now. Driving this interest is the essential fact that humans (or any other living species) are essentially driven by electro-chemical reactions which essentially regulate all the physiological movements. In addition, the components of human bodies, e.g., blood, cell membranes, proteins, ion-channels etc., all contain charges or dipoles embedded in their molecular structure that can be made to respond to external electrical excitation. However, for the better part of the last century, the main interest was focused around the chemical response of the body. Such studies were mostly group-wise experiment driven. With the advent of more sophisticated technology – especially in diagnostic domains the focus has now shifted to studying the response of small tissues and cells. In particular, the application of electric and magnetic fields, or even optical and/or ultrasound for probing and diagnostics has begun to rapidly emerge and grow. This has given rise to a whole new class of research that falls under the purview of “bio-electrics”.

Bio-Electric research, encompassing the exploration of electrical stimuli and their bio-responses (i.e. the physiological or chemical response of cells and/or tissues) has seen a tremendous growth in the last decade or so. A lot of research work has been published targeting areas such as alternative drug delivery methods at the cellular level<sup>1</sup> [1], single cell and tissue membrane dynamics [2, 3], directed energy systems and therapeutic applications etc. to name a few. Unfortunately, almost all the development in these and associated areas is limited to either a single cell or small and localized tissue models. For example, cells are easier to study *in vitro*, given their small size, homogeneity and ease of isolation and growth. Studies in full body responses, on the other hand, are rather limited and in their infancy at best. This limited information impacts development in this area. Furthermore, given the complicated inter-dependencies of cells and tissues of different types within a composite whole-body, it becomes relevant and germane to study “whole-body” aspects. Also, devices with full body impact such as TASERS developed without comprehensive studies, have led to extremely undesirable effects (e.g., deaths in some cases) that clearly need to be addressed and analyzed. Similarly, even

---

<sup>1</sup> The journal format followed for this dissertation is IEEE Transactions on Plasma Science.

though studies of nerve segments [4-6] and the conduction block of electrical action potentials (AP) in nerves have been probed for several decades [7-10], there is currently no viable solution for achieving AP blocks in a robust, controlled and consistent manner. Some of the methods that have been proposed involve AC interruption signals [7, 11], while other work has explored DC current injection [12-14]. Other methods that have been examined include temperature alterations [15, 16] and injection of chemicals. However, in all of these proposed methods, there is a high degree of variability; there are often deleterious side-effects such as tissue damage; the effects can be non-localized, slow, or not very robust. Consequently, a robust AP block method is the other aspect that the present dissertation will explore.

## **1.2 The role and advantages of bio-modeling**

Over the past decade, simulation capabilities have grown tremendously in ways of scope as well as the level of detail, in every aspect of life. The most important reason driving this surge in modeling and simulation schemes is that given sufficient level of detail, these systems are able to provide an acceptable level of accuracy in making realistic predictions, while being completely non-invasive. Whether it is modeling tissue necrosis during radiofrequency ablation [17], optimal biopsy pathways [18], or tumor progression paths [19], extremely sophisticated and powerful schemes exist that allow such models to deliver high precision estimates and results. The other advantage of any modeling based approach is that it significantly reduces the prototyping collateral, making it a cheaper and faster process. It also allows for the quick evaluation of a wide parameter range without having to experiment and physically evaluate a range of scenarios and possibilities. A study for validation data involving live subjects, even though vital for end validation, is expensive and requires various arrangements and protocols and some inherent delays. Simulations, on the other hand, are faster and provide fundamental understanding of the underlying basic processes and phenomena. Besides, both deterministic processes (such as propagation of information in nerve fibers) and non-deterministic systems such the use of heuristic machine learning to study vocal pitch tracks can be studied and estimated.

## **1.3 Overall scope and specific goals of this research work**

In order to be able to perform a systematic analysis or development, it is necessary that there exist a clear body of work that needs to be performed, since neither unlimited time nor

resources exist. Towards this end, this chapter provides the overall scope and a list of more specific targets and tasks that this research expects to meet and accomplish.

- Develop a full body mathematical model that will allow for computation of potential values in the 3-D discretized tissue volume.
- The underlying algorithms will then be validated using analytical computations for simple cases of geometry and complexity.
- The system will be further developed to incorporate tissue complexity and body contour variability.
- Provisions will be provided for simulating multiple electrodes.
- These electrodes can be defined as arbitrary shapes depending on user specification.
- The overall system will be applied stimulus independent, which could be potential or current waveforms.
- For the purposes of development, binary model files provided by Brooks Air Force Base, San Antonio, TX will be used.
- This system will employ distributed algorithm and distributed (parallel) computing. It will be scalable by the number of processors, and consequently, the problem size.
- The output form of this system will also allow for computation of current, current density in each of the three orientations.

Upon successful completion of the above goals, the resulting computed data for potential values within a tissue model would facilitate and allow for studies of possible activation of nerves and potential action potential block. The following tasks are therefore proposed for implementation.

- Existing nerve models for myelinated and unmyelinated nerve segments will be validated.
- Potential problems with the AP blockage schemes that exist, involving AC and DC current injection will be explored and analyzed.
- Electroporative effects of ultra-short, high intensity pulses to nerve membranes will be studied from existing literature [20-25].
- The resulting changes in membrane conductivity due to formation of nano-pores in membranes will then be incorporated into a modified model of nerve segments. This will be done to study whether action potentials can be interrupted by modulating the membrane conductivity in unmyelinated nerve segments.

- Upon systematic examination of the above, this will also be explored and expanded for application in myelinated nerve segments.
- The numerical models will eventually result in “strength-duration (SD)” curves relating the applied electric potential and the pulse duration required for successful AP block in nerve segment (myelinated and unmyelinated) of some selected diameters.
- Given the sparsity of modeling schemes that incorporate branching of the nerve segments, the above concepts will also be probed for their applicability to multi-branch segments, myelinated as well as unmyelinated.
- Finally, some recent experimental observations on ion-channel blockage (e.g., the Sodium channels) will be examined with the intension to put forth plausible explanations and scenarios. Here the emphasis will be more on qualitative features and the underlying physics rather than rigorous bio-computational analyses.

The above overview was meant to present an extremely abbreviated idea of an extremely detailed research area encompassing significant work that is to follow. It is hoped that by way of this research work, multiple levels of tissue resolutions could be studied upon being stressed by electric fields. At the conclusion phase of this dissertation work, a brief over view of the latest work that targets electric field effects on cell clusters will be presented. Even though single cell response has been studied extensively [24, 26-29], very few attempts have actually targeted cell clusters [30, 31]. Even fewer time dependent analyses exist, as will be presented in this dissertation research.

This dissertation is structured in the following manner. Chapter 2 is devoted to an in-depth background study of the current research area and related aspects. This is followed in chapter 3 by a detailed presentation of the numerical and algorithmic details of all the modeling schemes that this dissertation targets. Subsequently, all the results and analyses appear in chapter 4. This chapter also includes discussions of the results. The final chapter is used to summarize results from this dissertation. It also lists possible future work or extensions to the work already done in this research. Some miscellaneous algorithms and concepts (which have been identified as important) are collated in an appendix that follows the references.



## Chapter II

### Literature Review and Pertinent Background

*Proteins are the machinery of living tissue that builds the structures and carries out the chemical reactions necessary for life. - Michael Behe*

#### 2.1 Overview

The biochemist, Michael Behe, may or may not find universal acceptance for his beliefs owing to his advocacy of *Intelligent Design*. However, the above statement does highlight a key truth – that every mammal body is driven (at the fundamental level) by chemical reactions. Over the last two centuries, human interest in the inherent biological functioning of the body has led to several discoveries. The founding facts, all point towards a chemical basis, or, more accurately, an electro-chemical basis for biological action. Mammalian anatomy, in general, is comprised of organic tissue down to the cellular level. Consequently, every behavior exhibited when examined at the cellular level, shows the distinct signature of its chemical nature and inherent ionic movement.

For example, one can consider the simple act of breathing. It involves systematic stimuli from the brain stem whether voluntary or involuntary. At a very coarse level this can be viewed as the contraction of the diaphragm caused by the systematic stimuli, followed by its elastic recoil. However, at the micro level, this is a reasonably complex process driven by chemo-receptors. These are a special type of cells that perform transduction of a chemical signal into an action potential (AP). The AP is a voltage driven electrical signal and the bio-response form along neural pathways. These chemo-receptors detect levels of CO<sub>2</sub> in the blood-stream by monitoring the H<sup>+</sup> (hydrogen ion) concentration. A higher concentration leads to a drop in the pH. In response, the inspiratory centre in the medulla sends nervous impulses down the phrenic nerve to activate the intercostal muscles. This, in turn, regulates the breathing rate as well as the volume of the lungs. Thus, an electrically-driven, continuous feedback processes based on distributed sensors is at work within the mammalian body.

The above example is meant to highlight the chemical interactions at the most fundamental level of the mammalian anatomy. It also shows the intricate and fundamental role of electrical signaling. The implication is that all mammalian tissue is extremely susceptible to any electric/electromagnetic stimulus. This is very important since it means that through external

application, electrical stimuli, could possibly be made to have an effect on the nervous system and the electrical signaling within mammalian bodies. A modeling study to examine and make predictions of the biological behavior or tissue response could be geared towards the functioning and neural activation and effects of external electrical stimuli. Previous studies have explored the intrinsic anatomical stimulation based on natural nervous signaling. However, the gap that exists in the bio-electric/bio-medical community is in the area of physiological response to artificial (external) stimuli (such as direct contact electrical impulse) or electromagnetic radiation.

Studies of such electrically induced bio-responses are driven by several considerations. First, external electrical stimulation could be a useful therapeutic tool to re-activate nerves and spinal tissue in injuries to the nervous system. Second, concrete thresholds relating to safety levels and potentially hazardous limits of electrical stimulation need to be ascertained. This is particularly important in the context of pace-makers and electrically driven medical instruments and sensors. The safety aspect is also important in specific modern-day environments such as high-power transmitters, microwave stations, and military radars. Currently, there exist schemes that allow for the study of “small tissue volume” response to external excitation such as ablation. However, prediction of possible outcomes such as fibrillation in response to a directed energy source (such as the TASER® gun or high-power microwaves) requires the inclusion and careful analysis of a full body response. In particular, the various nervous pathways that could get activated need to be examined. This is a complex task and involves the electrical details, bio-electric interactions, whole body bio-responses associated with the complex bio-components and their inter-dependent interactions. However, here we attempt to study a small aspect of this overall issue through appropriate simulations as a pioneering step. Therefore, one of the key objectives of this research is to address the void in modeling schemes that would help predict and quantify the full body response of mammals to external, direct-contact electrical stimuli. Apart from the numerical model development, this dissertation research also attempts to explore electrically driven means of controlling the neural pathways through the use of ultra-short voltage pulses. The analysis is based on time-dependent, spatially distributed neural bio-models.

## **2.2 Full body modeling scheme**

Electrical excitation, which has been used to stimulate both the central and the peripheral nervous system, has a variety of potential diagnostic and therapeutic applications

[32-34]. For example, electrically stimulated neurogenesis is a potential tool for enabling the production of new nerve cells from neuronal stem cells [35, 36]. It is used in implantable devices for neuromuscular stimulation; these devices are designed to control the contraction of paralyzed skeletal muscles, thereby producing functional movements in patients with stroke and spinal cord injuries [5, 37]. Electrical excitation is also a useful tool for studying the properties and functions of nerves (including the brain) and muscles (including the heart). It also provides information on strength–duration characteristics including the inherent time constants. Strength-duration curves yield the critical electric pulse duration thresholds for a given electrical signal intensity. These are important for determining the safety levels for electrical excitation for a given voltage pulse or, conversely, the electrical intensity that can be applied for a chosen pulse duration.

Excitation with ultra-short pulses is also an important issue for the health and safety assessment of ultra-wideband (UWB) sources that produce nanosecond pulses. This issue has been discussed at length elsewhere [3]. In general, muscle excitation can be achieved either remotely through the principle of electromagnetic induction [38-40] or directly through electrical contact [41]. UWB pulses have not, to date, shown significant, robust, and reliable biological effects. Such UWB studies using rats examined behavioral teratology, heart rate, blood pressure, brain histology, and genetic alterations [42-45]. This contribution focuses on pulsed excitation delivered to biological tissues (and whole bodies) through direct electrical contacts. Thus, it is assumed that electrodes can be directly applied on the muscle/tissue surface. Motor nerve fibers within the muscle are then excited by the potential created within the muscle by the external source. In general, the potential can also be applied through a conductive medium surrounding the biomass as discussed in a previous report [46]. The use of ultra-short electrical pulses in this context is an emerging topic of interest [27]. Such pulses of nanosecond duration have been shown to penetrate the outer (plasma) membrane to create large trans-membrane potentials across sub-cellular organelles [47]. Thus, for example, neurotransmitter triggering or calcium release (from the Endoplasmic Reticulum) is possible through the use of ultra-short pulses [1, 26, 48]. These ultra-short pulses have also been shown to porate the outer plasma membrane reversibly, and this can be an important technique of artificially tailoring a pathway into the cell for drug delivery. Use of this new technology to study sub-microsecond pulse widths might reveal new biological phenomena as well. To highlight the plasma membrane poration and its reversibility, upon the application of nano-second Pulsed Electric Field (nPEF), consider figure 2.1. It shows the PI uptake in a cell suspension containing both PMN (poly-morpho-nuclear leuckcyte) cells (yellow circles) and Jurkat cells (blue circles) after

a 300- ns, 60-kV/cm pulse was applied [21]. The left column shows the cell suspension under incandescent illumination and the right column under fluorescent illumination. For the single-pulse application, only the Jurkat cells took up PI. With an increasing number of 300-ns pulses applied, the differences in PI uptake by PMN and Jurkat cells became less pronounced. For a pulse duration of 60 ns, PMN cells were found to be unaffected by the pulses, despite multiple pulses, whereas the number of Jurkat cells which showed PI uptake rose to almost 100% after ten shots. This experimental data reveals two important aspects: (i) It is indeed possible to porate the outer membrane of cells. This is an important “proof-of-concept” demonstration. It thus becomes plausible that the use of such short duration, high-intensity pulses would also be instrumental in facilitating the poration of nerve membranes. (ii) The poration effect can be enhanced by multiple pulsing, and there is some variability within different cell types.

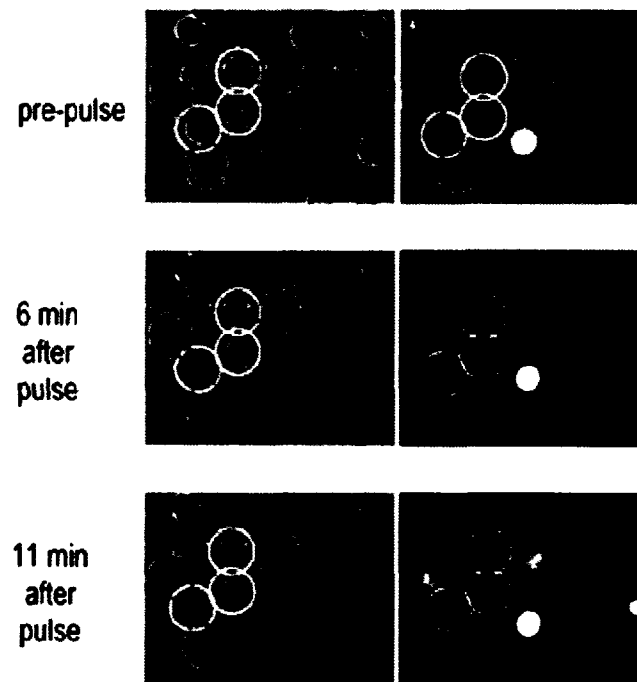


**Fig. 2.1.** Illustration showing the entry of PI into the PNM and Jurkat Cells before and after application of a nPEF [1] This experimental result demonstrates the possibility of outer membrane poration by an ultra-short, electrical pulse.

Thus, in summary, membrane integrity aspects are visible in figure 2.1, and can be considered to be the main effect of electric pulses of this time scale. The process of electroporation causes enough channels to form for the dye to enter the cell membrane. However, because the external electric field rapidly decays, these pores reseal and prevent the dye from escaping. Not only does this ensure that structural integrity is maintained, but also

that this is a *repeatable process*. Therefore, the chemical (and consequently the electric) property of the intracellular regions can momentarily be altered and then recovered fairly rapidly (considering the time scale of operation) using the application of these nanosecond pulsed electric fields. The importance of this will become apparent when we discuss the possibility of using electroporation for neural traffic interruption.

The other key area in which the lack of full body electrical modeling is acutely felt is in non-lethal weapons development. Over the last few years, there have been several news reports of fatalities involving TASERS [49]. The underlying reasons range from cardiac fibrillation or destruction of neural pathways from the electrical energy. A robust scheme to study the impact of such directed energy devices at different areas of the body that may be dependent on other bio-factors will certainly help to improve designs of such devices.

#### 2.2.1 Intrinsic hurdles in full body modeling.

One of the primary reasons that full body modeling schemes are not so common is tissue complexity. So far, the most that has been done involves small tissue volume modeling for thermal ablation [17] or lesion growth modeling [50]. The above is perhaps better understood by considering a region near the human skin as shown in figure 2.2. A cross-sectional view (not drawn to complete scale) of the human skin and the underlying layers is given. Even though this is just a small tissue sample, the level of tissue variability is clearly evident. Clearly characterizing and accurately representing whole bodies with multiple tissues is very complex and daunting. In order to perform a simulation of the electrical bio-response to an external stimulus, the characteristics of all the tissue types should be incorporated. This is an extremely non-trivial task due in part to the following (but not limited to) reasons:

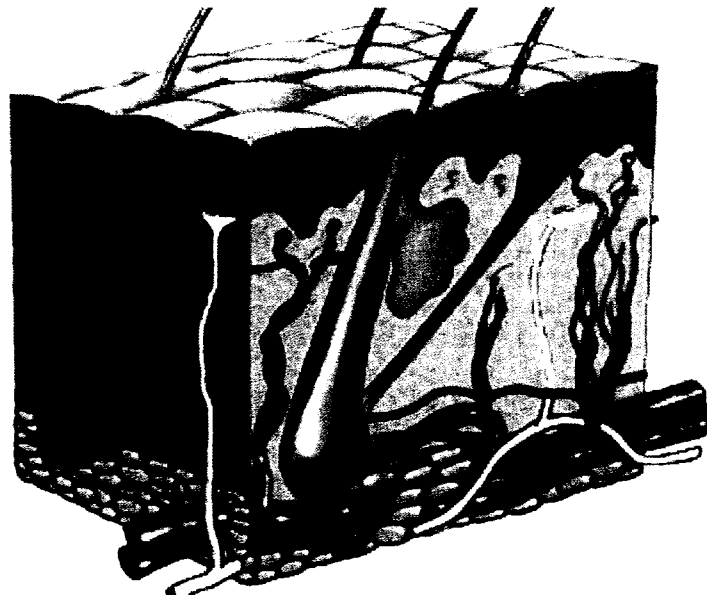


Fig. 2.2. Cross-sectional representation of human skin tissue.

- 1) Simulation accuracy depends upon the resolution of the model.
- 2) Tissue characteristic parameters need to be known *a priori* for each and every type of tissue present in the volume. This involves large-scale “data-mining” and the meticulous characterization of the various tissues within a body due to the large variety and heterogeneous distribution of the different tissues. One needs to have sufficient spatial resolution by extracting tissues from all locations in addition to determining their electrical characteristics such as permittivity and conductivity. An added challenge is that the electrical parameters change with the health of the tissue. Hence, measurements need to be done quickly before “tissue death” or other irreversible effects set in.
- 3) Irregular geometry is inherent in any whole body bio-structure. This makes it difficult to accurately model and represent the actual structures and to specify boundary conditions at the surfaces. Usually Cartesian co-ordinates are used that inevitably lead to spatial discretization errors. However, discretization errors are not exclusive to Cartesian discretization and may appear in spherical/cylindrical schemes too.
- 4) The excitation and the subsequent response is dependent upon:
  - a) The placement of the electrodes,
  - b) The shape of the electrodes,
  - c) The form and duration of the stimulus.

We examine the above issues in the next few sub-sections. Unless otherwise noted, we will refer to figure 2.2 in the next three sub-sections.

### 2.2.1.1 Model resolution

Consider that the tissue block given in figure 2.2 spans 10 cm by 5 cm by 1 cm. Since any digitization of this tissue volume will involve some form of scanning operation, let us assume that the tissue section is discretized at 1 cm. This means that the tissue volume is scanned in 1cm sections in each dimension (direction). The resulting section will then consist of  $(10*5*1)$  cm<sup>3</sup> blocks. These elemental volumes are called nodes and make up the building block of the underlying modeling scheme. Using such a low (coarse) resolution leads to 50 nodes but at the cost of loss of tissue *complexity detail*. What that means is that given that most of the embedded regions that are significantly smaller than 1 cm, such as vesicles and follicles will be lost in such a discretization scheme. However, if the scanning is done at say – 1 mm resolution, the total number of nodes rises to  $100*50*10=50000$ . This leads to a dramatic rise in computational price but yields the advantage of extremely fine-grained results. To highlight this, typical myelinated nerves have a 2 mm inter-nodal span.

### 2.2.1.2 Tissue parameters

As mentioned previously, bio-models are, without exception, obtained using some form of volumetric scanning method. However, these methods (MRI, CAT, etc.) are imaging methods. That means the tissue density or its response to a particular excitation method is used to “draw” its shape. It is relatively easy, though incomplete, to generate the volumetric image data of a particular data type; however, in order to be able to use such information in mathematical models, it is imperative that their characteristics and parameter values also be known. For example, in the electrical domain, the specific conductivity and permittivity is needed for mathematical modeling and quantification. Fortunately, over the years, almost all the normal tissue types present in common animals and humans have been mapped and characterized. Nevertheless, this does not preclude the possibility that a particular tissue volume might consist of an abnormal growth that displays characteristics different from those in the surrounding regions. This can also be understood by considering the case where a bone has been replaced, grafted, or in extreme cases, replaced with an artificial limb. In any event, in order to successfully model and compute the response of a bio-model, all the underlying tissue models need to be identified and characterized using known, quantifiable parameters.

### 2.2.1.3 Excitation (stimulus) locations and form.

As mentioned in section 2.1, since short term UWB radiation has to date, not shown significant biological effects, this research focuses on pulsed electrical stimulus delivered through direct contact pathways (electrodes). Referring again to figure 2.2, assume that a

rectangular electrode spanning the entire top surface is used as the “Anode”. Given such a setup, barring a few minor areas at the follicle and other similar irregular regions, the electric field lines would *mostly* be linear and vertical. If the orientation of the electrode plates were to be changed, the average electric field would be different from the previous case. Furthermore, if the cathode was reduced to a small circular region, with the anode being kept the same, the electric field would not only be different, but would also no longer be uniform. These different examples all indicate the fact that electrode regions’ size, shape and placement play a vital role in setting up the electrical driving forces that ultimately affect the behavioral response of the tissue upon stimulation. This is worth mentioning because this *response* can range from activation of nerves (if any, as embedded in a particular region), to cell death (tissue necrosis and apoptosis).

On the topic of applied stimulus, it should be mentioned that even the duration of the applied potential pulse is a variable that needs to be accounted for and studied. For example, let us assume that the entire tissue volume represented in figure 2.2 is comprised of only the dermis. If the applied stimulus is a DC pulse with a finite ON time, then this ON time **MUST** be such that the dermis sub-volumes are sufficiently charged. Otherwise, the observed current flow and potentials would be lower than the maximum that could be achieved owing to the finite electrical charging time of the system. In the next chapter, a brief table highlighting the effective conductivity and permittivity of some of these tissues is listed. These can be used to compute the effective time constants and the charging durations for various tissues in the context of electrical pulsing.

The above essentially highlights the hurdles that make it virtually impossible to perform accurate simulation studies. Consequently, research groups have tended to focus on tissue sub-sections and localized effects within such regions. Localized tissue uniformity (e.g. liver block or skin section) definitely helps. Micro level non-uniformity in cases such as capillaries, is typically ignored without loss of any appreciable accuracy. However, to develop a more physical and accurate bio-model and to address this void in the area of bio-medical modeling, this dissertation aims to create a robust and scalable simulation scheme that will allow for whole body modeling.

As mentioned earlier, to obtain any practical, usable information the discretization resolution of the tissue model needs to be sufficiently high. However, this leads to a dramatic increase in the computation cost. Stand alone computational systems cannot fulfill the resource requirement for such a large order system. Additionally, the commercial restrictions that are



often imposed on commercial simulation packages such as those used in [17], can be prohibitive. In this context, parallel algorithms have the potential to alleviate most of these computational restrictions by providing resources that span more than one physical system. These resources include memory capacity and processing capability. However, distributed (parallel) algorithms are essentially more complex than their serial counterparts because apart from numerical model component, they also need to incorporate data and synchronization communication schemes. Furthermore, to be really efficient in handling large-scale problems based on a *given resource/processor* limit, even the data storage scheme needs to be altered. A more detailed example of this is given in chapter three, where the entire process flow diagram of the proposed distributed modeling scheme is presented. To preface that however, consider the following hypothetical scenario where two data sets A, B are operated upon. This operation could be anything from simple data match to solution of a system of equations. In a serial system the entire operation could be summarized using the following steps.

1. Load the datasets.
2. For each element in dataset A:
  - a. Perform operation with element in dataset B.
  - b. Echo the result.
3. Exit.

Comparing this to a parallel scheme of operation, and using the shared data scheme, the algorithm would end up with a possible form such as:

1. Identify a control processor.
2. *Send appropriate sized datasets to each slave processor.*
3. *Wait for results from each slave.*
  - a. At each slave node for each element in sub-dataset A:
    - i. Perform operation with sub-dataset of Element B
    - ii. *Send result to Control processor.*
4. *Reorder each result as received from the slaves.*
5. Echo result of each operation.

This is an *extremely simplified* and generic example, yet one can clearly identify the communication and synchronization overhead that would be involved with a distributed solution scheme. The extra steps have been *italicized*. However, the underlying advantage that

is perhaps not very apparent is that significantly large datasets can be operated upon with a distributed solution scheme.

As will be highlighted in chapter three, the full body modeling scheme being proposed in this research involves solution of a system of equations that has a form given by the following equation:

$$[\mathbf{M}]x = b \quad (2.1)$$

where,  $[\mathbf{M}]$  is a coefficient matrix and  $b$  is the target vector. As will also be shown later,  $[\mathbf{M}]$  is an extremely sparse and asymmetric matrix. The normal solution methods of solving equation (2.1) involve some sort of factorization of  $[\mathbf{M}]$ . Its asymmetric structure, eliminates the possibility of employing Cholesky factorization [51, 52] that can take advantage of symmetry. It can not only speed up the operations but also provide memory savings. The practical solution, then, is to perform a LU decomposition in sparse form followed by a forward-backward substitution to obtain the vector  $x$ . Several computational schemes that deal with such LU factorization methods have been developed [51, 53-58] and consequently, the underlying math or the schematics will not be discussed here.

The primal application area of a full body modeling scheme is to predict or simulate the possible response of the underlying organs or tissue regions upon application of a stimulus. Apart from possible thermal response (which is not being modeled here), the physical response is almost *always* due to activation of some embedded nervous segment. To study these possibilities – viz. activation method and its control, the second half of this research addresses neural modeling (activation, traffic and interruption). More pertinent background and precursory information relating to these issues is presented in the remainder of this chapter.

### 2.3 Neural Signals and block schemes

Given the overall goal of being able to understand, quantify, and predict possible adverse electrophysiological changes, including electrically induced organ failures in humans and whole animals due to electro stimulation, the overall objective requires a two-step approach. As first discussed by McNeal [59], the first component is the development of a numerical model for quantifying the microscopic currents and electrically induced potentials due to an external voltage pulse in whole-body systems. Such capability can also provide a useful tool for optimal electrode design and placement. The second step is to use the derived excitation potentials within the whole-body system to determine the biological response of nerves, muscles, and related electrochemical reactions. One of the key areas where a lot of

research and study has been done is that of nerve segments and the action potential propagation and block mechanism. However, before we investigate any of this, it is prudent and logical to examine the basic structure of a nerve segment and this is given in the next sub-section.

### 2.3.1 Nerve segment structure and key terms

As is well known in the field of physiology, the basic information/signal pathway in any mammal is comprised of a complex network made up of neurons. Neurons are electrically excitable cells that process and transmit information and in vertebrate animals, they are the core components of the brain, spinal cord and peripheral nerves. A schematic figure of a neuron is shown in figure 2.3 [60].

It should be noted that figure 2.3 represents a myelinated neuron in contrast to an unmyelinated one which is shown in figure 2.4. The differentiating element is the myelin sheath that is shown covering the axon. Also to be noted is the segmented form of this myelin sheath. The region between each such myelin covered axon (myelinated axon) segment is known as the “Node of Ranvier.” For the most part, the primary conduction pathways are comprised of myelinated neurons. This is due to the fact that myelinated neurons provide a faster conduction velocity of information due to salutatory effect induced by the extremely high resistance myelin sheath between consecutive nodes [6, 59, 61]. It should also be noted that any “information” or a signal that is propagated via the neural channels is in the form of a temporally varying potential wave known as the Action Potential (AP). For the sake of thoroughness, prior to any discussion of significance and methods of AP arrest, a brief discussion of the underlying mechanism involving the rise and propagation of AP is presented and discussed.

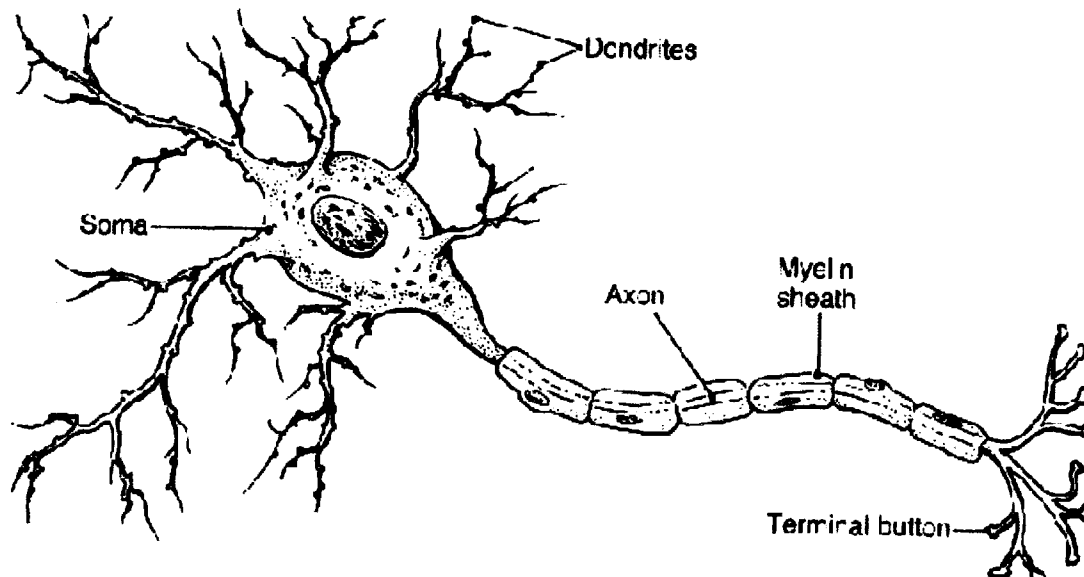


Fig. 2.3 A typical mammalian neuron (myelinated).

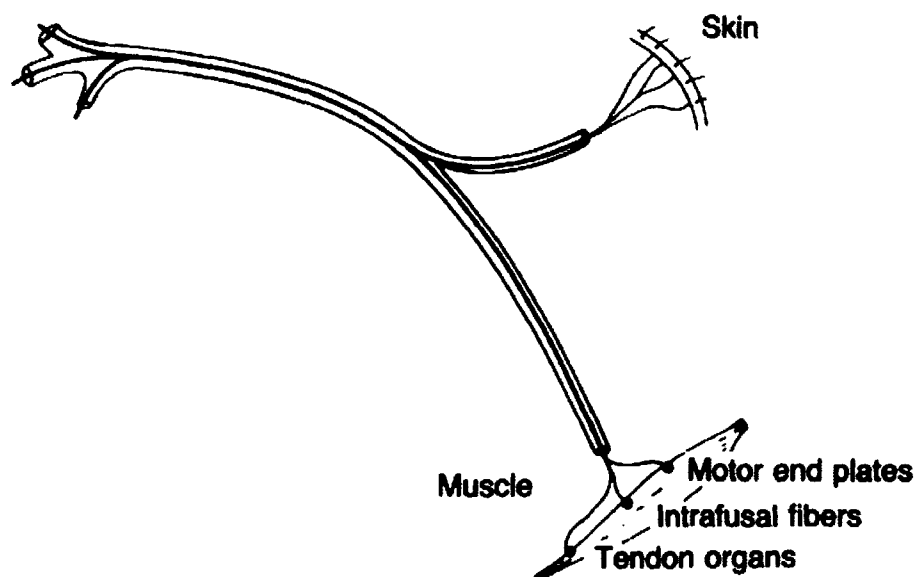


Fig. 2.4 A typical mammalian neuron (unmyelinated).

### 2.3.1 Action Potential

It is now well known that generation and propagation of an action potential in a nerve fiber is triggered by perturbations in trans-membrane potential that activate ionic flows through voltage-gated sodium and potassium channels. These channels are essentially protein structures that reside on the nerve membrane in a distributed manner. Dynamical details and mathematical

analyses of the various ionic currents across the cell membrane can be obtained from the Hodgkin-Huxley [62, 63] and Huxley-Frankenhaeuser [6] models for unmyelinated and myelinated nerves, respectively. The governing equations (and the underlying modification to be proposed) will be presented in the next chapter. The qualitative features of action potential generation and propagation though, can be distilled into the following salient aspects.

- The attainment of a trans-membrane voltage shift that exceeds a threshold level is a primary requirement for the successful generation and launch of an action potential.
- Three factors facilitate and contribute to the attainment of this critical trans-membrane potential shift.
  1. First, the voltage-modulated sodium and potassium channel conductivities need to possess and maintain distinct and disparate temporal evolution rates. The sodium channel is turned-on faster than the potassium channel, causing sodium inflows at earlier times. For example, a slight initial depolarization leads to sodium inflows that work to accentuate the depolarization as positive charges begin to be continually inducted into the nerves.
  2. The capacitance afforded by the membrane lipid bilayer facilitates charging and voltage development across the membrane. Thus, the sodium inflow at the earlier times enhances this potential build-up. The voltage increase modulates channel conductivities and this in turn further enhances the rate of ionic transport. The net effect is a positive feedback mechanism that amplifies the initial trans-membrane potential perturbation to create a local voltage that exceeds the critical threshold.
  3. Localized enhancements of the trans-membrane potential drives ionic conduction into neighboring nerve segments, as predicted by the usual “cable-model” of transmission line theory[10, 59, 64-66]. This effectively injects charge into the neighboring elements and launches a propagation of the electrical wave from the initial source point.
- The slow but eventual voltage-modulated “turn-on” of the potassium channel, coupled with the sodium channel inactivation, work to quench the potential and restore equilibrium at the initiating node. The sodium-potassium pumps help restore charge distributions to their original levels.

It should be noted that the neuron model proposed in [62] which has been adopted as the *de-facto* standard in almost all subsequent studies in this area, was based on a giant squid axon. In more recent studies [67, 68], it has been shown that the neurons in humans and other mammals tend to have a significantly higher number of ionic channels that contributed to the activation of the nodes. Some recent researchers [69, 70], have employed a slightly different model wherein it has been assumed, in contrast to the classic model, that the sodium channel does not have any inactivation variable. They also incorporate the dynamics of an additional calcium channel current in the membrane activation/deactivation process along with a calcium assisted potassium hyper-polarizing current.

It should also be mentioned that the original Hodgkin-Huxley (HH) model was for an unmyelinated axon. One of the first studies for the myelinated case involved incorporation of the molar concentration of sodium and potassium ions in the medium surrounding the axon. However, in quite a few other reports such as [61, 71], the original HH equations defining the nodes were retained. Changes were incorporated by treating the “Node-of-Ranvier” as having significantly higher densities of sodium, potassium and leakage channels. The inter-nodal distance (myelinated part) is usually modeled as extremely high resistance, coupled with an extremely low capacitance value. This gives rise to an extremely low time constant for the myelinated segment of the axon and consequently allows for the modeling of the salutatory conduction and leads to a fast response. This form of treatment of the myelinated segments allows for a unified scheme of modeling the complete neural spectrum while keeping the equations consistent. It is the apparent lack of incorporating the myelinated segment in studies such as [69, 70], that seems to contradict those of other researchers in this area [72-74]. The possibility of interrupting AP propagation, as already mentioned in section 2.2, is the primary motive behind this dissertation. Hence, concepts and issues relating to AP signal blockage are examined next.

### 2.3.2 Action Potential conduction block

Since a shift in electrical potential is a necessary requirement to initiate and maintain electrical propagation through a nerve fiber, *any event that disrupts the trans-membrane voltage can potentially impede action potential propagation*. One possibility is through the application of an external DC bias near a nerve. For a propagating action potential (initiated, for example, by a depolarizing voltage), the application of a positive bias on the outer region of the nerve would prevent the local potential from reaching the requisite negative value. This would effectively arrest AP propagation, and hence, in theory block nerve conduction. However, a number of

potential and practical problems arise from the application of an external DC bias for purposes of a conduction block.

- (i) First, the prolonged application of the DC bias can itself inject localized currents and charge the axonal membranes, thereby launching its own AP. The duration and amplitude of the external DC has to be sufficiently low to circumvent such “self-launch” phenomena.
- (ii) In addition, since the timing and sequence of propagating action potentials are not known *a priori*, it is practically very difficult to achieve reliable conduction blockages for all possible propagating APs.
- (iii) Any sharp rise times for the DC biasing voltages can lead to large capacitive charging currents that have a similar undesirable effect of self-launching an AP. Hence, the rise and fall times of any applied DC bias need to be sufficiently large.
- (iv) Long durations or repetitive DC biasing can potentially cause tissue damage due to internal heating [75]. For effective suppression of this deleterious effect, the net energy needs to be sufficiently small.

All the above problems notwithstanding, a good deal of research involving application of AC/DC interrupting signals to achieve AP block [8, 12, 13, 76-78], has been carried out. Though other methods of achieving nerve conduction blockage such as pressure application [79], temperature lowering [15], chemical and pharmacological means[77] exist, none can be as quick-acting, localized and yet reversible as electrical stimulation. Cessation of biological electrical signaling pathways can have a variety of applications in neurophysiology, clinical research, neuromuscular stimulation therapies, and even non-lethal bio-weapons development. For example, pudendal nerve conduction block during micturition can reduce urethral pressure [16, 80], or help relieve chronic pain from a site of peripheral nerve injury [81]. It is well known that the nerve blocking ability of electrical stimulation is progressive from larger to smaller fibers [82, 83] and has been used to activate muscles in a physiological recruitment order and to reduce muscle fatigue. The concept of arresting action potential (AP) propagation on command through external electrical stimulation could open the possibility of temporary incapacitation with applications to crowd-control.

The application of high frequency blocking signals alleviates some of the problems with DC biasing. The heat generation can be reduced and the biphasic signals make it somewhat more difficult to self-launch action potentials. However, the overall difficulties are not

eliminated, and the fundamental issues remain. In addition, the frequency of operation begins to play an important role in the blocking effectiveness. A frequency bandwidth limitation for AP extinction exists, and excitation that is either too fast or too slow cannot provide a conduction block [7]. Despite the reservation of all *our* results and discussion for another chapter, for the sake of a thorough discussion, the simulation results from our AC block modeling scheme, which was attempted on an axon with a diameter of  $24\mu\text{m}$  is presented now. Table 2.1 highlights the frequency range in which the AP was successful. The data is from a simulation done by us using the standard HH model for un-myelinated nerves. Details of the model and discussion of the results given here will be presented in chapters three and four, respectively.

As seen in Table 2.1, there is a frequency band for the interrupt signal to achieve successful conduction block.

**Table 2.1** AC block frequency range for good and fail AP block in an unmyelinated nerve segment.

Start time	Stop time	Frequency (kHz)	Diameter ( $\mu\text{m}$ )
0	7.9	7	24
0	7.9	7.3	24
0	7.9	7.5	24
0	7.9	8	24
0	7.9	9	24
0	7.9	9.2	24

It should also be pointed out that there is no robust method of determining this frequency range. However, an estimate can be made by employing the propagation velocity values for a given axon diameter. The small frequency range is easily understood from the standpoint of having to cause sufficient disruption of the trans-membrane potential during the time an incident AP approaches the “blocking spot.” A very low frequency bias signal will not have sufficient time to disrupt an approaching action potential, while a very fast oscillatory signal will effectively present a net zero average perturbation. Furthermore, the continuous AC signal contributes to localized heating. For these reasons, the use of AC biasing techniques for AP suppression, is not really an optimal solution. Though various different waveforms and electrode arrangements have been proposed [84] for blocking the action potential traffic, the underlying problems remain.

Almost all modeling and experimental work relating to AP conduction blocking (whether DC or high-frequency) has been performed at relatively low voltage amplitudes with



temporal durations in the micro-second range or higher. However, the development and use of electric pulses with very high fields ( $\sim 100\text{kV/cm}$  or higher) and pulse durations in the nanosecond range [24, 85] has been a very recent development in bio-electrics. From a practical standpoint, such high-intensity, short-duration electrical pulses (HISDEPs) or nPEFs have been shown to be useful for various biological applications including cellular electroporation [1], electrically-triggered intra-cellular calcium release [25, 26], the non-thermal destruction of micro-organisms [1, 86, 87], killing of tumor cells [1, 88], DNA damage [89], and possibly wound healing [90, 91]. The hallmark of such a HISDEP is the creation of a high density of nanometer-sized pores on the cellular membrane, followed by their relatively rapid recovery through re-sealing. This has been confirmed by analytical calculations [85, 92-94] as well as molecular dynamic simulations [95-97] and verified by tracking fluorescent dyes in flow cytometry experiments [1]. Since the process of electroporation in cell membrane has potentially far reaching possibilities (not to mention application in the AP block schema being proposed), it warrants a slightly detailed examination. Some of the pertinent and salient aspects of electroporation are briefly discussed in the next section.

#### 2.3.2.1 Electroporation

It is fairly well known that cell membranes are composed of lipids and proteins. Differences between cell membranes arise from the relative composition of these two constitutive elements and their structural arrangement. For example, proteins make up only 18% of the myelin membrane of nerve cells, while the rest of it is lipids. On the other hand, the inner mitochondrial membrane is 76% proteins [98]. A schematic representation of the cell membrane is shown in figure 2.5. Note that the cell membrane represented in figure 2.5 shows a significantly higher presence of lipids compared to proteins and may be considered to be representative of the myelin sheath. The other aspect is the variability in the lipid composition itself. A large fraction of mammalian plasma membrane is constituted of cholesterol and carbohydrates, etc. In any event, the above simply implies that a membrane has a very complex structure.

The central idea of “electroporation” is that it is a progressive and systematic re-organization without any molecular breakup or detachment [99] brought about by an electric field. Thus, the application of external electric fields to cells or tissues permeabilizes the cell membrane producing aqueous pathways (called filled pores) in the bilayer system. This process is referred to as electroporeabilization or membrane breakdown.

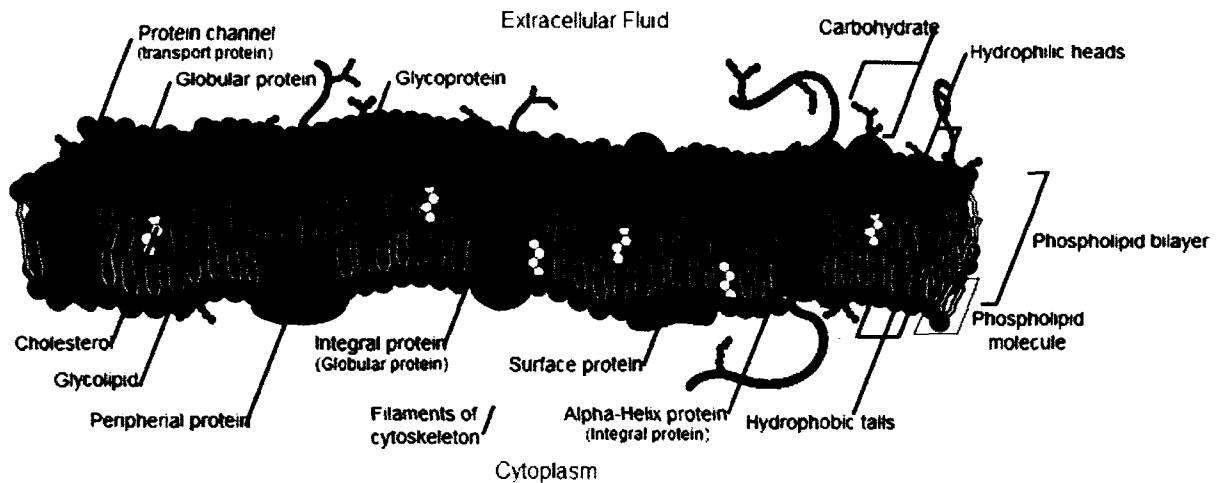
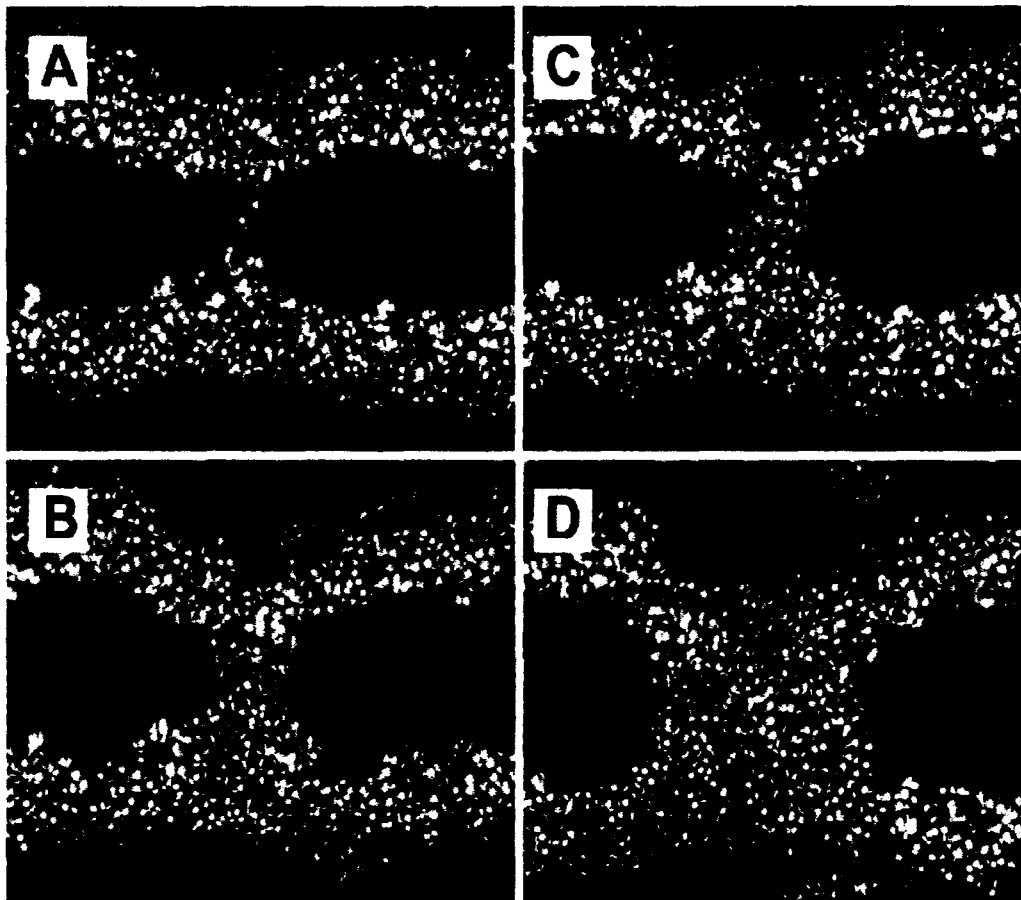


Fig. 2.5. Representation of a cell membrane section.

The molecular processes involved in this process are still not properly understood. However, a recent study [100] highlighted that it is a two step process. The first step is the organization of water molecules in a “wire structure” which penetrates the water-repellant (hydrophobic) lipid bi-layer. This initiates a deterioration of the structural integrity of the bi-layer eventually leading to the formation of the pore. Typical pore diameters are on the order of 1.6 nm with about a 0.6 nm statistical spread. Time scales for pore re-sealing range from milliseconds to a few seconds with the dynamical details depending parameters such as cell diameter, applied electric field magnitude, permittivities, and membrane tension. This process can be visualized using computer simulation and a sample of the same is presented in figure 2.6 which has been adopted from one such work pertaining to molecular dynamics simulation [101].

### 2.3.3 Proposed Action Potential conduction block scheme

In this research, we discuss and analyze the possibility of applying HISDEPs for blocking nerve conduction by modulating the membrane conductivity through the electro poration process. So far, such a study has not been performed, though simple considerations of electroporation in the context of ventricular muscle breakdown were reported [102]. Formation of a high pore density would increase the local membrane conductivity and effectively “short-out” the trans-membrane potential of a nerve in the vicinity of the pulsing electrode.



**Fig. 2.6:** Snapshots of pore formation in the DOPC bilayer, with an applied field of 0.5 V/nm in the presence of 1 M NaCl (right): A) 5330 ps, B) 5450 ps, C) 5500 ps, D) 5700 ps. The lipid head groups are shown in yellow, the chains in cyan, chloride ions space-filling in green, sodium ions in cyan; water is shown as dark blue and white space-filling in the interface region and the pore, as dark blue bonds elsewhere. The potential is positive at the top of each snapshot relative to the bottom. [101]

The net effect would be a disruption of the requisite trans-membrane potential shift required to sustain AP propagation. The use of a HISDEP in conduction block context would conceivably offer the following advantages:

- Negligible heating due to the low energy content of each pulse. This would minimize any possible tissue damage, and allow repetitive pulsing (even multiple firings with tailored amplitudes) to achieve the desired effects for selected durations.
- The effects of such HISDEPs would be reversible due to the resealing of pores created electrically by the external voltage. Hence, a permanent effect would be avoided.
- The turn-on would be relatively fast (on the order of tens of nanoseconds [92]), and the effect could be spatially tailored.
- Unlike the DC or AC excitation, it would be more difficult to “self-launch” action potential waves that required depolarization over micro-second time scales or longer.

The porated regions of the membrane would effectively clamp the local trans-membrane potential to near-zero values. Also, the nanosecond pulse termination would produce a negative voltage change with time, and hence, a strong negative displacement current. This would cause the membrane potentials to fall sharply back to their resting potentials well before the microsecond time scales that are typically required for launching action potentials.

#### 2.3.4 Synaptic process and possible AP block site

Since the process of neural signaling involves not only the conduction (salutatory or otherwise) within a neuron, but also the “jump” across the neuron through the synaptic space (gap). This implies that a possible conduction block site may either be the pre-synaptic or the post-synaptic axon terminal. To better illustrate this process, consider figure 2.7.

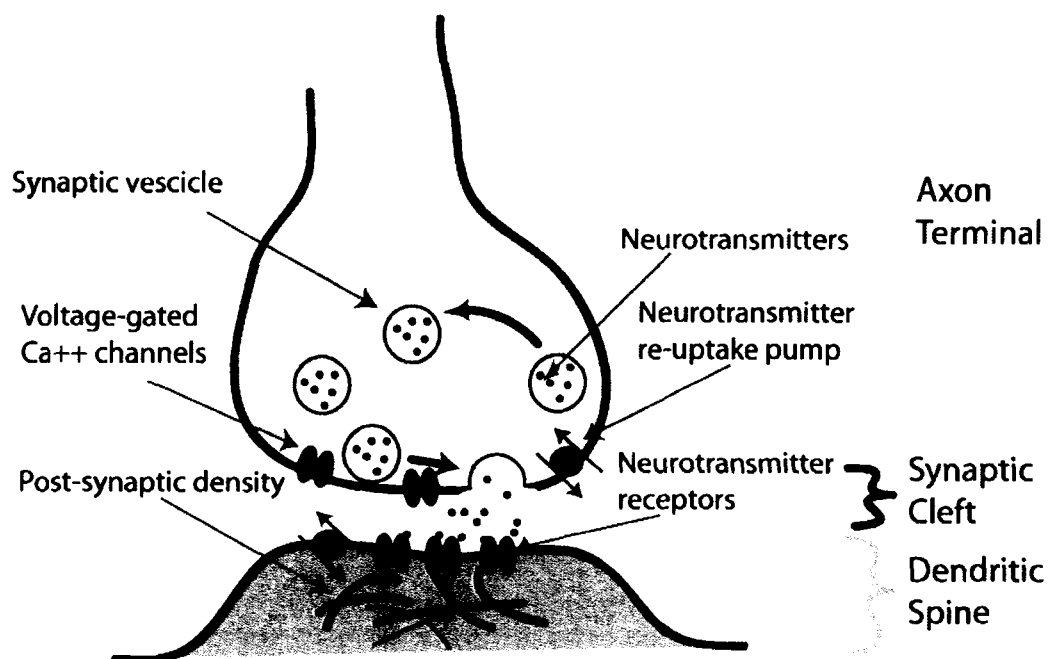


Fig. 2.7: Major elements in prototypical synaptic process.

When an action potential travels to the end of the pre-synaptic axon terminal, the rapid depolarization causes Calcium ionic channels near the end points to open. Calcium stimulates the transport of neurotransmitters (packaged in small vesicles) to the synaptic membrane, where these vesicles fuse with the membrane, and eventually release the neurotransmitters into the synaptic gap. These vesicles then travel and bind to the receptors at the post-synaptic neuron. It

should be noted that this conduction is ALWAYS uni-directional at any given time. Also, this movement of the neurotransmitters is by diffusion across the narrow synaptic gap – with dimensions typically on the order of ~20 nm. Since this entire process is initiated by the influx of  $\text{Ca}^+$  ions through the voltage gated  $\text{Na}^+$  channels and because pulsed electric fields can modulate calcium release [25, 26], it may be hypothesized that electric field effects on the  $\text{Ca}$ -release may play a role in AP blockage. Modulation and changes in  $\text{Ca}^+$  drift across the neuronal terminals could influence the continued AP propagation through neurons.

The mathematical details and quantitative analyses of the AP blockage scheme in response to a HISDEP, proposed in this dissertation, will be modeled and discussed in the next chapter. This will be followed by appropriate simulation results in chapter four. Among other areas of contribution, one of the key aspects of this research work is on the unexplored aspect of nanosecond, high-intensity electric pulses for disruption of neural traffic. For all the modeling and analyses purposes, a cylindrical geometry with a constant cross-section has been assumed for simplicity without compromising the qualitative physics. As will be elaborated upon later, the original HH model has been modified to include an additional shunt membrane conductance in parallel to the ionic channel currents to account for the time-dependent flow through the electro-pores.

### 2.3.5 More recent modes and studies

Before wrapping up this literature review, it is perhaps appropriate to touch upon whole-body neural-signaling as it relates to medical malfunctions. In a sense, this aspect involves the “whole-body,” concept of a distributed network of neurons, and the electrical signaling times, durations and sequencing. For example, the generation of action potentials is usually not an isolated event but instead involves frequent signaling with information encrypted in the frequency, modulation and stochastic variability. Several medical conditions, such as epilepsy, originate from the malfunctioning of the neural network, or the improper signal generation. Normal physiological activity and perceptive response depends upon an extremely refined and synchronized neural behavior. Any disturbance from the norm (excessive or irregular activity, for example) can lead to severe complications including seizure and cardiac arrhythmia. Most of the work that has been reviewed here has dealt with singular AP generation and modulation or block in the continuum sense. However, the above mentioned irregularities in the neural network are valid, appropriate and germane issues that broadly fall under the purview of such electrical-based neural modeling. There have been efforts and attempts at

addressing problems and issues associated with such whole-body, neural signaling and its failures. The study of such instances that may be perceived as failure of neural stability or synchronization have incorporated multi-neural models in some form or multi-state environments where the activity level of one group of neural segment may or may not be causal. In some reports, this has been done as a focus on seizure dynamics using a nonlinear network [70], or employing chaos theory for the same [103] or cardiac activity [104]. All this points to the possibility that focused electrical stimulation can be used to alleviate some of these problems, akin to the transcutaneous electric nerve stimulator. Just as electrical stimulation proves to be an effective treatment for controlling heart disorders (such as arrhythmia) via “pacemakers,” it would seem natural to look to similar electrical stimulation for regulating and controlling neural disorders such as epilepsy. However, the above aspect through interesting remains outside the present scope of this dissertation research. It has been mentioned here, simply from the standpoint of completeness.

In this chapter, all relevant background research that related directly to this research work has been highlighted. The preface to the actual modeling details and simulation results, which follow in the subsequent chapters, has also been incorporated. The remainder of this dissertation will present the proposed simulation schemes for full body modeling, nerve segment model with action potential block methods, followed by simulation results in both these areas. The final chapter includes concluding remarks along with the road map of possible extension to this work.

## Chapter III

### Modeling Details and Numerical Implementation

#### 3.1 Full-body Modeling Scheme

In this section, details about the input data format, the overall modeling scheme and its rationale are presented. This is followed by the modeling approach for nerve segments and also the proposed method and its mathematical representation for AP blocks. However, before proceeding, it is perhaps prudent to discuss the representative structure (i.e., format) of any volumetric data that is typically encountered and needs to be used in modeling work. Once the data representation format has been established, it becomes easier to specify boundary conditions, the discretization scheme, and, consequently, the modeling schema.

##### 3.1.1 Input Format Details

Irrespective of the scan method or source (be it MRI, CAT scan or otherwise), almost any bio model data is 3-D in structure. Moreover, this volumetric data is always generated slice-wise. That means, that the scanning is done (either sequentially or in parallel) of multiple 2-D planes, which are then collated to form the volumetric data set. Finally, almost all such modern volumetric data sets are comprised of “voxels.” Unlike conventional “pixels” which are used to represent a point in 2-D space, voxels – a blend of volume and pixels - is used to represent an element in 3-D space. Unlike pixels, which include their coordinates, voxels do not contain their absolute spatial position. Instead, they are represented by their position relative to their neighbors. Therefore, once the scanning sequence is established, then based on the voxel index, its spatial coordinates can be computed.

To illustrate this point consider the following case where a cubic volume, as shown in figure 3.1, is the subject and has been discretized at 1 unit resolution. The unit could be any metric and hence is not specified in this discussion. Based on figure 3.1, one notes that there are 16 elements in the X dimension, 4 in the Y and 4 in the Z dimension. One can also see that the entire volume can be considered to be 4 stacks of either XY surfaces, 4 stacks of X-Z surfaces or 16 stacks of Y-Z surfaces. Either way, the total number of cells in this data set equals  $16*4*4 = 256$ . Assuming that each cell in this volume is comprised of a different type of tissue, we can assign them a unique identification code. Let this code be an integer that varies from 1~256.

Additionally, for simplicity, assume that these tissue cells are numbered sequentially along the X-Z plane. This is shown in figure 3.1.

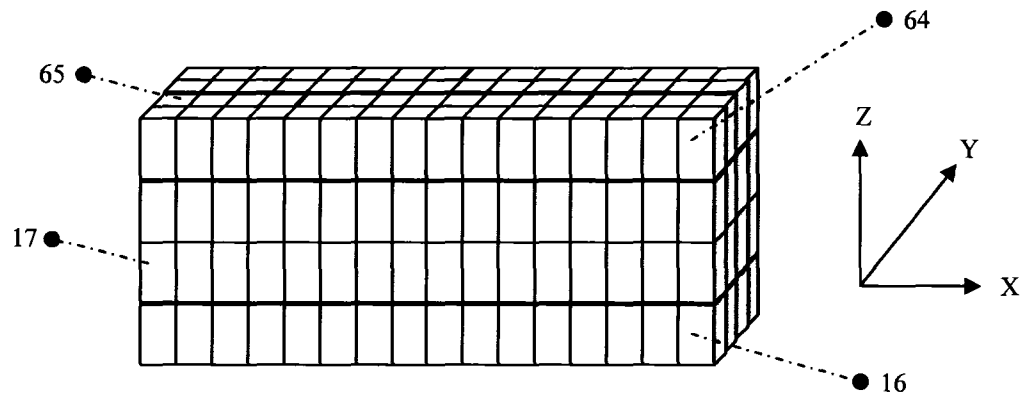


**Figure 3.1:** Sample volumetric data set with the tissue cell indexing scheme.

There are two methods of representing this volumetric block. The conventional method is to list all of the spatial coordinates and the tissue identification numbers. This leads to a list comprised of 4 vectors at the minimum. Expressed in the matrix format this looks like:

$$\begin{bmatrix} 1 & 1 & 1 & 1 \\ 2 & 1 & 1 & 2 \\ \cdot & \cdot & \cdot & \cdot \\ 16 & 1 & 1 & 16 \\ 1 & 1 & 2 & 17 \\ \cdot & \cdot & \cdot & \cdot \\ 16 & 1 & 4 & 64 \\ 1 & 2 & 4 & 65 \\ \cdot & \cdot & \cdot & \cdot \\ 16 & 4 & 4 & 256 \end{bmatrix}$$

In the above, matrix columns 1~3 represent the X, Y, Z coordinates respectively and column 4 represents the tissue identity. It should be noted that tissue identity number could be any value in the range (we have just kept the sequential numbering for brevity). Therefore, to represent this volumetric data using the explicit spatial coordinate scheme, the minimum amount of memory required (assuming a 4 byte integer) is  $256*4*4 = 4096$  Bytes = 4kB.



However, if we want to represent this using voxels, we need to fix the scanning order. Using the same sequential X-Z plane, all we need to do is list all the 256 tissue identification numbers in the *order* they were scanned. This results in a single column vector of 256 elements which requires  $256 * 4 = 1024$  Bytes = 1kB. The algorithm in appendix A.1 can be used to compute the x, y, z coordinates of a tissue with index  $n$  given that the total number of nodes in X, Y and Z dimensions are 16, 4 and 4 respectively. The savings in memory required between the two representation formats might not seem significantly different in this example. However, when using large data sets containing say, 100,000 data points, the savings can make or break a simulation.

For the purpose of developing a “full-body” modeling scheme, we have used volumetric data that was provided by the Research Laboratory at Brooks Air Force base in Texas. An example of the following is presented in figure 3.2.a and 3.2.b. These binary data files are in voxels format, which sequentially list the tissue identification number (IDN) for a preset scan resolution. The tissue IDNs are expressed using 2 Byte characters. The data stream sequence is the same as the one mentioned previously.

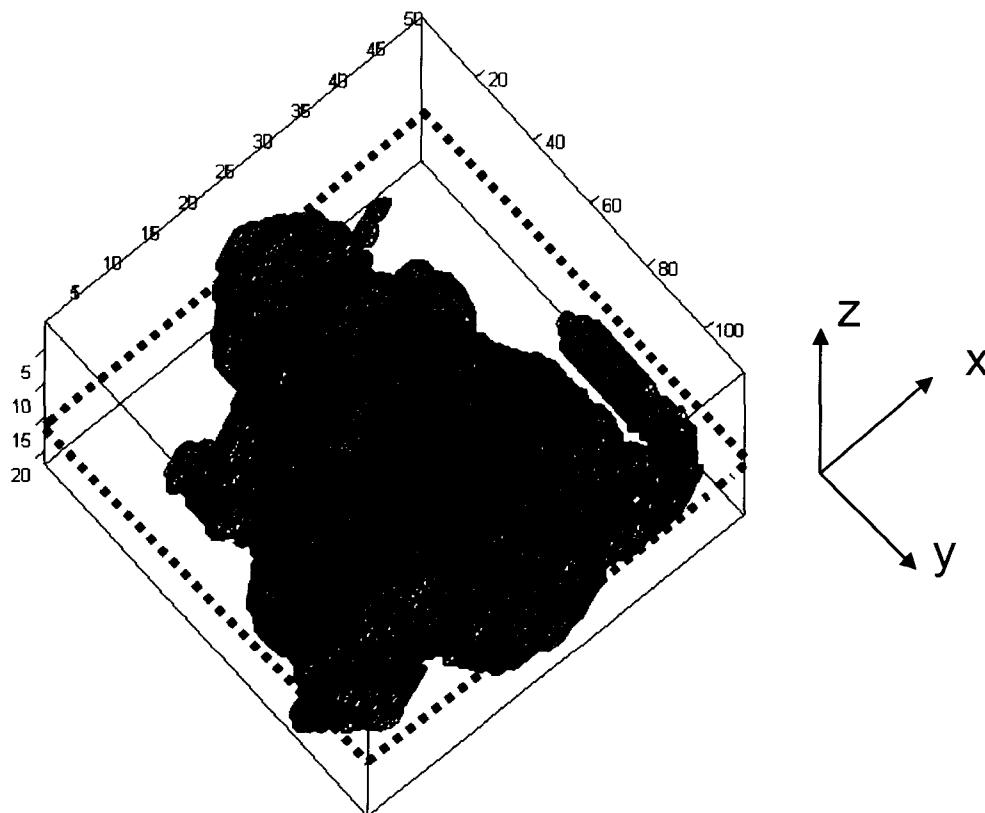


**Figure 3.2.a:** Visualization of a sample data file, with a rat as an example. The image is a wire frame model where the iso-surfaces are generated by patching non-air points. The dotted line illustrates a plane in the x-y plane. All dimensions are given in millimeters.

Almost all visualization schemes that exist for volumetric data use iso-surface patching techniques. A reasonable description is available in the MATLAB<sup>®</sup> documentation: “A patch graphics object is composed of one or more polygons that may or may not be connected. Patches are useful for modeling real-world objects such as airplanes or automobiles, and for drawing 2- or 3-D polygons of arbitrary shape.” So, if we consider a region that contains voxels for similar tissue types (or tissue types that we would like to treat as the same), their coordinates can then be expressed in two key forms to form these polygons:

- By specifying the coordinates of the vertices of each polygon;
- By specifying coordinates of only unique vertices and also defining the connection map for these vertices to form the different polygons.

A wire-frame model is simply created by not applying any fill to these polygons. In figure 3.2, we use the surrounding air (that exists) in the overall volumetric data as the threshold value. The wire is generated by not coloring the patch surfaces. This also highlights the air regions that exist *within* the animal’s body. To highlight the advantage of voxel format data representation, consider the following. This rat model contains a total of 127,908 data points, even though the actual rat is only 51mm by 22mm by 114 mm in dimension. The data file contains EXACTLY 127,908 one-byte entries. Consequently, the voxel format allows entire spatial representation to be represented using only 124 Kilobytes. Furthermore, only the tissue *type* of the various points needs to be listed. Comparing this to a full representation schema that is independent of the scanning sequence, the storage required would be three times. The reconstructed data is presented in 2-D slice format is shown in figure 3.2b. Herein we present the underlying tissue variability. The images are contour plots taken at different X-Y slices. The other advantage of voxel representation data form is that it is directly generated using most real world scanners. Now that the input data format has been detailed, in the next section the actual modeling scheme of electrical response for such full bodies is presented.

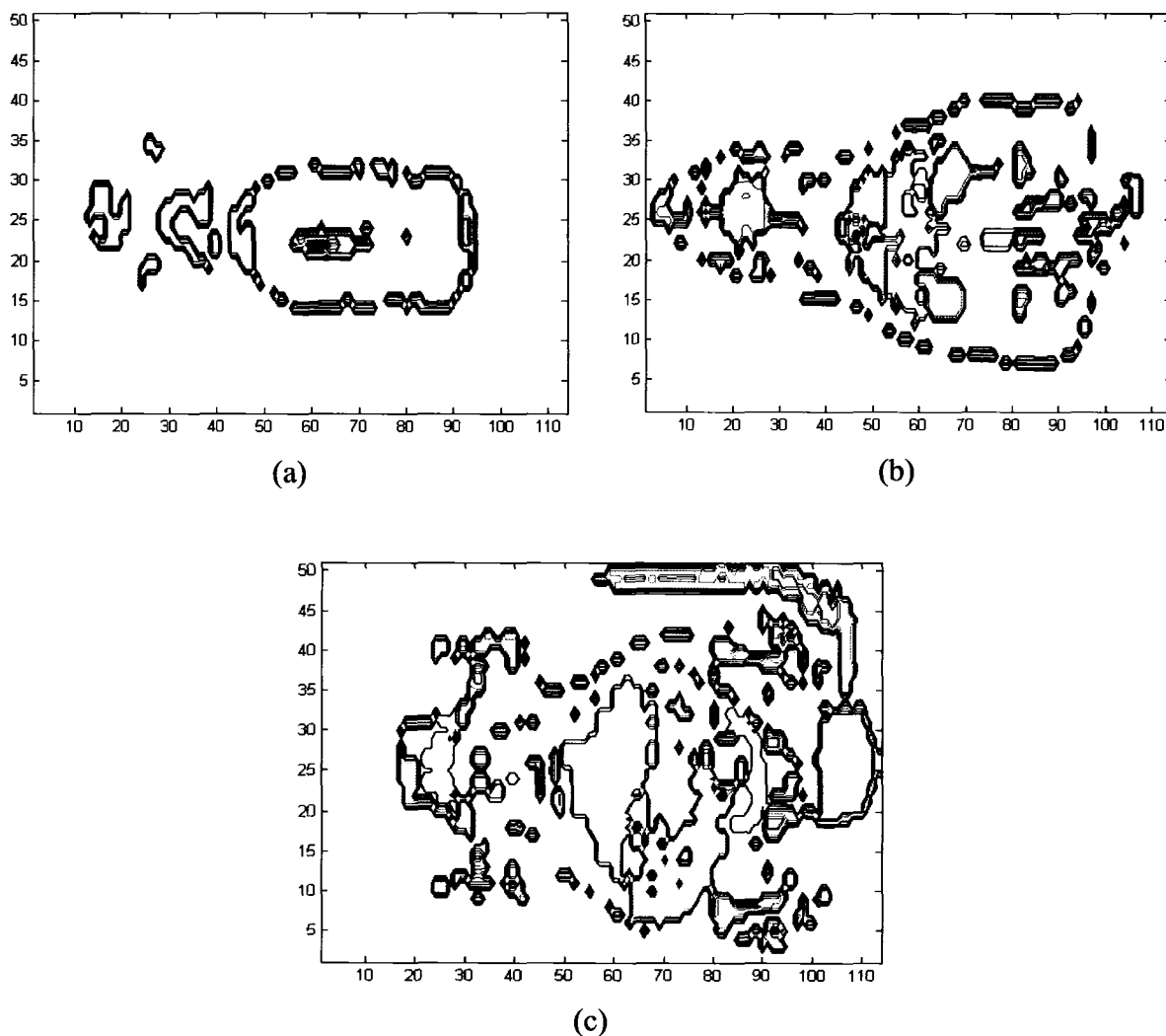


**Figure 3.2.b:** Cross-sections of the rat at different depths starting at (a) 5 mm, (b) 10 mm, and (c) 18 mm along the depth (Z axis).

### 3.1.2 Proposed Modeling Scheme

Based on the above-mentioned volumetric data and discretization scheme, we assume that each cell (i.e., biological sub-region) is characterized by a known conductivity ( $\sigma$ ) and permittivity ( $\epsilon$ ). From an electrical standpoint, each cell is represented as a parallel combination of an effective resistance (R) and capacitance (C). The RC combination at each node is connected to other RC combinations characterizing adjacent cells. Given the Cartesian nature of the simulation volume and the subsequent discretization, each cell can have *at most* 6 neighboring cells (nodes). The resulting electrical schematic is shown in figure 3.3.

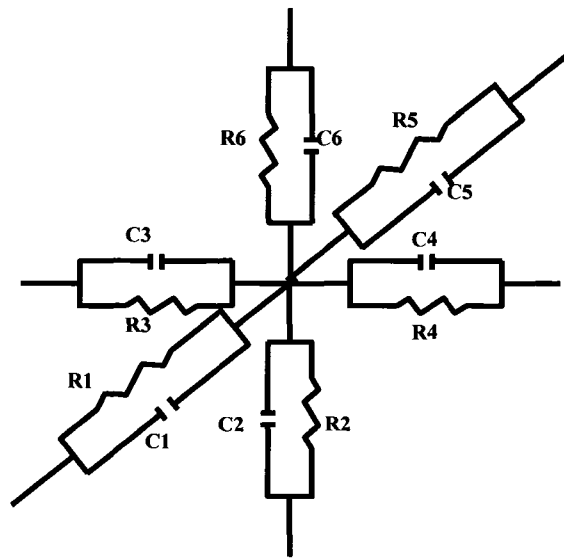


Fig. 3.3. Schematic of the discretized electrical model.

In the above figure, R1 and C1 represent the effective resistance and capacitance between the central node and its first neighboring node, while R5 and C5 are for the values for the 5<sup>th</sup> neighboring node. This effective capacitance and resistance is computed using the average  $\sigma$  and  $\epsilon$  of the current and its neighboring cell (node). A lookup table similar to the one shown in table 3.1 provides the actual  $\sigma$  and  $\epsilon$  values for each tissue type. Once this schematic is established, we can apply the current continuity to yield a set of coupled equations for nodal voltages. Time dependent values of the potential across each discretized sub-region and current distributions can then be directly obtained.

In theory, the voltages can be obtained through Kirchhoff's node analysis. At each node, equations of the type:

$$\sum \left[ \left( \frac{A\epsilon}{L} \right) \left( \frac{d(\Delta V)}{dt} \right) + \{ \Delta V \} \left[ \frac{A\sigma}{L} \right] \right] = 0 \quad , \quad (3.1.1)$$

based on the Kirchhoff's node analysis, are applied In equation(3.1.1),  $A$  is the cross-sectional area of each cell and  $L$  is the length. It can then be recast in a matrix form given by equation(3.1.2).

$$[M][\Delta V|_{t+\Delta t} - \Delta V|_t] = B(t) \quad . \quad (3.1.2)$$

In the above equation,  $\Delta V|_{t+\Delta t}$  denotes potential at time step  $t+\Delta t$ .  $[M]$  is the “mapping matrix” that is asymmetric in general, although a symmetric version which shall be detailed in Appendix A2 is also possible.

**Table 3.1.** Electrical parameters for various constituent tissues.

TissueName	Tissue ID	Sigma	Epsilon (real part)
AIR.(external)	0	0	1.00E+00
AIR.(internal)	1	0	1.00E+00
BILE	2	1.4	4.00E+00
BODY.FLUID	3	1.5	4.00E+00
EYE.(cornea)	4	0.4	4.00E+00
FAT	5	0.01	2.50E+00
LYMPH	6	0.5	4.00E+00
MUSCOUS.MEMBRANE	7	0.0004	4.00E+00
NAILS.(toes.and.fingers)	8	0.02	2.50E+00
NERVE.(spine)	11	0.006	4.00E+00
MUSCLE.	17	0.2	4.00E+00
HEART	25	0.05	4.00E+00
WHITE.MATTER	30	0.02	4.00E+00
STOMACH	48	0.5	4.00E+00
GLANDS	49	0.5	4.00E+00
BLOOD.VESSEL	65	0.25	4.00E+00
LIVER	68	0.02	4.00E+00
GALL.BLADDER	88	0.9	4.00E+00
SPLEEN	108	0.03	4.00E+00
CEREBELLUM	110	0.04	4.00E+00
BONE.(cortical)	111	0.02	2.50E+00
CARTILAGE.	133	0.15	4.00E+00
LIGAMENTS	142	0.25	4.00E+00
SKIN/DERMIS	143	0.0002	4.00E+00
INTESTINE.(large)	148	0.01	4.00E+00
TOOTH	152	0.02	2.50E+00
GRAY.MATTER	160	0.02	4.00E+00
EYE.(lens)	163	0.3	4.00E+00
LUNG.(outer)	164	0.2	4.00E+00
INTESTINE.(small)	168	0.5	4.00E+00
EYE.(sclera/wall)	183	0.5	4.00E+00
LUNG.(inner)	184	0.03	2.50E+00
PANCREAS	188	0.5	4.00E+00
BLOOD	189	0.7	4.00E+00
CEREBRALSPINALFLUID	190	2	4.00E+00
EYE.(retina)	203	0.5	4.00E+00
EYE.(aqueous.humour)	204	1.5	4.00E+00
KIDNEYS	207	0.05	4.00E+00
BONE.MARROW	209	0.0005	2.50E+00
BLADDER	227	0.2	2.50E+00

To understand the matrix  $[M]$ , we need to write down the nodal equations for each node. This is shown and discussed next. One of the most significant steps is to ensure the stability of the solutions. Given the fact that the capacitance of each cell is extremely small, the characteristic “RC” time constant of the system becomes low. Hence, in order to ensure accuracy and stability of the numerical system, we need to keep the time step extremely small. This leads to a severe

constraint on computational time and also prohibits the use of rapidly rising/falling pulse waveforms. To avoid these constraints, we employ the centre-averaged, implicit solution scheme. This can be understood by considering figure 3.4. It shows a simplified inter-connectivity outline of figure 3.3. The node in question is 2, and its neighbors are numbered 1~7. For the sake of complete information, it should also be mentioned that nodes 1,3 are along the x dimension, nodes 5,7 along the z, and nodes 4,6 along the y dimension. Using the present voxel indexing scheme this implies that if node 2 represents a node  $i$ , then the following the neighbors are actually indexed as:  $1 \rightarrow i-1$ ,  $3 \rightarrow i+1$ ,  $4 \rightarrow (i-nx*nx)$ ,  $6 \rightarrow i+(nx*nz)$ ,  $5 \rightarrow i-nx$  &  $7 \rightarrow i+nx$ , where  $nx$  is the number of nodes (cells) along the x dimension and  $nz$  along the z dimension.

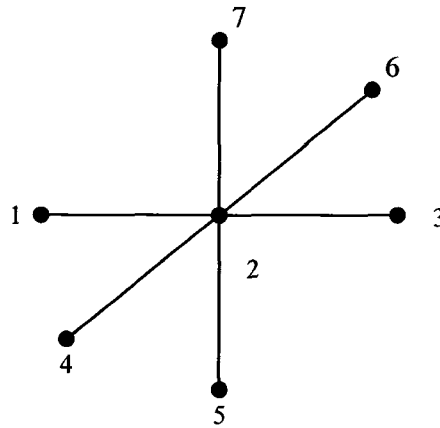


**Figure 3.4.** Simplified schematic to highlight the nodal links and node indexing.

The nodal equation at node 2 is then given by equation(3.1.3).

$$\begin{aligned}
 & \left( \frac{C_{21}}{\Delta t} \right) d[V_1 - V_2] + \left[ \frac{V_1^o - V_2^o}{2.R_{21}} \right] + \left[ \frac{V_1^n - V_2^n}{2.R_{21}} \right] + \dots \\
 & \left( \frac{C_{23}}{\Delta t} \right) d[V_3 - V_2] + \left[ \frac{V_3^o - V_2^o}{2.R_{23}} \right] + \left[ \frac{V_3^n - V_2^n}{2.R_{23}} \right] + \dots \\
 & \left( \frac{C_{24}}{\Delta t} \right) d[V_4 - V_2] + \left[ \frac{V_4^o - V_2^o}{2.R_{24}} \right] + \left[ \frac{V_4^n - V_2^n}{2.R_{24}} \right] + \dots \\
 & \left( \frac{C_{25}}{\Delta t} \right) d[V_5 - V_2] + \left[ \frac{V_5^o - V_2^o}{2.R_{25}} \right] + \left[ \frac{V_5^n - V_2^n}{2.R_{25}} \right] + \dots \\
 & \left( \frac{C_{26}}{\Delta t} \right) d[V_6 - V_2] + \left[ \frac{V_6^o - V_2^o}{2.R_{26}} \right] + \left[ \frac{V_6^n - V_2^n}{2.R_{26}} \right] + \dots \\
 & \left( \frac{C_{27}}{\Delta t} \right) d[V_7 - V_2] + \left[ \frac{V_7^o - V_2^o}{2.R_{27}} \right] + \left[ \frac{V_7^n - V_2^n}{2.R_{27}} \right] = 0
 \end{aligned} \tag{3.1.3}$$

In the above equation,  $V_i^o$  implies potential at node  $i$ , at the old time step and  $C_{25}, R_{25}$  represent the effective capacitance of the link between nodes 2 and 5 respectively. Further expanding the above equation yields:

$$\begin{aligned}
& \left( \frac{C_{21}}{\Delta t} \right) [V_1^n - V_2^n - V_1^o + V_2^o] + \left( \frac{C_{23}}{\Delta t} \right) [V_3^n - V_2^n - V_3^o + V_2^o] + \dots \\
& \left( \frac{C_{24}}{\Delta t} \right) [V_4^n - V_2^n - V_4^o + V_2^o] + \left( \frac{C_{25}}{\Delta t} \right) [V_5^n - V_2^n - V_5^o + V_2^o] + \dots \\
& \left( \frac{C_{26}}{\Delta t} \right) [V_6^n - V_2^n - V_6^o + V_2^o] + \left( \frac{C_{27}}{\Delta t} \right) [V_7^n - V_2^n - V_7^o + V_2^o] + \dots \\
& \left[ \frac{V_1^n - V_2^n}{2.R_{21}} \right] + \left[ \frac{V_3^n - V_2^n}{2.R_{23}} \right] + \left[ \frac{V_4^n - V_2^n}{2.R_{24}} \right] + \left[ \frac{V_5^n - V_2^n}{2.R_{25}} \right] + \dots \\
& \left[ \frac{V_6^n - V_2^n}{2.R_{26}} \right] + \left[ \frac{V_7^n - V_2^n}{2.R_{27}} \right] = - \left[ \frac{V_1^o - V_2^o}{2.R_{21}} \right] - \left[ \frac{V_3^o - V_2^o}{2.R_{23}} \right] - \dots \\
& \left[ \frac{V_4^o - V_2^o}{2.R_{24}} \right] - \left[ \frac{V_5^o - V_2^o}{2.R_{25}} \right] - \left[ \frac{V_6^o - V_2^o}{2.R_{26}} \right] - \left[ \frac{V_7^o - V_2^o}{2.R_{27}} \right]
\end{aligned} \tag{3.1.4}$$

Separating the old and new terms to either side of the equation results in:

$$\begin{aligned}
& V_2^n \left[ \sum_i \left( \frac{C_{2i}}{\Delta t} + \frac{1}{2R_{2i}} \right) \right] - V_1^n \left[ \frac{C_{21}}{\Delta t} + \frac{1}{2R_{21}} \right] - V_3^n \left[ \frac{C_{23}}{\Delta t} + \frac{1}{2R_{23}} \right] - \dots \\
& V_4^n \left[ \frac{C_{24}}{\Delta t} + \frac{1}{2R_{24}} \right] - V_5^n \left[ \frac{C_{25}}{\Delta t} + \frac{1}{2R_{25}} \right] - V_6^n \left[ \frac{C_{26}}{\Delta t} + \frac{1}{2R_{26}} \right] - V_7^n \left[ \frac{C_{27}}{\Delta t} + \frac{1}{2R_{27}} \right] = \\
& (V_1^o - V_2^o) \left[ \frac{1}{2R_{21}} - \frac{C_{21}}{\Delta t} \right] + (V_3^o - V_2^o) \left[ \frac{1}{2R_{23}} - \frac{C_{23}}{\Delta t} \right] + (V_4^o - V_2^o) \left[ \frac{1}{2R_{24}} - \frac{C_{24}}{\Delta t} \right] + \dots \\
& (V_5^o - V_2^o) \left[ \frac{1}{2R_{25}} - \frac{C_{25}}{\Delta t} \right] + (V_6^o - V_2^o) \left[ \frac{1}{2R_{26}} - \frac{C_{26}}{\Delta t} \right] + (V_7^o - V_2^o) \left[ \frac{1}{2R_{27}} - \frac{C_{27}}{\Delta t} \right]
\end{aligned} \tag{3.1.5}$$

For notational simplicity, we assign the following variables to terms on the left hand side (LHS):

$$\begin{aligned}
k_1 &= \left[ \frac{C_{21}}{\Delta t} + \frac{1}{2R_{21}} \right]; k_3 = \left[ \frac{C_{23}}{\Delta t} + \frac{1}{2R_{23}} \right]; \\
k_4 &= \left[ \frac{C_{24}}{\Delta t} + \frac{1}{2R_{24}} \right]; k_5 = \left[ \frac{C_{25}}{\Delta t} + \frac{1}{2R_{25}} \right]; \\
k_6 &= \left[ \frac{C_{26}}{\Delta t} + \frac{1}{2R_{26}} \right]; k_7 = \left[ \frac{C_{27}}{\Delta t} + \frac{1}{2R_{27}} \right]
\end{aligned}$$

and the following for those on the right hand side( RHS):

$$\begin{aligned}
m_1 &= \left[ \frac{1}{2R_{21}} - \frac{C_{21}}{\Delta t} \right]; m_3 = \left[ \frac{1}{2R_{23}} - \frac{C_{23}}{\Delta t} \right]; \\
m_4 &= \left[ \frac{1}{2R_{24}} - \frac{C_{24}}{\Delta t} \right]; m_5 = \left[ \frac{1}{2R_{25}} - \frac{C_{25}}{\Delta t} \right]; \\
m_6 &= \left[ \frac{1}{2R_{26}} - \frac{C_{26}}{\Delta t} \right]; m_7 = \left[ \frac{1}{2R_{27}} - \frac{C_{27}}{\Delta t} \right] .
\end{aligned}$$

Equation (3.1.5) can then be recast as:

$$\begin{aligned}
&V_2^n [k_1 + k_3 + k_4 + k_5 + k_6 + k_7] - \dots \\
&V_1^n k_1 - V_3^n k_3 - V_4^n k_4 - V_5^n k_5 - V_6^n k_6 - V_7^n k_7 = \\
&V_1^o m_1 + V_3^o m_3 + V_4^o m_4 + V_5^o m_5 + V_6^o m_6 + V_7^o m_7 - \dots \\
&V_2^o [m_1 + m_3 + m_4 + m_5 + m_6 + m_7]
\end{aligned} \tag{3.1.6}$$

The left hand side of equation (3.1.6) contains terms involving the current node of interest ( $V_2$ ) and its neighboring nodes. Given that there are  $N$  nodes, the resulting  $N$  coupled equations when cast in matrix form, yield a system of simultaneous equations that has just the same form as equation (3.1.2). Now we are in a better position to discuss the structure of the matrix  $[\mathbf{M}]$ . Since each row of this matrix can contain at the *utmost* 7 *non-zero* entries (including the diagonal), this matrix is extremely sparse. If the applied stimulus is a potential pulse train, then those nodes that serve as electrode locations (i.e. connected to an Anode or Cathode) contain only *one* element (at the diagonal). However, if the applied stimulus is a current pulse train, then only cathode location nodes contain one diagonal element. This is simply due to the fact that application of KCL at the anode location in a current stimulated system does not provide *a-priori* knowledge of the potential at the anode location. However, since Cathode is always grounded (the chosen reference potential), consequently  $V_i^n = V_i^o = 0$ .



In the next subsection, we examine how and why this sparse nature of  $[M]$  plays a vital role in the development of this modeling scheme. It ends up being the single most critical factor in the subsequent performance during the solution phase.

### 3.1.2.1 Matrix Sparsity and its Significance

To highlight the sparsity of the matrix and its significance, consider figure 3.5. In this particular case, the underlying tissue model was a  $10*10*10$  node saline brick. The matrix  $[M]$  has a dimension of  $1000*1000$ . However, the actual non-zero entries in this particular case are only 6378. Another key point to note is that even though the structure of the matrix *looks* symmetric, it is NOT. The reason is that even though equation (3.1.5) leads to the condition that  $a_{i,j} = a_{j,i}$  in the coefficient matrix, this is only valid for non-electrode nodes. The applied input potential waveform essentially imposes the Dirichlet boundary conditions at the electrode locations (both Anode and Cathode). Thus, these rows contain a single diagonal element (1) and also disturb the symmetric nature of  $[M]$ . It should be noted that in case of current stimulus, this applies only to cathode (grounded) locations. This lack of symmetry is a serious operational restriction that causes increase in factorization time, increase in memory requirement, as well as limited solver possibilities.

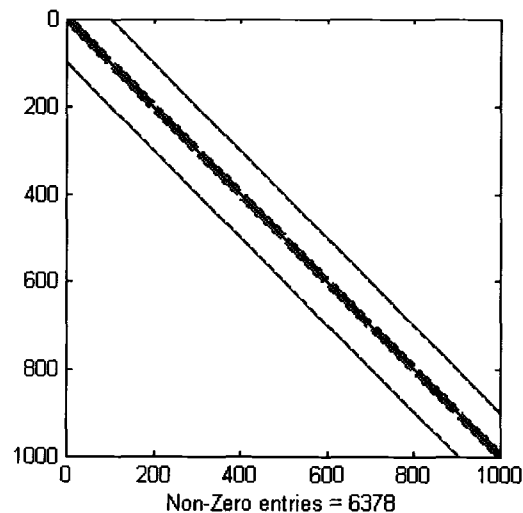


**Figure 3.5.** Figure showing the non-zero entries in case of a  $10*10*10$  node, saline brick model with a particular electrode placement.

In any case, the 6378 non-zero entries lead to a sparsity index of 99.362%. If this matrix was expressed in its full form, 99.362% of the entries would not have any significance because they would all be zero. The biggest implication of this is in the memory or storage required. Consider

the following three different storage options. Assuming  $[M]$  is square and has an order of  $k^2$  i.e. there are  $k$  rows and columns. Also, let the number of non-zero entries (NNZ) be  $m$ . Finally, it is assumed that 8 byte floating precision is used to store these numbers.

- *Full storage* - requires  $k^2*8$  Bytes (at the minimum).
- *Non zero storage* – requires 3 vectors (two for the X, Y locations and the third for the actual value). Using 4 byte integers for X, Y vectors, one needs a total of:  $4*2m + m*8 = 16m$  Bytes.
- *Compressed Row Storage Scheme (sparse storage scheme)*: This method involves three vectors (much like the previous scheme). The first vector – let's say called ISR has a dimension of  $(k+1)*1$ .  $ISR(j+1)-ISR(j)$  equals the number of non zero elements in row  $j$ . The second vector, let's call it YLOC, has a dimension  $(m*1)$ .  $YLOC(p)$  contains the column number of non-zero element ( $p$ ) with  $1 \leq P \leq m$ . Finally the third vector, let's call it RVAL, also has a dimension of  $(m*1)$ , while  $RVAL(p)$  contains the actual value of element  $p$ . Given this information, and using 4 Bytes integers for ISR, YLOC and 8 Byte floating values for RVAL, the total storage required is:  $[4*(k+1+m)]+8*m$  Bytes. A more detailed description of this storage scheme is presented in appendix A3.

For the sake of true comparative analysis, we use values of:  $m=6378$ ,  $k=1000$ . This yields: (i) Full storage: 7.6294 MB. (ii) Non-zero storage: 0.0973 MB, and (iii) Compressed Row Storage: 0.0768 MB. This storage saving *might* not seem significant, however, as the order of  $[M]$  increases, and the sparsity index also increases, the difference in storage requirements of the three schemes becomes more evident. The caveat is that this saving in the memory storage comes at the price of computational complexity. To illustrate this, we refer back to equation (3.1.2), which can be re-written as:

$$[M]x = [b] \quad (3.1.7)$$

The conventional method of solution of this equation is given by:

$$x = [M]^{-1}[b] \quad (3.1.8)$$

There are quite a few problems with the computations of  $[M]^{-1}$  (inverse of matrix  $[M]$ ). Some of the key issues and problems are as follows:

- a) A sparse matrix when inverted leads to a completely dense matrix. That typically means that the storage requirement suddenly increases to  $k^2*8$  Bytes.

- b) Typical inversion routines require a working space of *at least*  $k^2 \cdot 8$  Bytes, *apart* from the original storage requirement for the matrix.
- c) On most operating systems (whether Win32 or UNIX), there is a cap imposed by the operating system on each process (thread), irrespective of the physical memory (RAM) available. As an example – Windows (Win32) imposes a maximum of 1.5GB of physical memory to each process. This includes the memory requirement for the actual computation software and its own workspace (which is where any matrix to be inverted would be stored). Once this cap is crossed – the OS starts allocating *virtual memory* which is *significantly* slower.

The other methods of solving a system of linear equations as given by equation (3.1.7) are: (i) direct solvers or (ii) iterative solvers. For the purpose of this dissertation (keeping in mind the nature of the problem size), we only employ direct solvers based on the Gaussian elimination method. More details and discussions on sparsity will be presented in the later sections. In the next section the solution method for the set of linear equations is presented.

#### 3.1.2.2 Solution Scheme Overview for the Full Body Models.

The usual way of solving system of equations represented by equation (3.1.7) using a direct method is to perform the *triangular factorization (LU decomposition)* of  $[M]$ . This leads to:

$$[M] = [L][U] \quad , \quad (3.1.9)$$

where  $U$  and  $L$  are the upper and lower triangular matrices. The sparse structure of  $[M]$  depends upon the source from which system of equations (3.1.7) has been created. Due to “factorization fill-in,” even if  $[M]$  is sparse, then  $[L]$  and  $[U]$  are also sparse, though to a *lesser degree*. What this means is that upon factorization, the net storage requirement of the factored form of  $[M]$  is actually greater. This “fill-in” can be reduced by modifying the *structure* of  $[M]$  through re-ordering the variables and permuting the equations. Even though this operation usually does little for the solution efficiency, it is a vital practical step simply because the fill in coefficients can be as high as 600x leading to make or break situations of the actual solution process.

For purposes of highlighting the significance of reordering, consider the matrix  $[M]$  as shown in figure 3.5 (with 8 less electrode points). One of the reordering methods that is quite common is the COLumn Approximate Minimum Degree (COLAMD) method. The permutation matrix  $P$  is shown in figure 3.5(b). The permutation matrix  $P$  is a type of mapping matrix that defines

how the rows and columns of any original matrix have been shifted to yield the reordered matrix. It contains exactly one entry per row and column and zero elsewhere. The original matrix when factored without any reordering(c) results in 180547 non-zero entries. Subtracting the diagonal entries (as they are permanent), we get a fill in factor of:  $\frac{(180547-1000)}{6366} = 28.2041$ . Comparing this with the re-ordered case (d), the fill in factor equals:  $\frac{(119420-1000)}{6366} = 18.6019$ . This fill-in increases as the problem size increases. A case in point is the rat model (used extensively in this thesis work) with 127908 nodes. Without reordering, the total “fill-in” is ~100 times. However, with reordering this fill-in can be reduced to ~50x. For the purpose of this dissertation work, we employ the sparse matrix reordering routines from the METIS package [105] – specifically the METIS\_NodeND that computes the permutation vectors using multi-level nested dissection algorithm. Since discussion of such dissection algorithms are beyond the scope of this current dissertation, it will not be presented.

Once the Lower and Upper triangular factor matrices are computed the solution for  $x$  is obtained by performing the forward and backward substitution. Assuming that  $[\mathbf{w}]$  and  $\mathbf{b}$  are temporary working space and the right hand side vector respectively the following equations explain these steps.

$$\begin{aligned} [\mathbf{M}]^{-1} &= [\mathbf{U}]^{-1}[\mathbf{L}]^{-1} \\ \text{if } :[\mathbf{w}] &= [\mathbf{L}]^{-1}[\mathbf{b}] \\ x &= [\mathbf{U}]^{-1}[\mathbf{w}] \end{aligned} \quad . \quad (3.1.10)$$

Since  $[\mathbf{L}]$  and  $[\mathbf{b}]$  are known,  $[\mathbf{w}]$  is easily computable. This process is known as *forward substitution*. Once  $[\mathbf{w}]$  is ready,  $x$  is obtained using *backward substitution* with the last equation taking the form  $x_n = w_n$ . Even though it has been mentioned that  $[\mathbf{M}]$  is factored into the  $[\mathbf{L}]$  and  $[\mathbf{U}]$  factors, it is only prudent to explain why LU decomposition is followed by factorization steps. In the system of equations that result from the full body modeling (refer to equation(3.1.5), we note that the  $[\mathbf{M}]$  does not change. Also crucial to note is that  $[\mathbf{b}]_{t+\Delta t} = f([\mathbf{b}]_t)$ . These two aspects indicate that solution of this system of equations over the entire applied pulse steps can be performed by computing  $[\mathbf{L}]$ ,  $[\mathbf{U}]$  once, and then repeatedly solving equations(3.1.10).

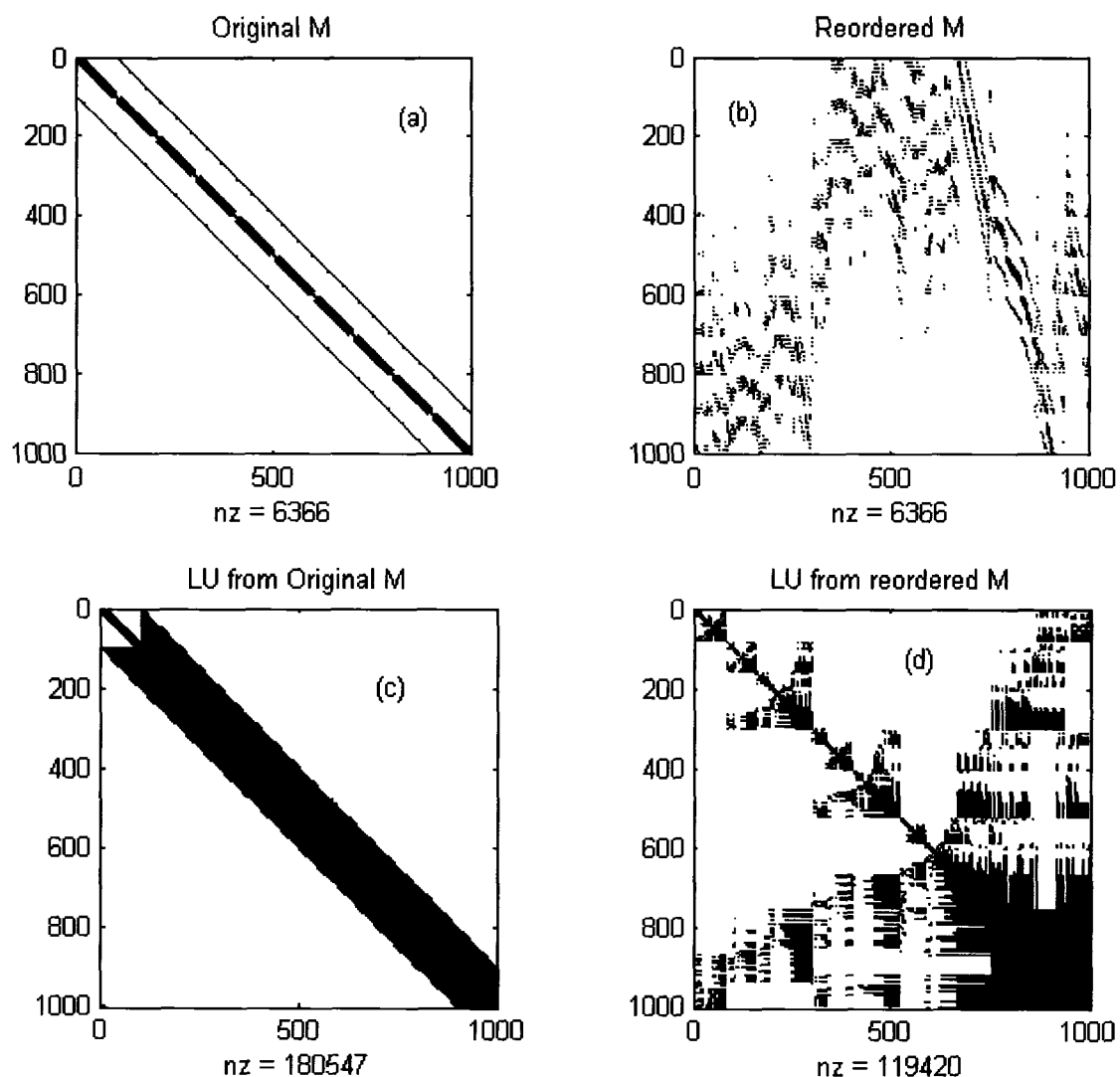


**Figure 3.6.** (a) Original coefficient matrix. (b) Reordered form of the original coefficient matrix (c) Non zero entries for L and U matrices computed without reordering M (d) Non-zero entries for L and U matrices computer after reordering M.

Without listing the details explicitly, the use of direct Gaussian Elimination to solve this system of equation over the entire applied stimuli steps would require the factorization to be performed at *each step*. The following set of equations list the operative steps for a LU factorization of a given matrix  $[M]$ . The equations are for a general matrix (sparse or otherwise).

For  $j=1, 2 \dots N$ , compute

$$u_{1j} = m_{1j} \quad , \quad (3.1.11)$$

$$u_{ij} = m_{ij} - \sum_{k=1}^{i-1} l_{ik} u_{kj}; i=2 \dots j, \quad (3.1.12)$$

$$\text{and, } l_{ij} = \frac{1}{u_{jj}} \left( m_{ij} - \sum_{k=1}^{j-1} l_{ik} u_{kj} \right); i=j+1 \dots N. \quad (3.1.13)$$

One of the peripheral advantages of LU decomposition is that we can compute the determinant of  $[\mathbf{M}]$ :

$$|\mathbf{M}| = |\mathbf{L}| \cdot |\mathbf{U}| = u_{11} u_{22} \dots u_{NN}. \quad (3.1.14)$$

The equations above also highlight the advantages of solution using LU decomposition versus the Gaussian elimination method, in this particular modeling scheme. Since equations (3.1.11) ~ (3.1.13) do not involve the  $[\mathbf{b}]$  vector, we need to perform this factorization step only once. Needless to say, this gives a definite advantage when solving the system of equations for a sequential stimulus pulse with multiple time steps. With the simulation scheme and the principal solution methodology laid out, the next two of sections list the need and details of converting this to a distributed solution scheme.

### 3.1.3 Distributed Algorithm Details

Full body modeling involves quite a large number of discrete points (nodes), and consequently, memory available for solution becomes a critical factor. Direct inversion is clearly not viable and using other solution schemes such as LU decomposition, which definitely allow for a larger simulation size to be solved for a given memory capacity, would benefit greatly, if the most memory and computation intensive operation of the entire solution scheme was distributed. However, before a distributed scheme of solution is implemented, the following key characteristics intrinsic to the proposed modeling scheme need to be borne in mind.

1. The system of equations gives rise to an asymmetric  $[\mathbf{M}]$  or an asymmetric coefficient matrix.
2.  $[\mathbf{M}]$  is extremely sparse, and yet, the factors are not quite as much.
3. Sparsity in factors can be improved with re-ordering of  $[\mathbf{M}]$ .
4. Since  $[\mathbf{b}]_{t+\Delta t} = f([\mathbf{b}]_t)$ , this implies that the equations are coupled in time, and consequently, such systems cannot be parallelized in time.

5. From a deployment perspective, it's better if the solver employs distributed memory architecture – especially given that shared memory systems are typically limited in the number of CPUs that are available.

Based on the above points, the optimal solver would be one that can solve sparse systems that are asymmetric and also allow for different reordering methods prior to factorization. A rather detailed survey of the available solver packages available in the open source community finally leads to “SuperLU\_DIST” [106]. This is a distributed version of a “general purpose library for the direct solution of large, sparse, nonsymmetric system of linear equations on high performance machines.” The other advantage of this package is that apart from providing internal reordering routines, it supports external reordering packages. However, the one limiting aspect is that during factorization phase, if the default memory allocation for factorization is not sufficient, then this factor needs to be modified and the subroutine re-linked through re-compilation. Like any other sparse solver, the onus lies on the user to provide the matrix **[M]** in a sparse format that must be ordered. Also, if an external reordering routine is being used, then the user must provide either the permutation vector or **[M]** in the reordered and sparse format.

#### 3.1.3.1 Algorithm Process Flow Diagram

The process flow of the distributed version of the solution scheme is now presented. Since Message Passing Interface (MPI) is also used, a process grid is classified, comprised of  $n$  processors, with the master being identified with IDN 0, and  $n-1$  slave processors with IDNs  $1 \sim n-1$ . In the flow diagram, the critical processes of setting up the **[M]** in the sparse format have been highlighted. For the sake of thoroughness, this section is also presented as pseudo-code in section 3.1.3.2.

The other key point regarding the following flow-diagram is that, in case the simulation size is not *big enough*, the memory saving achieved by reordering is not offset by the additional computation time required. Consequently, there are decision blocks that account for whether or not *METIS* is being called for reordering.

#### 3.1.3.2 Coefficient Matrix Setup in Compressed Row Storage Scheme

The following is the pseudo-code for the steps involved in setting up the **[M]** in the compressed row storage scheme. It is assumed that bio model has  $n$  nodes. Equation (3.1.6) is also referenced.

---

```
allocate ISR(n+1), ICOLTEMP(7*n) and RVTEMP(7*n)
initialize ISR(1) to 1
initialize ISRCOUNTER to 2, COLCOUNTER to 1, nodecounter to 1
```

```

WHILE nodecounter is less than  $n$  DO
  IF nodecounter EQUALS Anode OR nodecounter EQUALS Cathode THEN
     $ISR(ISRCOUNT) \leftarrow ISR(ISRCOUNT-1)+1$ 
    increment ISRCOUNT by 1
     $ICOLTEMP(COLCOUNTER) \leftarrow \mathbf{nodecounter}$ 
     $RVTEMP(COLCOUNTER) \leftarrow 1.0$ 
    increment COLCOUNTER by1
  OTHERWISE
    compute number of neighboring nodes for nodecounter (NBR)
     $ISR(ISRCOUNT) \leftarrow \mathbf{NBR}+1$ 
    increment ISRCOUNT by 1
    FOR each neighboring node DO
      compute  $k_i$ 
       $ICOLTEMP(COLCOUNTER) \leftarrow$  current neighbor index.
       $RVTEMP(COLCOUNTER) \leftarrow k_i$ 
       $SUM \leftarrow SUM+ k_i$ 
      increment COLCOUNTER by1
    END-DO
     $ICOLTEMP(COLCOUNTER) \leftarrow \mathbf{nodecounter}$ 
     $RVTEMP(COLCOUNTER) \leftarrow SUM$ 
    increment COLCOUNTER by1
END-WHILE
totalelements  $\leftarrow ISR(n+1)-1$ 
trim ICOLTEMP and RVTEMP to correct size (totalelements)
DEALLOCATE extra memory locations ( $7*n - (ISR(n+1)-1)$ )

```

---

It should also be mentioned that the raw process grid (or the number of processors as scheduled at job submission time) are mapped in a rectangular grid such that they can be factored using integral multiples of 1~6 rows. Any extra processors assigned are rejected from the process grid. Finally, in the spirit of memory conservation, the result file is written in binary format using 8 Byte floating-point precision. This keeps the output file size smaller compared to an ASCII format, which is definitely advantageous when transferring the same from clusters to workstations for subsequent analysis and visualization.



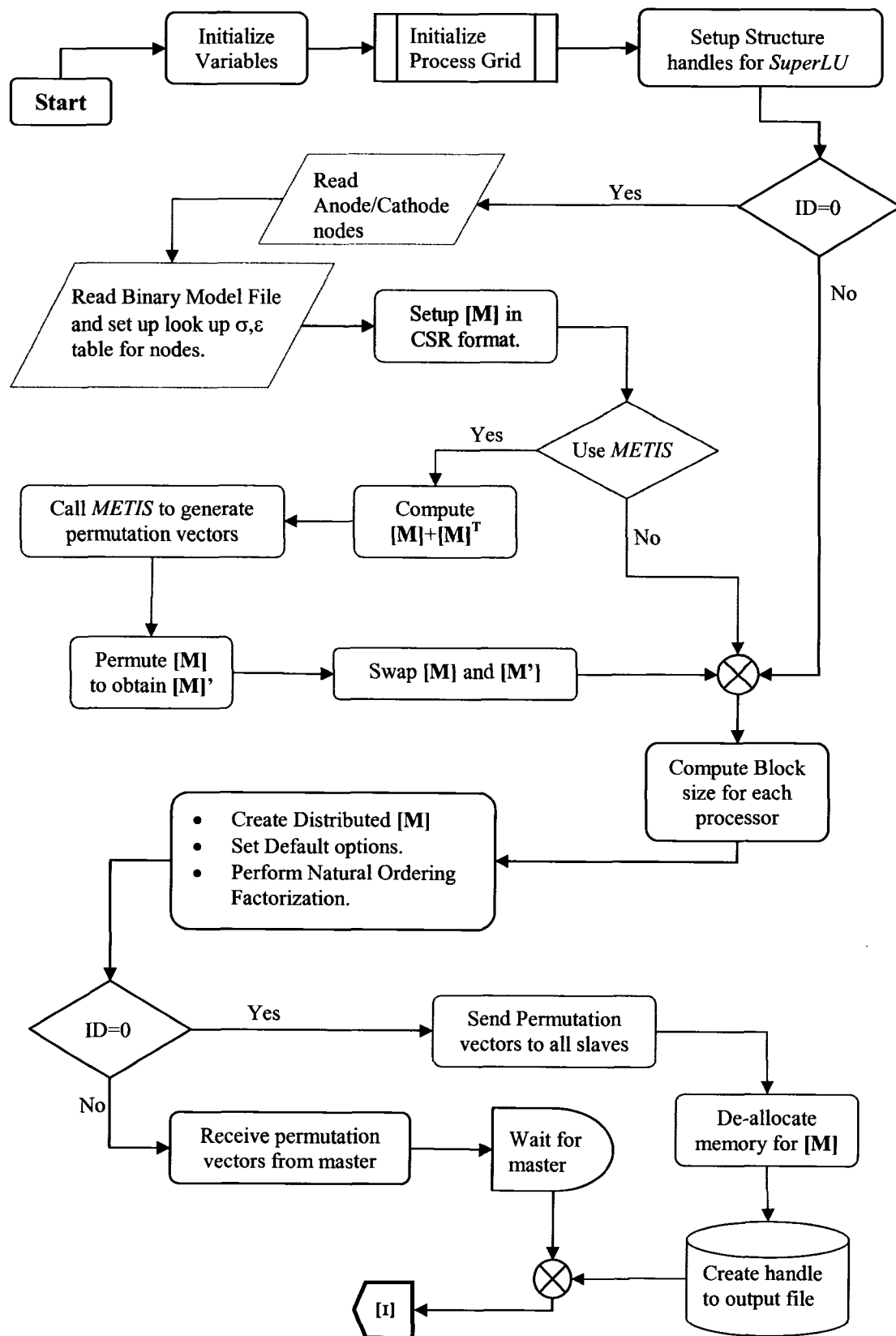


**Figure 3.7(a):** Process flow diagram for the distributed scheme of full body modeling.

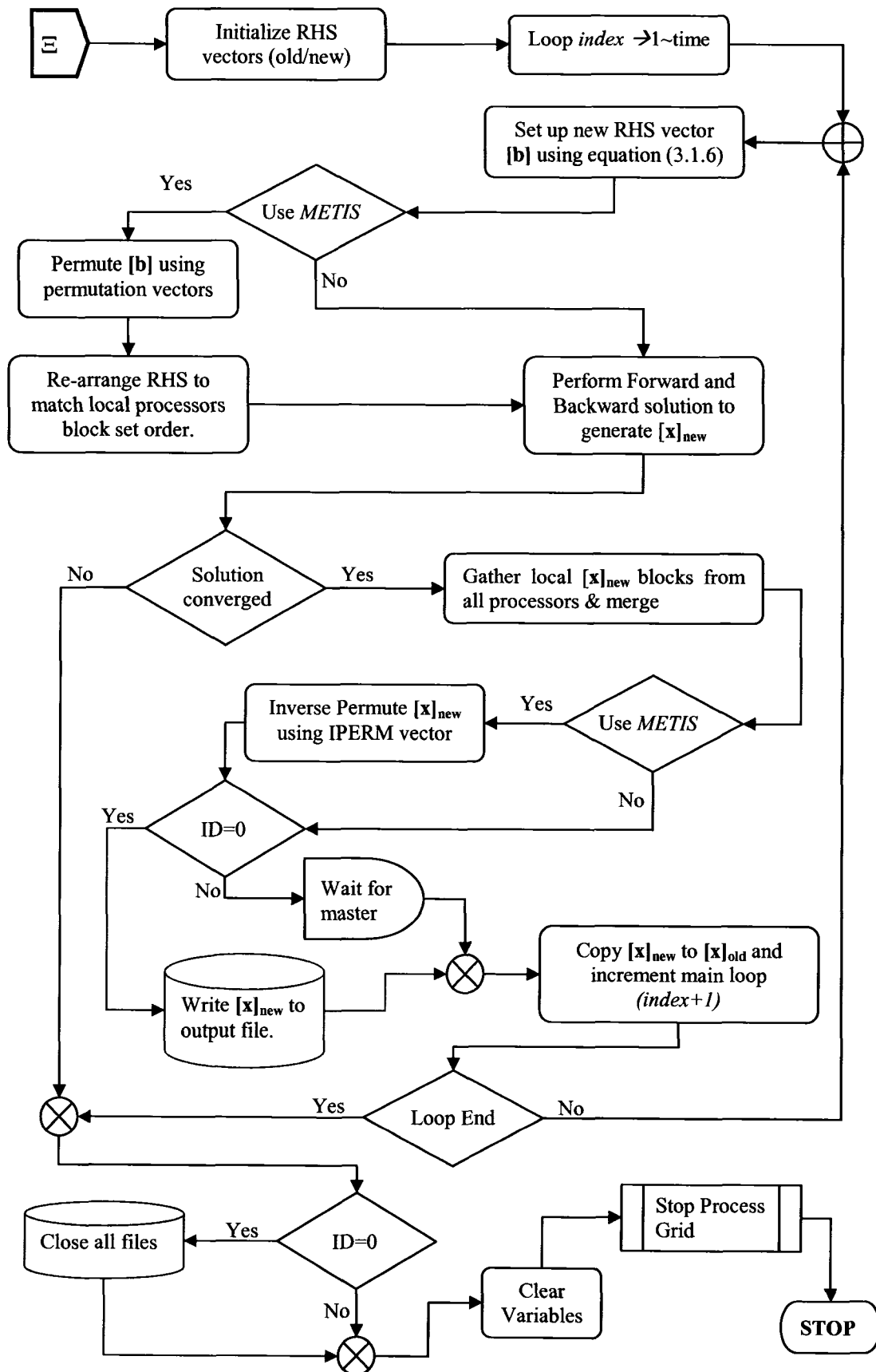


Figure 3.7(b): Process flow diagram (contd.).

### 3.2 Modeling Neural Traffic Interruption Methods

Subsequent sections of chapter 3 will be used to present details on nerve segment modeling (specifically unmyelinated and myelinated nerves). Also presented will be methods that have been proposed for action potential (AP) block as well for a novel scheme that employs High Intensity, Short Duration Electric Pulses (HISDEPs) for a robust and repeatable AP block. However, because the AP block methods build on the existing distributed cable model of the nerve, it is prudent to look at its details before any AP block method is presented.

#### 3.2.1 Distributed Cable Model for Representing the Unmyelinated Nerve Segment

The original distributed cable model used to represent the unmyelinated nerve segments was first proposed by Hodgkin-Huxley [62]. Other numerical implementation and changes were proposed by Cooley and Dodge [107] followed by McNeal [59] and Rattay [4, 5, 33]. As a one-dimensional system, the entire nerve is considered to be spatially discretized into nodes with the axonal resistances, and other ionic channels are represented in the form given in figure 3.8. In the model representation of Fig. 3.8,  $R_a$  and  $C_m$  represent the axonal resistance and membrane capacitance, respectively, while,  $G_{Na}$ ,  $G_K$  and  $G_L$  represent the conductivity of sodium ( $Na^+$ ), potassium ( $K^+$ ) and the leakage channels. Other elements such as  $E_{Na}$ ,  $E_K$  and  $E_L$  are the biasing potentials for the  $Na^+$ ,  $K^+$  and leakage channels. Finally,  $V_i$ ,  $V_{i-1}$  and  $V_{i+1}$  represent the internal membrane potentials at the node of interest ( $i$ ) and its neighboring nodes. The equations for the AP propagation are given by:

$$\frac{V_{i-1}^{k+1} - V_i^{k+1}}{R_a} - \frac{V_i^{k+1} - V_{i+1}^{k+1}}{R_a} + I_{inj}^{k+1} - I_{ch}^{k+1} = C_m \dot{V}_i^{k+1} \quad , \quad (3.2.1)$$

$$\text{and, } \frac{V_{i-1}^k - V_i^k}{R_a} - \frac{V_i^k - V_{i+1}^k}{R_a} + I_{inj}^k - I_{ch}^k = C_m \dot{V}_i^k \quad , \quad (3.2.2)$$

where  $V_{i-1}^{k+1}$  represents the internal membrane potential at time step  $k+1$ ,  $I_{ch}$  is the channel current and  $I_{inj}$  is the injected current pulse (for initiating the AP or for initiating a block or a given node). Using the mid-point implicit solution scheme, the potentials at times  $k$  and  $k+1$  are related using [107]:

$$V_i^{k+1} = V_i^k + \frac{\Delta t}{2} [\dot{V}_i^k + \dot{V}_i^{k+1}] \quad . \quad (3.2.3)$$

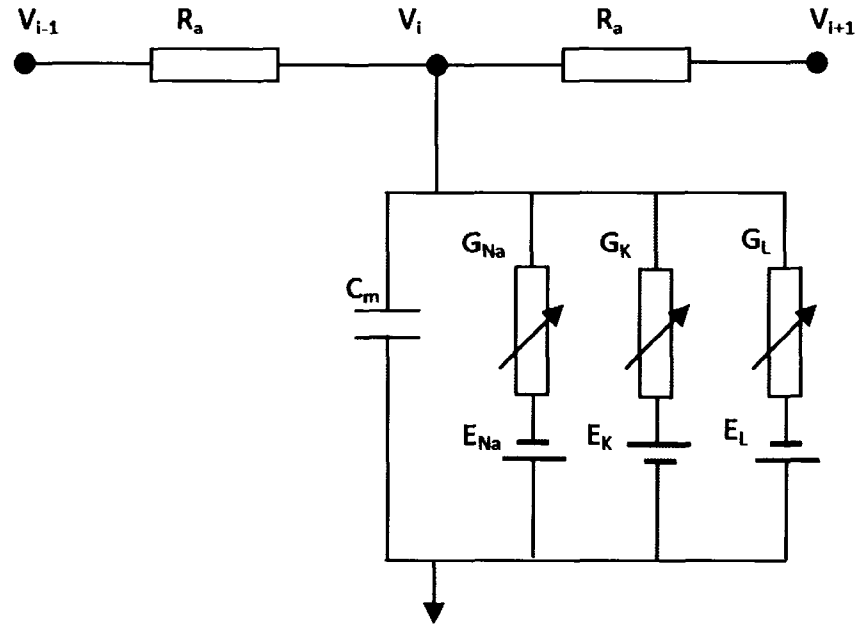


**Figure 3.8:** Equivalent circuit representing the cable line model for the unmyelinated nerve segment.

It may be noted that in equations (3.2.1)–(3.2.3), even though  $V_i$  refer to the internal node voltages, these are related to the trans-membrane voltage  $V^*$  by:

$$V_i = V_e + V_{rest} + V^* \quad , \quad (3.2.4)$$

where,  $V_{rest}$  is a constant resting potential and  $V_e$  is the external potential taken to be zero (the reference ground potential). Equations (3.2.1) ~ (3.2.3) also turn out to be applicable for  $V^*$ . The channel current,  $I_{ch}$ , which is a non-linear ionic current, is given by the analytical expression [62]:

$$I_{ch}^{k+1} = ft \left[ g_{Na} m_i^{3k+1} h_i^{k+1} (V_i^{k+1} - V_{Na}) + g_K n_i^{4k+1} (V_i^{k+1} - V_K) + g_L (V_i^{k+1} - V_L) \right] \quad , \quad (3.2.5)$$

where,  $g_{na}$ ,  $g_k$ ,  $g_l$  are the  $Na^+$ -channel,  $K^+$ -channel, and leakage channel conductivities, while  $m$ ,  $n$ ,  $h$  are non-linear, time-dependent gating functions. Also,  $ft = \pi \times diam \times dx$ . These gating functions are controlled using two rate control parameters each given by:

$$\alpha_m = \frac{2.5 - 0.1V^*}{e^{2.5 - 0.1V^*} - 1}; \beta_m = 4e^{-\left(\frac{V^*}{18}\right)}$$

$$\alpha_n = \frac{1 - 0.1V^*}{10(e^{1 - 0.1V^*} - 1)}; \beta_n = 0.125e^{-\left(\frac{V^*}{80}\right)} \quad (3.2.6)$$

$$\alpha_h = 0.07e^{-\left(\frac{V^*}{20}\right)}; \beta_h = \left(\frac{1}{e^{3 - 0.1V^*} - 1}\right)$$

In the set of terms described by equation (3.2.6), the subscript indicates the gating function name. So for example,  $\alpha_m$ ,  $\beta_m$  etc. are the rate control parameters for the gating functions  $m$ , and so on. This finally leads to the gating functions given by the following equations.

$$\dot{m}_i = \alpha_m(1 - m_i) - \beta_m m_i \quad , \quad (3.2.7)$$

$$\dot{n}_i = \alpha_n(1 - n_i) - \beta_n n_i \quad , \quad (3.2.8)$$

$$\text{and, } \dot{h}_i = \alpha_h(1 - h_i) - \beta_h h_i \quad . \quad (3.2.9)$$

Consequently, to update the  $m$ ,  $n$ ,  $h$  at each time step, the implicit scheme, which is the same as equation (3.2.3), is used and leads to:

$$m_i^{k+1} = m_i^k + \frac{\Delta t}{2} [\dot{m}_i^k + \dot{m}_i^{k+1}] \quad , \quad (3.2.10)$$

$$m_i^{k+1} = \frac{m_i^k + \frac{\Delta t}{2} [\alpha_{m,i}^k + \alpha_{m,i}^{k+1} - \alpha_{m,i}^k m_i^k - \beta_{m,i}^k m_i^k]}{1 + \frac{\Delta t}{2} [\alpha_{m,i}^{k+1} + \beta_{m,i}^{k+1}]} \quad . \quad (3.2.11)$$

### 3.2.2 Distributed Cable Model for Representing the Myelinated Nerve Segment

For the sake of completeness, it is also prudent to examine the modeling method for a myelinated nerve segment. This is also important because such nerves are present in the critical regions of mammalian species, allowing for a faster conduction velocity of the action potentials. This provides smaller response times when subjected to critical stimuli. One of the classic modeling schemes for the same was proposed by Frankenhaeuser and Huxley [FH model] [6]

and subsequently explored further to incorporate indirect stimulus by McNeal [59] This scheme builds upon the original set of equations for the unmyelinated case, by incorporating ionic concentration changes of  $\text{Na}^+$ ,  $\text{K}^+$  outside the nerve region as well. The model involves an additional ionic current component that is attributed to a “non-specific”  $\text{Na}^+$  channel. However, researchers such as Moore et al [71] and Fitzhugh [61] have used the original HH model with a slightly different treatment to account for the myelin sheath present in such nerves to achieve results comparable to the FH model. For the purpose of this dissertation, the modified HH model for myelinated nerves is used. To understand the differences in the modeling schema, consider figure 3.9. It shows the physical layout of a myelinated nerve segment along with its electrical equivalent network.

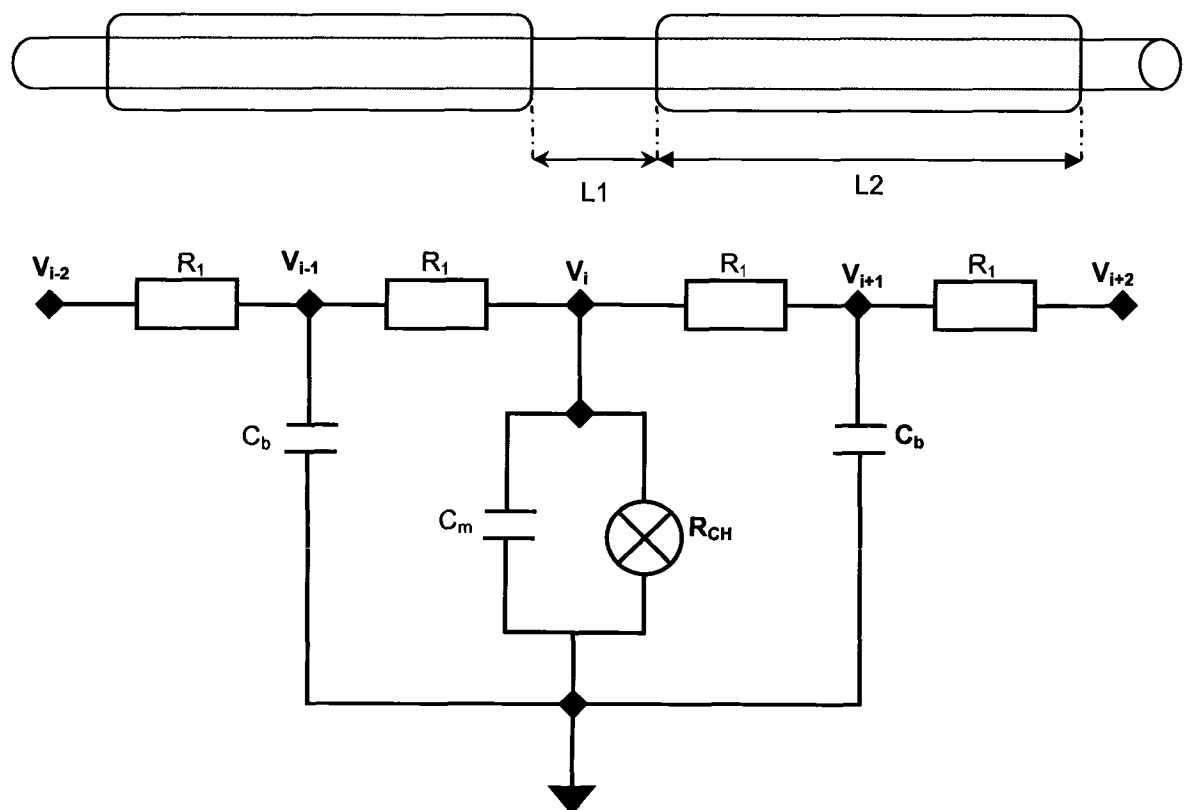


**Figure 3.9:** Physical structure of a Myelinated nerve segment. The Myelin sheath (shown in dark color) surrounds the axon length ( $L_2$ ) that lies between Nodes-of-Ranvier which have a length of  $L_1$ .

The figure above adopts the following convention. Nodes  $V_i, V_{i+2}, V_{i-2}$  refer to the “Nodes-of-Ranvier” that are unmyelinated regions. Nodes  $V_{i-1}$  and  $V_{i+1}$  refer to “virtual” nodes that exist at the mid-point of the myelinated sections. Also the compound ionic channels are represented as

$R_{CH}$ . The resulting equations are quite similar to those for the unmyelinated case, though with a few additions, and are presented here.

For the *virtual* node  $V_{i-1}$ , the equations at time steps  $k+1$  and  $k$  are given by:

$$\frac{V_{i-2}^{k+1} - V_{i-1}^{k+1}}{R_1} - \frac{V_{i-1}^{k+1} - V_i^{k+1}}{R_1} = C_b \dot{V}_{i-1}^{k+1} \quad , \quad (3.2.12)$$

$$\text{and, } \frac{V_{i-2}^k - V_{i-1}^k}{R_1} - \frac{V_{i-1}^k - V_i^k}{R_1} = C_b \dot{V}_{i-1}^k \quad . \quad (3.2.13)$$

For the node at Ranvier,  $V_i$ , these equations are:

$$\frac{V_{i-1}^{k+1} - V_i^{k+1}}{R_1} - \frac{V_i^{k+1} - V_{i+1}^{k+1}}{R_1} + I_{inj}^{k+1} = C_m \dot{V}_i^{k+1} + I_{ch}^{k+1} \quad , \quad (3.2.14)$$

$$\text{and, } \frac{V_{i-1}^k - V_i^k}{R_1} - \frac{V_i^k - V_{i+1}^k}{R_1} + I_{inj}^k = C_m \dot{V}_i^k + I_{ch}^k \quad . \quad (3.2.15)$$

The variables in equations (3.2.12) ~ (3.2.15) have the same meaning as those in the equations for the unmyelinated case. We can again use the implicit solution scheme given by equation (3.2.3), and make the following variable substitution for ease of writing:

$$Q_1 = \frac{\Delta t}{2R_1 C_m}; Q_2 = \frac{\Delta t}{2C_m}; Q_3 = \frac{\Delta t}{2R_1 C_b} \quad .$$

This yields for the *virtual* nodes:

$$V_{i-1}^{k+1} [1 + Q_3] - [V_{i-2}^{k+1} + V_i^{k+1}] \frac{Q_3}{2} = V_{i-1}^k + \frac{Q_3}{2} [V_{i-2}^k + V_i^k - 2V_{i-1}^k] \quad , \quad (3.2.16)$$

and for the Nodes of Ranvier points:

$$V_i^{k+1} [1 + 2Q_1] - [V_{i-1}^{k+1} + V_{i+1}^{k+1}] Q_1 = V_i^k + \dots$$

$$Q_2 \left[ \frac{V_{i-1}^k + V_{i+1}^k - 2V_i^k}{R_1} + I_{inj}^k + I_{inj}^{k+1} - I_{ch}^k - I_{ch}^{k+1} \right] \quad . \quad (3.2.17)$$

In all these equations, the channel current at all the applicable nodes is given by equation (3.2.5). Furthermore, the channel gating parameters and their rate equations are as defined in

equations (3.2.6)~(3.2.9). These parameters are updated using the equation set (3.2.10) ~ (3.2.11). It should be noted that equations for virtual nodes do not include injected current ( $I_{inj}$ ) or channel current ( $I_{ch}$ ) terms. This is due to the assumption made that the myelinated sections is significantly harder to excite. Consequently, any excitation that does occur will do so only at the “Nodes-of-Ranvier.” Furthermore, due to the well-known process of saltation, channel currents are negligible in the myelinated part [61]. Another key difference between the parameters of the myelinated and unmyelinated nerve segments is that the channel ionic conductance values for  $\text{Na}^+$ ,  $\text{K}^+$  and leakage are scaled in myelinated segments. Referred to as a high-density HH node, this is possibly due to a higher density of nerve fibers in the region of the “Nodes-of- Ranvier”.

Based on the set of equations in sections 3.2.1 and 3.2.2, the propagation of an action potential or multiple APs (neural traffic) can be simulated based on the nature and/frequency of excitation pulse ( $I_{inj}$ ). To highlight this consider figure 3.10, which shows the AP potential that is initiated using a  $0.2 \mu\text{A}$ ,  $0.2\text{ms}$  pulse. This is applied to a nerve discretized using  $0.1 \text{ cm}$  segments and having a diameter of  $23.8 \mu\text{m}$ . The excitation is applied at node 2 which is at one end.

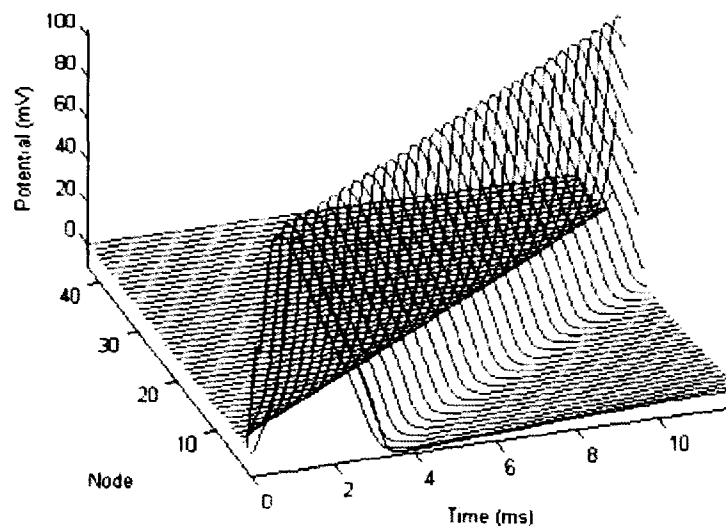


**Figure 3.10:** Action potential propagation in a  $23.8\mu\text{m}$  diameter nerve segment.

The temporal shift in the potential peak is clearly visible. Based on the time lag in successive peaks, we can also compute the action propagation velocity. The other key factor that figure 3.10 highlights is that an action potential is nothing but a sequential build-up of charge at consecutive nodes from the point of initiation. Alternatively, it constitutes a moving voltage wavefront. Consequently, the ONLY way of preventing successive nodes from being excited is to somehow draw out the charge as it builds up at a particular node. Almost all the methods that



have been proposed so far involve either injection of an “Interrupt Signal,” which could be a suitably polarized DC current [8] at a node downstream and/or AC current injection of suitable frequency [7]. In all these cases, the basic nerve model is not disturbed. Apart from problems such as permanent nerve damage due to heating (which is clearly undesirable) these methods also do not guarantee a robust block owing to their narrow frequency range. The fact that this frequency range is variable as a function of the nerve diameter does not help either. In the next section a new scheme is presented that allows for modulation of the trans-membrane conductivity, which in turn can facilitate the extraction of the charge required for AP propagation. The problems and disadvantages associated with the possible AC/DC block schemes have already been discussed in chapter 2.

### 3.2.2 Modified HH Model for Membrane Conductance Modulation

As shown earlier, the AP propagation mandates a sequential charge build up at successive nodes. It is also known that the external surface of the axon surrounded by some medium (body fluid, cerebral fluid, etc.) can be considered as grounded for all practical reasons. This leads to a possibility that if the stimulating charge propagating from a neighboring node can be shunted around the membrane capacitance, it will prevent the capacitance from charging. Consequently, the channel ionic gates would be prevented from switching from their default states. To test this scheme, a slightly modified electrical schematic is now presented. Only the unmyelinated equivalent circuit is shown, but it is applicable to the myelinated case as well, owing to the similarities between the two models.

Looking at figure 3.11, the pathway for channeling the charge is represented by a variable conductance  $G_{SH}$ . Before examining or discussing the possible ways by which this shunt conductance can be practically achieved, the modified equations are first presented. For the sake of brevity only the two key nodal equations are given.

The resulting nodal equation for  $V_i$  at time steps  $k, k+1$  are:

$$\frac{V_{i-1}^{k+1} - V_i^{k+1}}{R_a} - \frac{V_i^{k+1} - V_{i+1}^{k+1}}{R_a} + I_{inj}^{k+1} - I_{ch}^{k+1} = C_m \dot{V}_i^{k+1} + I_{sh}^{k+1} \quad , \quad (3.2.18)$$

$$\frac{V_{i-1}^k - V_i^k}{R_a} - \frac{V_i^k - V_{i+1}^k}{R_a} + I_{inj}^k - I_{ch}^k = C_m \dot{V}_i^k + I_{sh}^k \quad , \quad (3.2.19)$$

where,  $I_{sh}^k = V_i^k \cdot G_{sh}$ . Since the nodal equations for the “Nodes-of-Ranvier” in the myelinated model are quite similar to those in equation (3.2.1), equation (3.2.19) applies there as well.

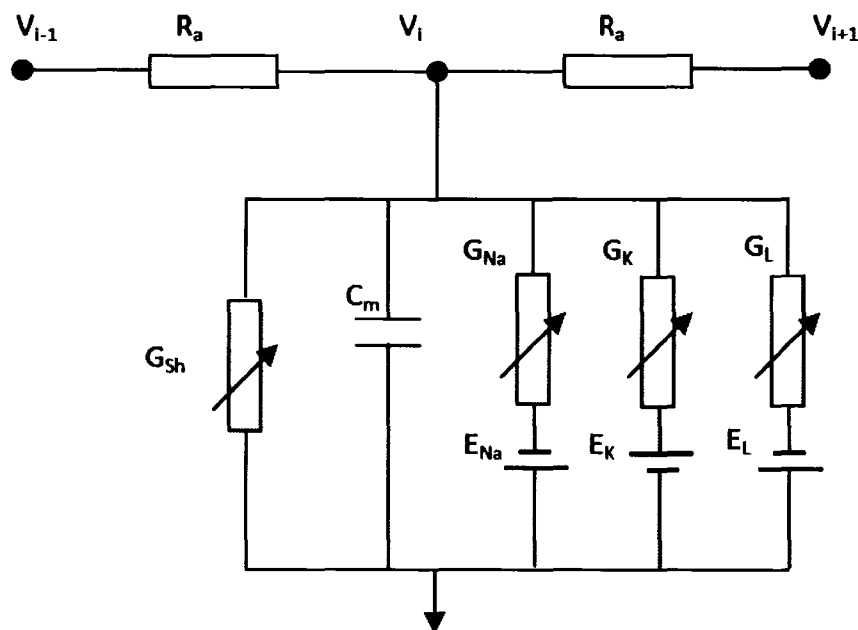
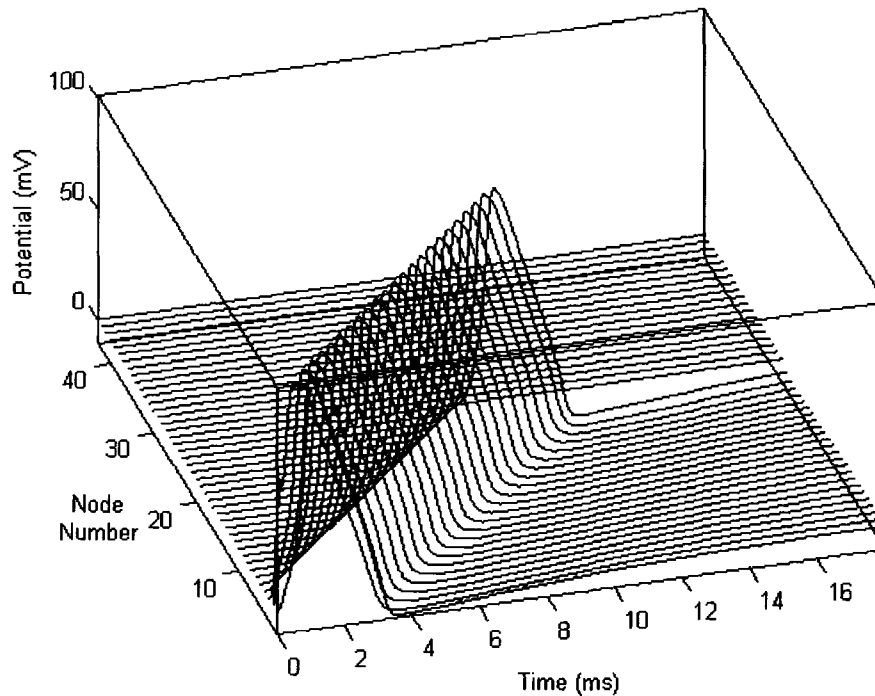


Fig. 3.11: Schematic for the modified cable model.

In the next chapter (the results section) the minimum shunt conductance required for a successful AP block as a function of number of nodes for a given axon diameter will be presented and discussed. Even though more detailed figures showing the AP block nuances will be presented in Chapter 4, a sample figure highlighting the AP block is shown in figure 3.12. In this figure, the AP initiated at node 2 was at node 28.

### 3.2.3 Membrane Electroporation Effects

The above set of equations(3.2.1)~(3.2.17) yield time-dependent voltages at each nerve node, and constitute the usual approach for the analyses of propagating action potentials. The application of a HISDEP leads to nanopore formation on the cylindrical membrane surface as sketched in figure 3.13. As a result, the traditional cable model needs to be modified to take account of the increased membrane conductance (the  $G_{sh}$  term of equations (3.2.18)~(3.2.19) ). These parameters characterizing the electrical response are, in general, dictated by the number of pores (conduction pathways) formed for a given voltage amplitude and pulse duration. Hence, the foremost task is the evaluation of the time- and voltage-dependent pore density.



**Figure 3.12.** Action potential propagation block a 23.8 $\mu\text{m}$  diameter nerve segment.

The dynamics of pore creation and destruction have been well characterized by continuum approaches based on the Smoluchowski equation [20, 28, 85, 92-94, 108-115]. Since a detailed analysis and/or development of these equations are beyond the scope of this dissertation, only a brief summary of the same is presented. Smoluchowski theory is given in terms of the pore density distribution function which is  $n(r,t)$  and given by:

$$S(r) = \frac{\delta n(r,t)}{\delta t} - \left[ \frac{D}{k_B T} \right] \left[ \frac{\delta \left\{ n(r,t) \frac{\delta E(r)}{\delta r} \right\}}{\delta r} \right] - D \left[ \frac{\delta^2 n(r,t)}{\delta t^2} \right] \quad , \quad (3.2.20)$$

where  $S(r)$  is the source (or pore formation) term,  $D$  is a pore diffusion constant,  $T$  is temperature in Kelvin, and  $k_B$  the Boltzmann constant. The process of diffusion represents a “random walk” of the pore radius in “r-space.”

The formation of pores is generally assumed to be a two-step process. All pores are initially created as hydrophobic/non-conducting at a rate  $S(r)$  per unit area of the membrane, during every time interval “ $dt$ ”. This rate is given by:

$$S(r) = \frac{v_c h}{k_B T} \left[ \frac{dE(r)}{dr} \right] e^{-E(r)/k_B T} dr, \quad (3.2.21)$$

where  $v_c$  is an attempt rate density [116],  $E(r)$  the energy for hydrophobic pores,  $T$  the operating temperature, and  $k_B$  the Boltzmann constant.

Membrane conductivity is modulated by pore formation and qualitatively depends on the number of pores, their effective radii, the energy barrier to flow produced by the ionic interactions between the pore and surrounding dielectric, and the spreading resistance. Treatments of pore conduction have been described in the literature [92, 112, 117].

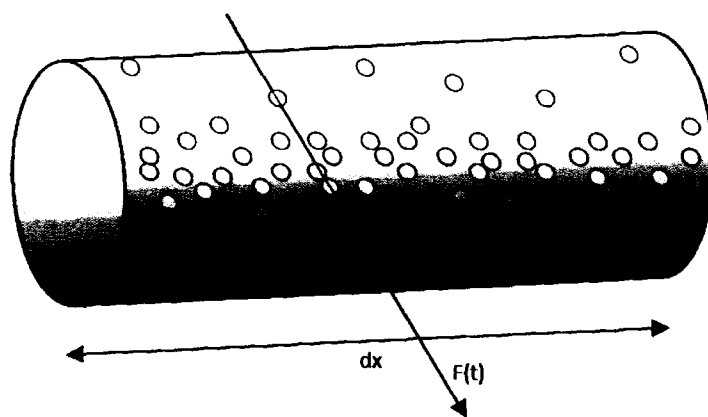


**Figure 3.13:** Sketch of pores created on the nerve membrane by the external voltage. A differential “ $dx$ ” of the nerve fiber is shown, and the external field is normal to the longitudinal axis.

While the treatment given below was originally discussed in the context of pulses longer than the nanosecond range, the basic physics of transport over a voltage-dependent barrier and pore-conductivity hold true regardless. As long as the transmembrane potential is suitably calculated and applied, the expressions given next remain valid. Following Glaser et al. [117] the pore conductivity  $G_{\text{pore}}$  was taken to be:

$$G_{sh}(t) = \pi R_o^2 H N(t) \left[ \frac{e^{U(t)} - 1}{U(t) \int_0^h e^{U(t) \left(1 - \frac{x}{h}\right) + \frac{W(x)}{k_B T}} dx} \right], \quad (3.2.22)$$

where  $U(t) = [V(t) \cdot q] / (k_B T)$ ,  $q$  being the electronic charge,  $H$  the conductivity of the aqueous solution,  $V(t)$  denoting the time-dependent trans-membrane potential,  $h$  the membrane

thickness,  $N(t)$  are the number of pores, and  $W(x)$  is the energy barrier for an ion inside the pore. The  $W(x)$  profile has a trapezoidal shape [117, 118] with a linearly varying regions of thickness  $d$  at the two ends of the pore, and a constant value of  $W_0$  over the central pore region.

Thus – the expression for  $W(x)$  profile is:

$$\begin{aligned} W(x) &= W_0; d < x < (h-d) \\ W(x) &= W_0 \frac{x}{d}; 0 < x < d \\ W(x) &= W_0 \frac{h-x}{d}; (h-d) < x < h \end{aligned} \quad . \quad (3.2.23)$$

Typically  $W_0$  is much larger than the thermal energy  $k_B T$ , and under these conditions, the pore conductivity simplifies to:

$$G_{sh}(t) = \frac{L_z \int_0^\pi d\theta \int_0^\infty n(r, \theta, t) r^2 H D dr}{[1 + P(t)] e^{\frac{W_0}{k_B T - \eta U(t)}} - P(t)} \quad , \quad (3.2.24)$$

where,  $P(t) = \frac{\eta U(t)}{\frac{W_0}{k_B T} - \eta U(t)}$ .  $\eta = d/h$  is a measure of the relative size of the pore,  $D$  is the

diameter of the nerve fiber and  $L_z$  is the inter-nodal segment length. In equation (3.2.24),  $n(r, \theta, t)$  is the pore density function as defined in equation (3.2.20). Since the number of pores is non-uniform with an angular dependence, the pore resistance needs to be evaluated across differential stripes of width  $R d\theta$  ( $R$  = nerve fiber radius) and longitudinal length  $L_z$  across the nerve membrane. The overall shunt conductivity  $G_{sh}$  is obtained by adding the spreading resistance at the pore entrance to the effective pore resistivity. Thus:  $G_{sh} = [1/G_{sh} + R_{sp}]^{-1}$  where the pore spreading resistance  $R_{sp} = \rho/2r$ , and is the resistivity of the aqueous medium. This latter characteristic is also referred to as the access resistance [119, 120].

This chapter detailed all the modeling methods and aspects thereof that this dissertation targets. In the next chapter, results from these schemes are presented along with relevant discussions and a few highlights of problems that were encountered in the development process. In the last chapter, a summary of this entire dissertation along with suggestions for future work in this area will be presented.

## Chapter IV

### Results and Discussion

#### 4.1 Distributed modeling scheme

In this section, simulation results from the full-body modeling implemented using the distributed computational scheme will be presented. Also highlighted will be the effects of process grid size, cluster load, and communication overhead. However, before any such data is presented, it is prudent to look at some of the available visualization methods for the raw *input data*. This will help in highlighting the tissue level variability as well as the concept of *slicing the dataset along different orientations*.

##### 4.1.1 Input data visualization methods.

As mentioned in chapter 3, the full-body modeling scheme operates on binary data files that (for the purpose of this research) were provided by the Air Force Research Laboratory (AFRL), Brooks Air Force Base, San Antonio, TX. These files are binary files containing a stream of voxels listed in a pre-defined scan sequence.

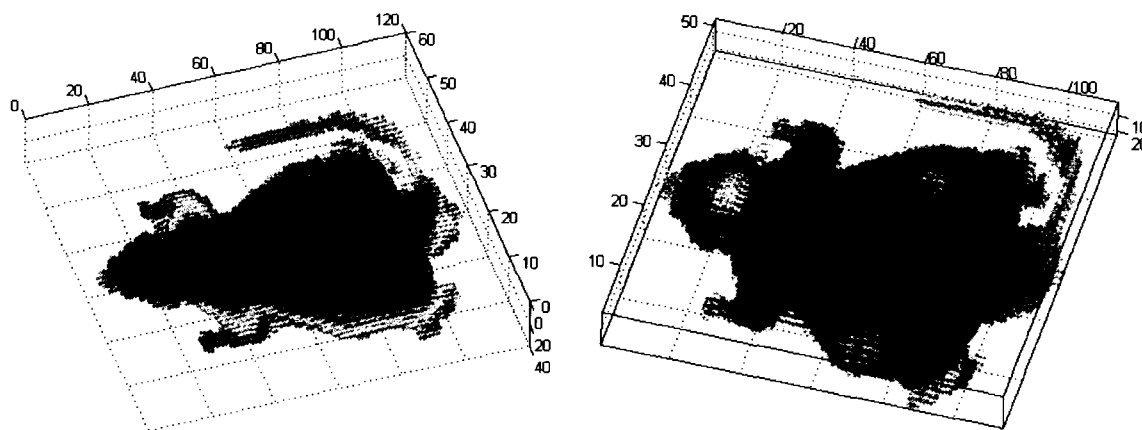


**Fig. 4.1:** Two forms of volumetric representation of the data.

The voxels are identified by their position in the file but represent a unique tissue identity number (ID). This ID is a 1-byte character that allows for representation of 255 tissue types. In figure 4.1 the rat model that will also be used for most of the validation tests is presented in the raw representation format. This model is comprised of 22 nodes along the depth (z), 51 nodes along the width (x) and 114 nodes along the length (y). The entire model was discretized using

1 mm spatial resolution. Even though there are  $\sim 23$  unique tissue types that are present in this model, they are not visible in figure 4.1 on the left, simply because the color-coding method used employs the vertical depth value. This means that all the voxels that lie at the same depth are represented by the same color code. If we use the tissue ID to color the data points, the tissue variation becomes more evident as shown on the right side of figure 4.1. Since this is a volumetric data representation, some of the tissue that lies on the *lower surface* is not very visible. However, to really impress the level of complexity that occurs in any real world bio-model, consider figure 4.2. It shows *slice-wise tissue layout* present at the depth of 15 mm.

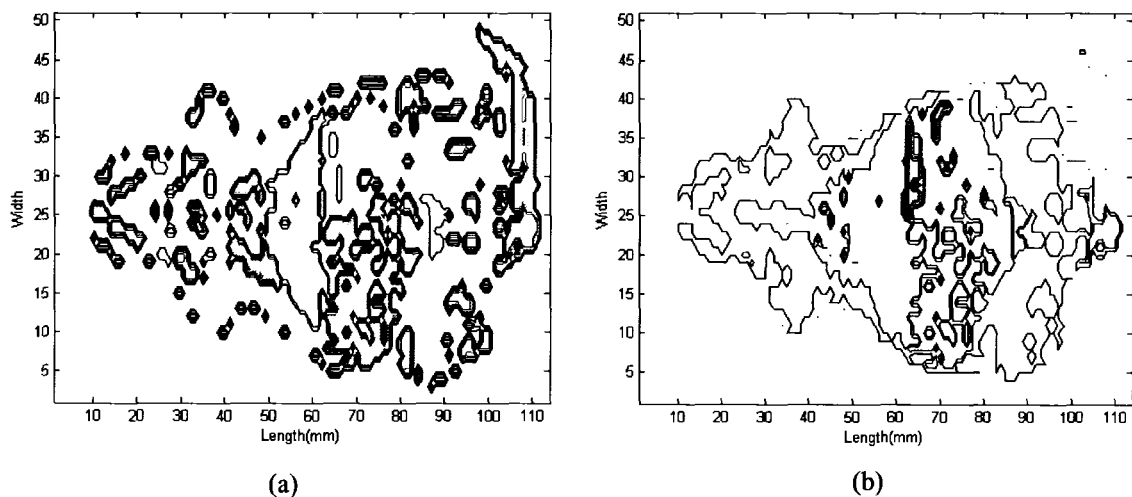


**Fig. 4.2:** Tissue layout present at a depth of 15mm. (a) tissue regions contoured using ID value.  
(b) tissue regions contoured using their conductivity values.

An important point made evident by figure 4.2(a) is that the conductivity values of different types of tissues are quite close to each other. This fact will become very important when the actual simulation results are presented. The other important point to note about slice-wise volumetric data visualization is the *orientation of the view*. Different orientations highlight information that tends to stay invisible in other dimensions. To highlight the importance of this, consider figure 4.3. This shows the tissue contours in the three different orientations. Each figure highlights the cranial matter; however, only figure 4.3(c) highlights the ocular region. Similarly, different orientations also bring out the intrinsic asymmetry present in the model. Even though each slice shown is taken along the central line for a given dimension, we notice that only the top portion of the right ear is made visible in figure 4.3-c. Similarly, 4.3a shows the asymmetry in the lateral cochlear regions. Furthermore, even though the depth spans 228 nodes, figure 4.3c shows the nasal region only up to  $\sim 215$ . A slice lower than the one shown

would highlight more of the nasal cavity and less of the ocular region. This visual difference becomes significant when visualizing the potential profiles in 3 dimensional form. Now that visualization and format of the input data have been presented, results from the parallel simulation scheme will be presented.

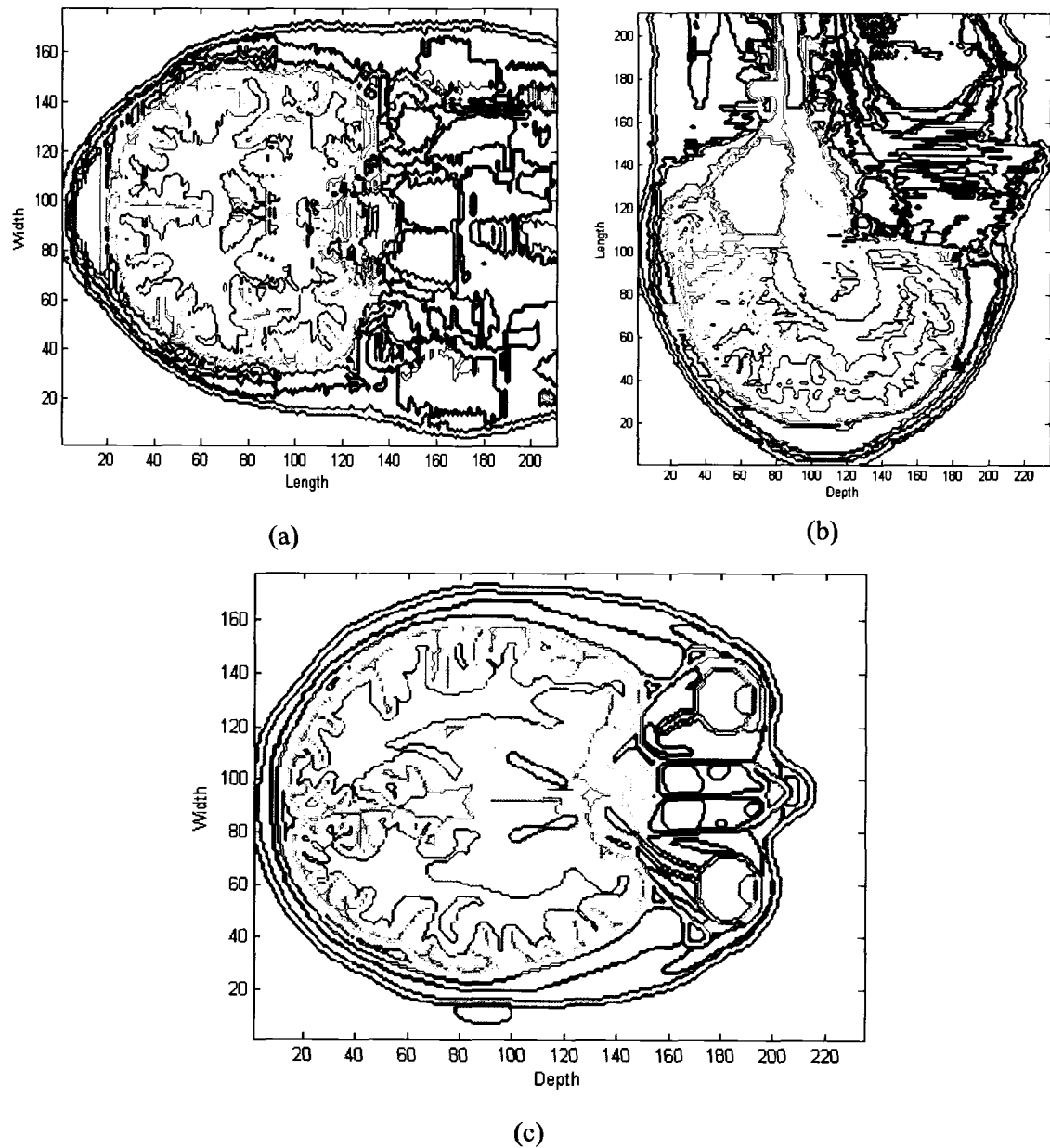


**Fig. 4.3:** Tissue layout in a human head as visible in three different orientations: (a) X-Y (b) Y-Z (c) X-Z

It should be noted that unless explicitly stated, all the results involving parallel computation were performed at Old Dominion University's Beowulf Cluster (Orville or Orion).



At no time was the cluster unloaded, and at no time were the compute nodes specifically reserved (this will become evident in the next section). The resulting data files were analyzed and visualized using MATLAB<sup>®</sup> 7.x on two separate IBM machines.

#### 4.1.2 Validating the full-body modeling scheme.

In order to gauge the numerical accuracy and actual validity of the proposed scheme **two** test cases are now presented. They are both implemented using a saline sphere but different electrode configurations. The saline sphere under consideration has a diameter of 21 mm (21 nodes at 1 mm each).

##### 4.1.2.1 Saline sphere with two parallel planar disc electrodes.

In this case, the cathode was assumed to be a planar disk passing through the center of the spherical tissue, with the anode being a smaller circular disk cutting the sphere parallel to the cathode. Thus, a two-dimensional projection of the geometry, as shown in Fig. 4.4a, resulted. In figure 4.4a, the cathode is represented by the diameter on the left, while the circular anode plate is the solid line on the right. The region in-between contains saline solution.

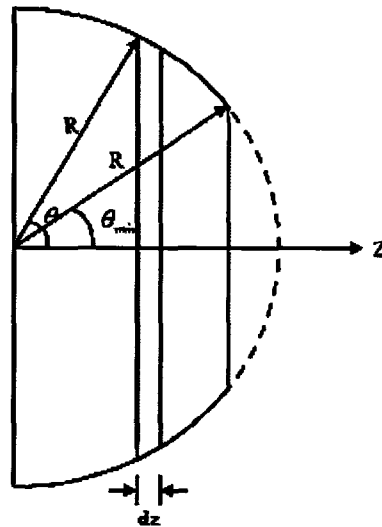


**Fig. 4.4a:** Two-Dimensional projection for the geometry used the in the first validation case.

The anode is parallel to the cathode and cuts the sphere in a circular disk. In spherical coordinates, the maximum angle between the peripheral anode point and the spherical center is  $\theta_{\min}$ . The radius of the sphere is denoted by  $R$ , the perpendicular distance between the two parallel electrodes is along the “z-axis”, and  $\theta$  is a general angle with  $\theta_{\min} < \theta < \pi/2$ . The effective resistance  $R_{\text{eff}}$  of the tissue between the two electrodes can be computed analytically.

Considering a differential slice of thickness “dz” as shown in Fig. 4.4a, the corresponding differential resistance  $dR_{eff}$  is:

$$dR_{eff} = \frac{dz}{\sigma \cdot Area} \quad (4.1)$$

where the area of the differential disk =  $\pi[R \sin(\theta)]^2$ . Also,  $z = R \cos(\theta)$ , from which  $dz = -R \sin(\theta) d\theta$ , and the total effective resistance  $R_{eff}$  becomes:

$$R_{eff} = \int_{-\pi/2}^{\theta_{min}} \frac{R \sin(\theta) d\theta}{\sigma \pi R^2 \sin^2(\theta)} \quad (4.2)$$

Carrying out the integration yields,

$$R_{eff} = \frac{\ln \left[ \tan \left( \frac{\theta_{min}}{2} \right) \right]}{\sigma \pi R} \quad (4.3)$$

Simulation result for the current response to a 1000 Volts trapezoidal pulse (0.5 ns rise and fall times and 10 ns ON time) is shown in Fig. 4.4b.

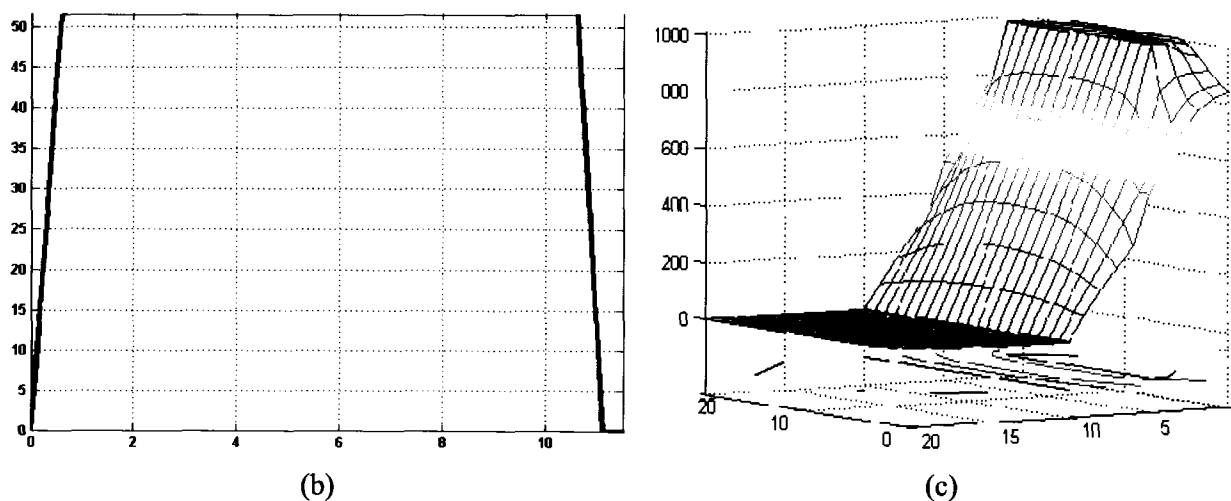


**Fig. 4.4b and 4.4c:** Current response and Potential profile to the first validation test case.

The predicted stabilized current during the pulse ON time was roughly 51.5 Amperes. The effective resistance from the numerical simulation works out to be:  $1000V/51.5A=19.42$  Ohms. The angle  $\theta$  in equation (4.3) is given by:  $\theta = \cos^{-1}(7/10) = 0.7954$  radians. Using this value in equation (4.3) yields  $R_{eff} \sim 20.7$  Ohms. This value is very close to the simulation result of 19.42 Ohms and roughly validates the numerical implementation in this case.

The voltage profiles for the above test simulation are presented in figure 4.4c. The maximum voltage at the anode is 1000 V and occurs over a flat region intersecting the sphere. The cathode is at zero volts and runs through the parallel diameter. Most of the voltage drop occurs between the two electrodes. Some electric field is also created near the smaller anode disk. In the next sub-sections, we present a more detailed analysis of this saline sphere that will also focus on current density and other variables.

#### 4.1.2.2 Saline sphere with symmetric axially located electrodes.

Figure 4.5a shows the saline sphere rendered using a solid patch method. Since this is a uniform sphere, the Cartesian cubic volume also contains surrounding air regions. The six faces where the sphere is in contact with the volume boundaries are shown in grey. For this simulation case, two such diametrical regions are used to set up the Anode and Cathode regions.

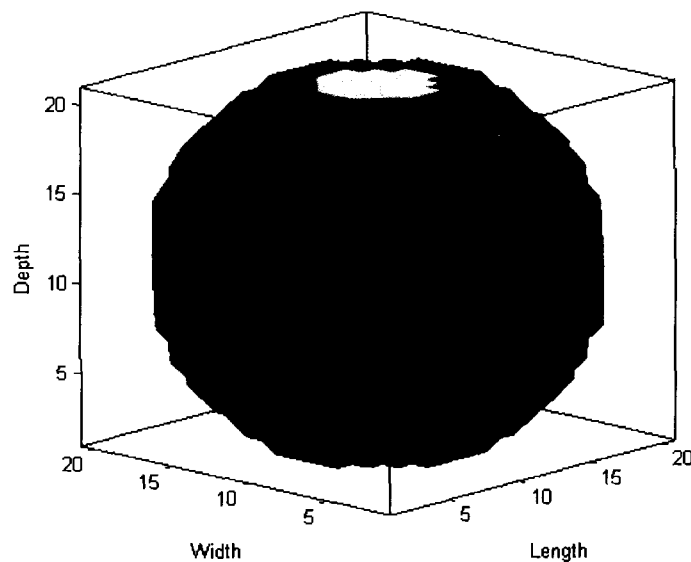


**Fig. 4.4a.** Solid rendered saline sphere. The Grey patches are the interface regions of the sphere with the simulation volume region (also shown).

The applied pulse was taken to be trapezoidal with a 1kV amplitude, 30 ns rise and fall times and 500ns ON time. The resulting potential profile taken mid way along the depth is shown in figure 4.5b. The net steady state current flowing between the electrodes computed across a slice spanning along the width and depth is shown in figure 4.5c. Comparing this with the first test case, the net current flow is significantly lower, which is also expected, as now the entire sphere is under consideration, and the net resistance offered will be higher.

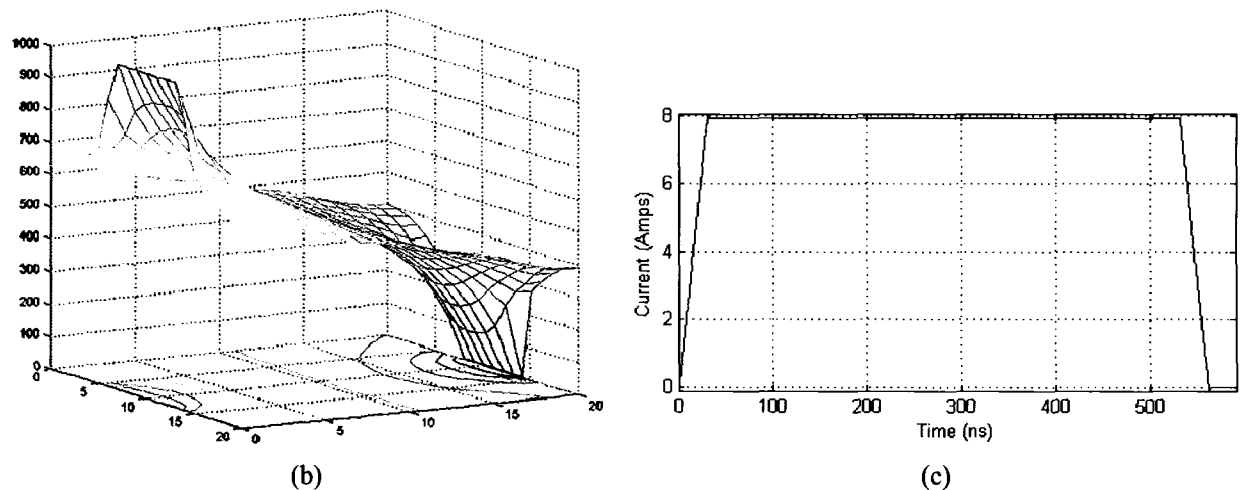


Fig. 4.5b and 4.5c. Potential profile and current response for the second validation case.

#### 4.1.2.3 Saline brick with an air pocket.

To further test the potential computation, we now present another simple geometry, that of a saline brick. It has dimensions of 10mm\*10mm\*10mm. An air slab is introduced between  $x=4\text{mm}$  and  $x=5\text{mm}$ . This slab is parallel to the Y-Z plane and the electrodes are simulated to be located on the two Y-Z faces at  $X=1$  and  $X=10$ . The setup is shown in figure 4.6a.

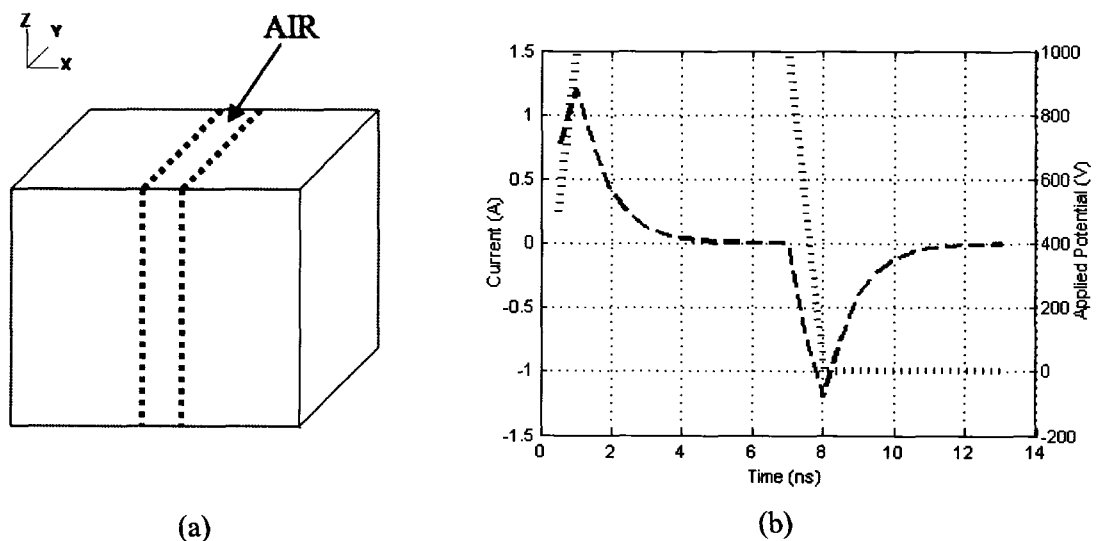


Fig. 4.6. (a) Saline brick with an embedded Air Slab, and (b) Applied potential and Current flowing through any slice parallel to the air slab.

This setup is then excited using a trapezoidal pulse with a 1ns rise time, 6 ns on time, 1ns fall time and the simulation continued to 5 ns post pulse duration. The applied pulse amplitude was

1000V and its waveform is shown in figure 4.6b (green dotted curve). Saline is listed to have an effective conductivity of 0.133 S/m. This indicates that the total resistance offered by this compound brick during the effective rise time and fall times of the pulse is  $\sim 752$  Ohms. Consequently, the peak current should be  $\sim 1000/752 = 1.32$ A. This compares very well with the value observed in figure 4.6b (the dashed curve). Since there is an air slab, the net current flow across the slab along the X direction must eventually fall to zero. The initial current peak rapidly (consisting of the displacement current) decays to zero. The air slab, which acts like a parallel plate capacitor, gets charged to the applied potential and the displacement current finally decays to zero. This operation gets repeated in a reverse order, as the pulse is removed starting from the fall time. The air slab discharges its stored energy and eventually the reverse direction displacement current also decays to zero. This current computation could also be done in different directions and the resulting current densities along different orientation can provide a good idea of body response to applied stimuli. This is highlighted in the next section, where we simulate the saline sphere using a different electrode configuration.

#### 4.1.3 Preliminary results highlighting current density computations.

In this particular setup the Anode and cathodes are rectangular plates that span the entire X-Y top and bottom surfaces. The two figures, 4.7a and 4.7b, show the potential profile for the central planes for central slices along two orientations.

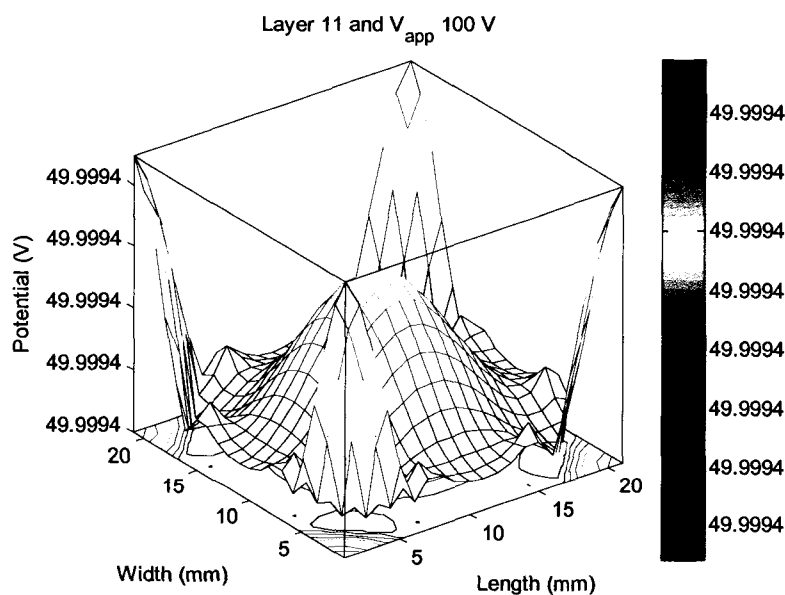


**Fig. 4.7a:** Potential profile for layer 11 in the X-Y orientation.

Since layer 11 is mid-way between the two electrodes and the saline sphere has uniform parameters everywhere, except for the air-regions (that have no conductivity), the potential is expected to be half of the applied value, i.e.,  $V_{app}/2$ . Given that the applied potential at the particular time instant is 100V, the mid-point value should be  $\sim 50V$ . This is borne out in Fig. 4.7b. An interesting feature of figure 4.7a is that it highlights the utility of visualization tools.

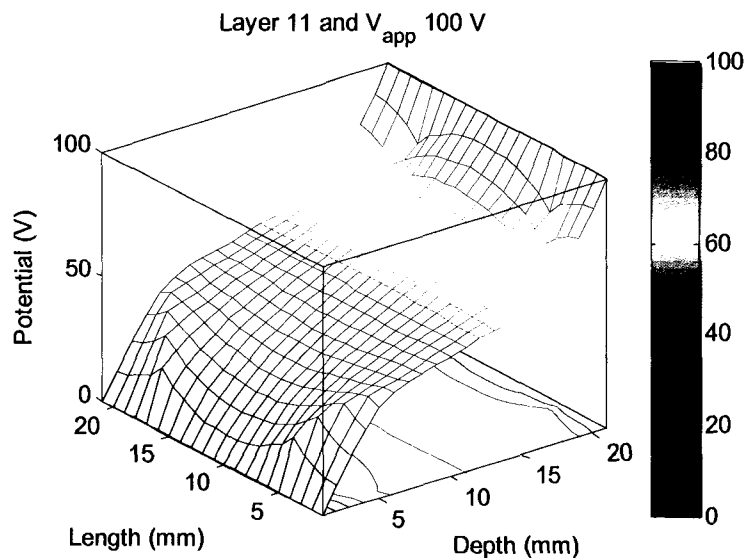


**Fig. 4.7b:** Potential profile for layer 11 in the Y-Z orientation.

In this particular case, the ripples and the “leaf” like structures in Fig. 4.7a are due to differences in values that are in the 5<sup>th</sup> decimal place or higher. Comparing this to figure 4.7b which highlights the profile at the central slice in the YZ orientation, we notice that the central portion (occupied by the saline), shows a linear drop from  $V_{App}$  to 0, while the air regions show the concentrated potential gradient at the edges. A color legend has also been included in figure 4.7b to reveal the potential values. Further analysis of these results involves computation of the current between the electrodes. More information can also be obtained by plotting the current density in each direction. Given that there are three primary orientations, to demarcate the different current density components, we use the following naming conventions. Irrespective of the orientation, *horizontal* refers to the X (Width) dimension, *Lateral* refers to the Y(length) dimension and *Vertical* refers to the Z (Depth). The computed current density for the central slice in each dimension is presented in figures 4.8. For the sake of symmetry and ease of visualization, we selected the central slice in each dimension.

Given that there are 9 plots here, it is prudent to discuss them briefly. The first row shows the current density for the slice that is parallel to the electrodes. Since this slice is normal to the actual current flow, the horizontal and lateral plots show the symmetrically minor density

distribution. The reason the horizontal and lateral components are so negligible is because in this particular setup the entire slice is an equi-potential. The vertical current density plot is the one indicative of the bulk current flow. Rows two and three of this figure show the current density for slices that are parallel to the current flow. Figure 1 in row two and figure 2 in row three have negligible values. Similarly, figures 2 in row two and 1 in row 3 are symmetrically equal. Despite this being extremely trivial, it should be noted that even though the peak current densities are as high as  $1000 \text{ A/m}^2$ , because the typical cell area is  $1 \text{ mm}^2$ , which translates to a peak of  $0.001 \text{ A/mm}^2$ .

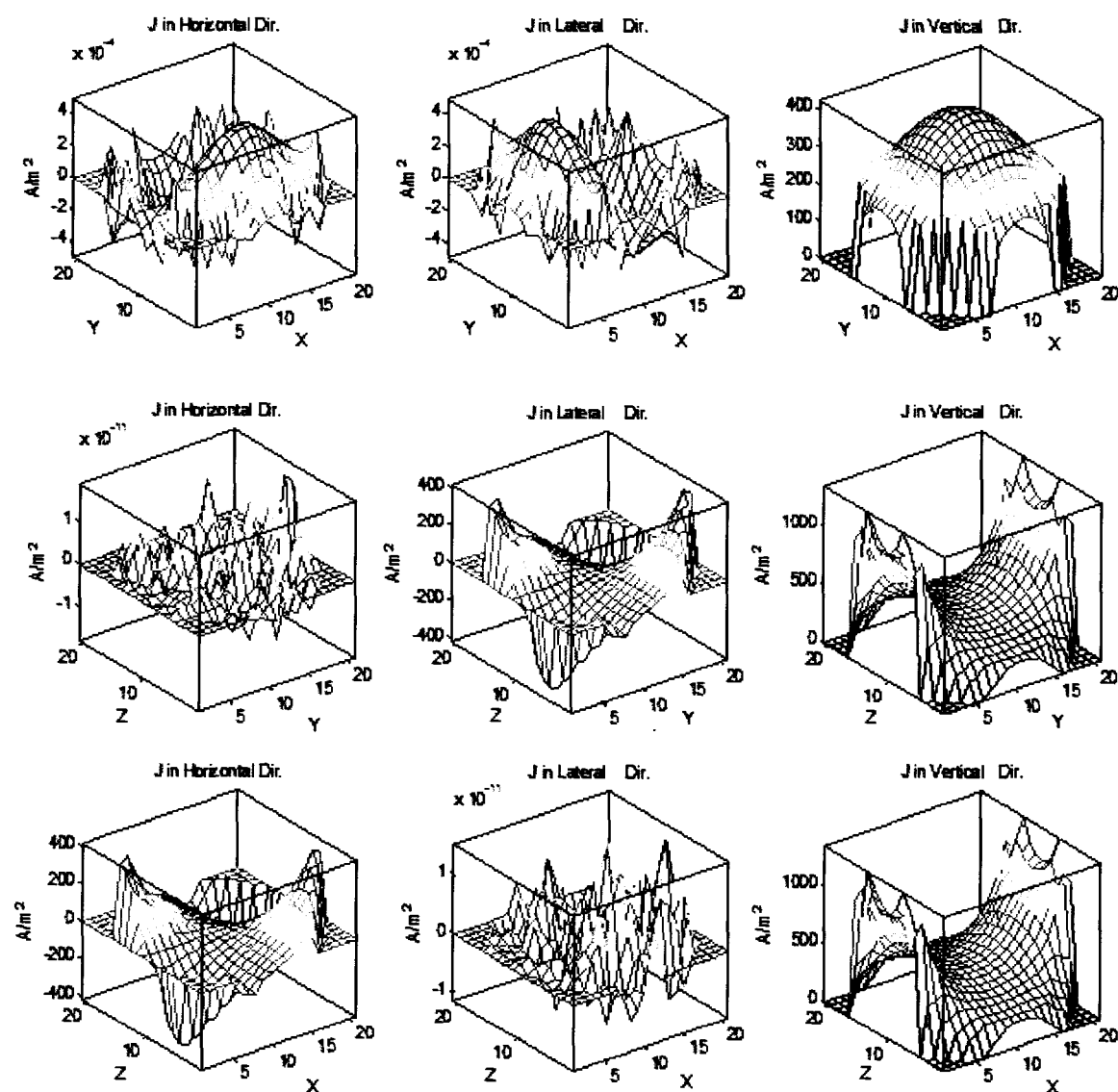


**Fig. 4.8:** Current density components occurring in central slice in each orientation. Each row represents slice 11 along a different orientation. Top row is for X-Y, followed by (Y-Z) and finally X-Z.

#### 4.1.4 Distributed process grid size and cluster load impact

Given a distributed computational setup, any simulation job that is submitted for parallel execution on a computing cluster is typically placed in a queue. The process/queue controller then holds the job there till the other jobs ahead of it have finished executing *and* the number of processors requested at the job submission time are available. If they are not, the current job is again put on hold (of course this may vary due to different cluster setup policies). In any event, the automatic assumption the notion that making more processors available for the execution of a computational job is always better in terms of the required “run-time”, is not necessarily correct. This is clarified through figures 4.9a and 4.9b.

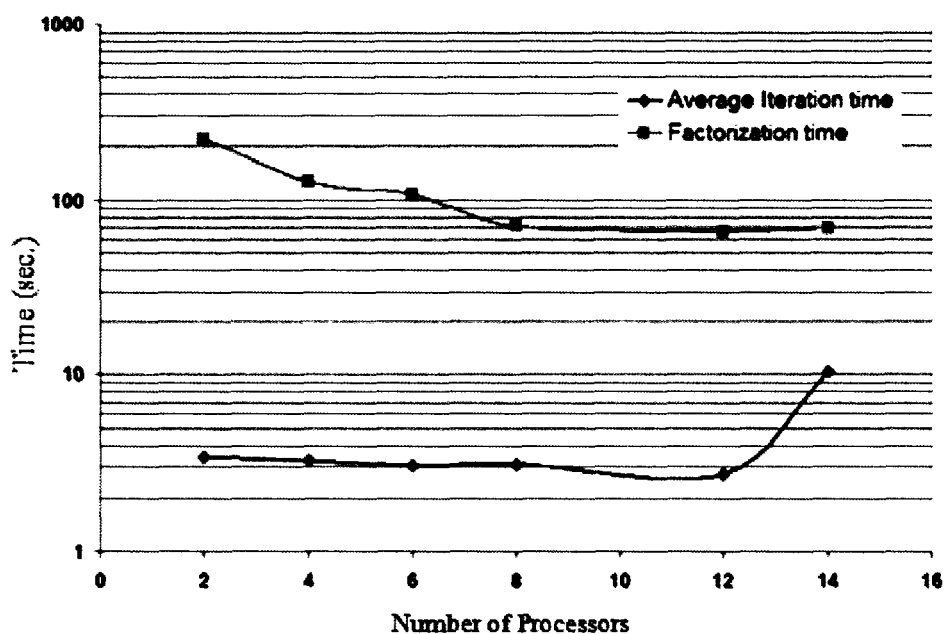


Fig. 4.9a. Timing diagram for the rat model for different process grid sizes during peak load hour

Figures 4.9a and 4.9b pertain to the rat model with 127908 nodes, which was setup up with a planar electrode configuration and solved for 503 time step potential pulse. As mentioned in chapter 3, the important step in this solution scheme is the setup of the coefficient matrix  $[M]$  and its subsequent factorization. Figure 4.9a shows that the most important change arising from variations in the number of processors occurs in the factorization time of  $[M]$ . We can also note that a process grid size greater than 8 in this particular case does not significantly decrease either of the two operation times. Now consider figure 4.9b.



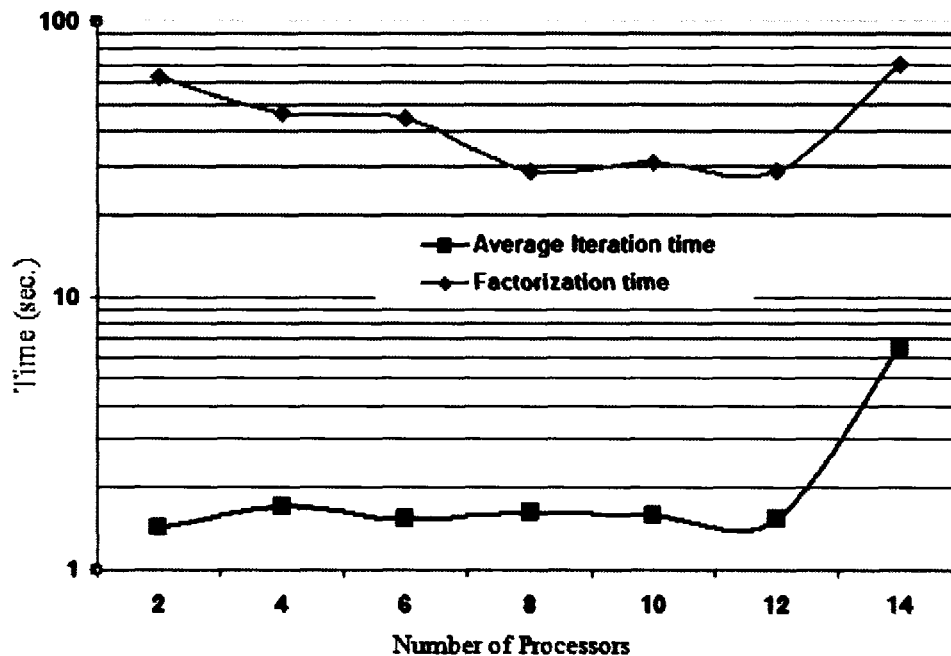


Fig. 4.9b: Timing diagram for the rat model for different process grid sizes during off peak hour.

This figure is for the same rat model, but the timing data was collected during off-peak hours. Immediately evident is that the overall times for both factorization and iteration are significantly lower during off-peak hours. This is to be expected. Also noteworthy is that even here the factorization time decreases fairly steadily up to the process grid size of 8. This then leads to the next important point about these figures. In both figures 4.9a and 4.9b, we notice a sudden jump in iteration times, especially after a process grid size of 12. This is due to the fact that for this particular problem size (and apparently, irrespective of the cluster load level), any more than 8 processors causes the *communication overhead* to become large. Thus the utilization of more processors for computations eventually exceeds the *computational benefit*. The communication overhead concept is related to requirement in that all distributed computation environments, the data sharing as well as synchronization uses some form of message passing protocol. However, the physical network interfaces have their own intrinsic latency. Depending upon the length (physical placement of the nodes with respect to the switch) and their bandwidth (10/100 Mb/sec, Gigabit or InfiniBand<sup>®</sup>), this latency can vary dramatically. Furthermore, if the number of slaves (i.e. processors other than the main in a process grid) is high, then the number of communications required to share the data and keep them in synchronization will also increase. Thus, after a particular process grid size, the physical hardware (especially the network end) starts straining the computation advantage in a job of a given size.

However, the caveat is that the optimal process grid size is not known *a priori* and typically needs to be determined heuristically. Of course, the assumption is that there are sufficient nodes actually available to allow for large variational testing. It should also be mentioned that factorization time also depends upon the number of non-zeros that appear as fill in. However, given the variability in the number of ways the setup and factorization can be implemented, the timing impact is not discussed here. Nevertheless, it is prudent to consider the impact of reordering the  $[M]$  to reduce the fill in. Even though the idea of these additional terms appearing during the factorization process has been discussed in section 3.1.2, the next section presents more details about the same and the reasons why exploring its reduction is worthwhile (especially for problems of “high” dimensions).

#### 4.1.5 Reducing fill-in during coefficient matrix factorization.

In section 3.1.2, the significance of sparsity was discussed. It was also explained that even though the original coefficient matrix may be extremely sparse, the factored form is almost always, extremely dense due to additional coefficients that arise (known as “fill in” phenomena [51]). Apart from the slightly less severe problems such as estimating the memory requirement for the “fill-in” caused, the biggest problem associated with “fill-in” is the requirement of significantly higher memory itself. In this section the differences that reordering can make are presented. Table 4.1 highlights two different cases.

Reordering is a process of re-arranging the columns and rows of a matrix so that the additional terms that appear during the factorization process are minimized. Even though the concept seems simple enough, several algorithms that stem from graph theory towards the optimal reordering scheme are fairly complex and beyond the scope of this research.

In any event, referring back to Table 4.1, a comparison of fill in for two different problem sizes is shown, i.e. dimension of the coefficient matrix. One is with 9261 nodes and the other with 127,908 nodes.

**Table 4.1** Comparative figures for fill-in with and without reordering

<b>Total nodes</b>	<b>Non Zeros</b>	<b>Density</b>	<b>NP</b>	<b>Reorder</b>	<b>Fill in</b>	<b>Fill-in density</b>	<b>Fill-in Factor</b>
9261	57939	0.000675546	2	Yes	1663534	0.019396167	28.87165812
9261	57939	0.000675546	2	No	1938705	0.022604555	33.62098069
127908	876390	5.35676E-05	2	Yes	68023862	0.004157822	77.76420315
127908	876390	5.35676E-05	2	No	91299694	0.00558051	104.3229635

In the table above, the column “non-zero” stands for the actual number of coefficients in the pre-factored coefficient matrix  $[M]$ . “Density” is nothing but a measure of the sparsity compared to a fully dense matrix of the same dimension. “NP” denotes the number of processors used. “Reorder” is a binary value that, if true, indicates that fill in reduction steps (reordering of  $[M]$  was performed prior to factorization). For reference, reordering of matrices has also been discussed in section 3.1.2. The “Fill-in” is the additional coefficients that were generated after the process of factorization. Anyway, this table shows a couple of very significant aspects of the full-body problem in general. First and foremost is that even though a problem size of 9261 nodes has a fill-in density of 0.00067, the number of fill-ins generated is ~29 times with reordering. Without reordering this rises to a factor of ~34. What this points to is that even though SuperLU\_DIST (the sparse solver that was introduced in chapter 3) has a default setting for maximum fill setting, it needs to be changed to a higher number based on the problem size and then recompiled. The advantage of reordering becomes more evident as the problem size grows. This also makes sense intuitively since problems with smaller dimensions will have a higher density. Consequently, the fill-in density will not be as different between the ordered and unordered cases. As mentioned in chapter 3, the reordering was done using a subroutine of a very well known open source package for multi-level graph partitioning. In all simulation results – the default control options were used. More information about these parameters can be obtained from the METIS manual (specifically METIS\_NODEND section) [121]. Furthermore, since the  $[M]$  setup and its reordering is done by the master only, the sequential version of METIS is employed. Having listed most of the peripheral aspects of the distributed algorithm, we are now in a position to actually present some real world simulation details. In order to ensure that a good range of problem complexity is presented, two (and space permitting three) different bio-models will be employed. These range from a saline sphere to a rat model and then onto a monkey head. These also provide a good range of problem *size* (ranging from 9261 nodes to 127908 to ~1.6 Million nodes).

#### 4.1.6 Simulation results for a complex multi-tissue whole body model.

Some of the preliminary results using uniform composition body models have already been presented earlier. The saline sphere and the brick models were used for validation as their uniform content allows for easy validation of a generalized scheme. The real target audience of this full-body modeling scheme is real world systems (animals or human models) where the tissue complexity is significant. In the next subsection, results are presented from two different complex bio-models.

#### 4.1.6.1 Rat model with cross-diagonally grounded paws

In this particular setup, the simulation was performed on the rat model. For a more realistic approach to the electrical excitation, two key modifications were incorporated. First, the applied pulse used was similar to that of an actual TASER<sup>®</sup> gun. The applied potential waveform is shown in figure 4.10. The other key difference was that very specific regions will be treated as anode and cathode nodes to simulate the miniature flat disk electrodes. In this setup, the base of the front right paw is connected to the anode. The base of the rear right paw is grounded. The semi-solid rendering of the rat bio model is shown in figure 4.11. This also provides a cross-diagonal electrical pathway and will lead to interesting deviations from the symmetric setup described in the previous section. To ensure that the clarity is maintained, there are 22 nodes along the depth (22 mm). Layer 1 implies the top surface (i.e. where the tips of the ears touch the simulation volume and 22 implies where the paws touch the simulation volume lower surface).

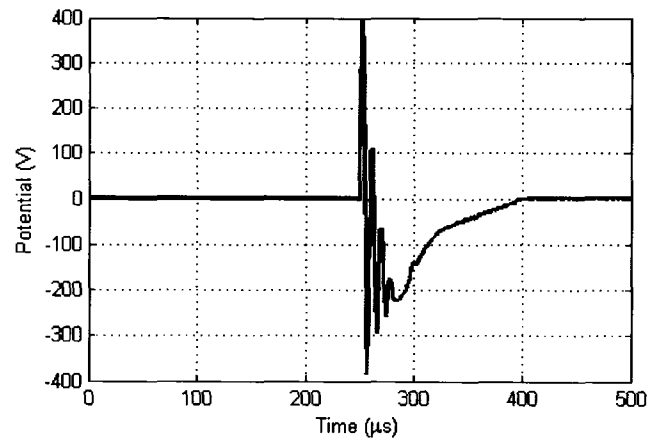


**Fig. 4.10:** Profile for the applied potential pulse for the rat model. This waveform is obtained by capturing the digital oscilloscope data stream, when connected to a TASER device.

A couple of points are worth mentioning with regards to the plot of the applied pulse. The real world data consisted of a lot of pre-pulse noise that has been smoothed out for the plot and simulation purposes.

In figure 4.11, air was used as the demarcating tissue type for generating the path-surface. Thus the stomach and the intestinal passage, which are usually associated with containing the largest air content, are visible inside the bio model.

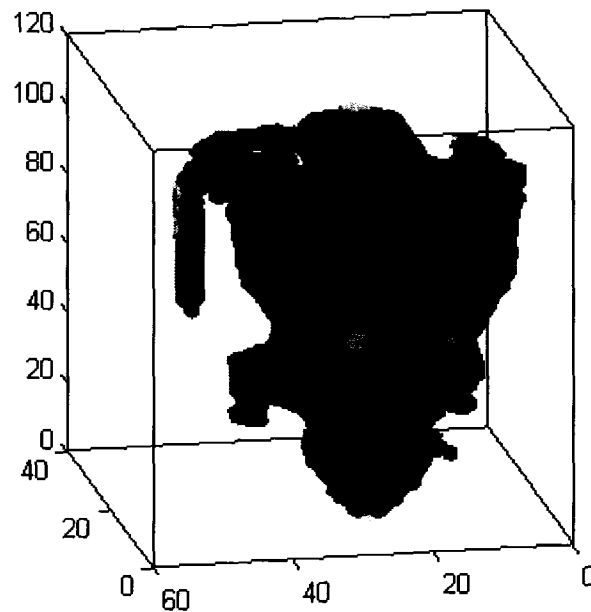


**Fig. 4.11:** Semi-transparent rendered rat model.

In figure 4.12, the resulting potential profile on two slices in the X-Y plane is shown. Since this is the most pertinent orientation given the electrode setup, we ignore the other two orientations. Figure 4.12, shows the resulting potential profile at 18mm and 5 mm depths (slice 18 and 5). It should be mentioned that the tissue boundary applicable to each slice is also overlaid on the potential contours in figure 4.12 for clarity. From figure 4.12a, the sharp potential gradient (dense contour lines) in the two limb sections is noticeable. This effect is quite pronounced given that this region is close to the electrodes and that the limb is the only conduction channel. In the main body section, the potential contours are far more spread out. In both cases, the snapshot has been taken when  $V_{APP}$  was 390.813V. Figure 4.12b shows the same for slice 5, which is much farther from the base. The two ears cross sectional regions are clearly visible. The dense potential contour in the ear region on the right side shows higher potential gradient owing to its proximity to the front limb that is connected to the anode.

It should also be noted that the tissue boundary is different from layer 18 due to the fact that the rat is not of uniform width or shape along any of its dimensions. Referring back to table 3.1 in chapter three, we notice that the conductivity for most of the tissue types is different. However the permittivity is quite similar. Therefore, even though the potential contours are fairly widely distributed in the main torso/abdomen region, the current density in each direction for a given slice brings out the difference in the conductive parameters. Given the fact that the permittivity values are almost the same, the displacement current density is not being shown here.

Figure 4.13 shows the conductive current density in  $A/m^2$  in the XY slice at 11 mm depth. Unlike the symmetric spherical case, since the electrical pathway from the anode to cathode has clear vertical, horizontal and lateral components, the current densities reflect these as well. The left column in figure 4.13 employs contours to highlight regions that have similar current density values (owing to similar tissue regions) while the right column is a standard 3-d surface plot. A negative current density means that the current flow is opposite to the direction assigned for the computation. As expected, the region of air that has negligible conductivity displays no current flow (density). Yet another significant result is visible from the vertical current density plot in figure 4.13. The three high current density regions (visible as circular regions) near the central part are coincidental with the spine placement. Given the fact that the spine curvature spans multiple regions along the depth, this shows that a part of the spinal region is under an unusually high electric stress. The significance of this result will become evident in the later sections when we discuss the hypothesis of high intensity electric pulses for the purposes of action potential block in nerve segments. We will also revisit this particular result when discussing an experimental result that will be used to support this hypothesis. For the sake of completeness, the total current flow across the central slices in each dimension is also shown in figure 4.14. In each subfigure of 4.14, the current magnitudes are in  $\mu A$ . Perhaps the most interesting result is that for the longitudinal current flow. It shows that the most of the current variation and flow is occurring not through the bulk but through the region near the edges. The proximity effect of the anode is also visible in the vertical current flow. It should also be mentioned that the visualization in figure 4.14 b and 4.14c are shown with angular rotation of 90 and 180 degrees, respectively.

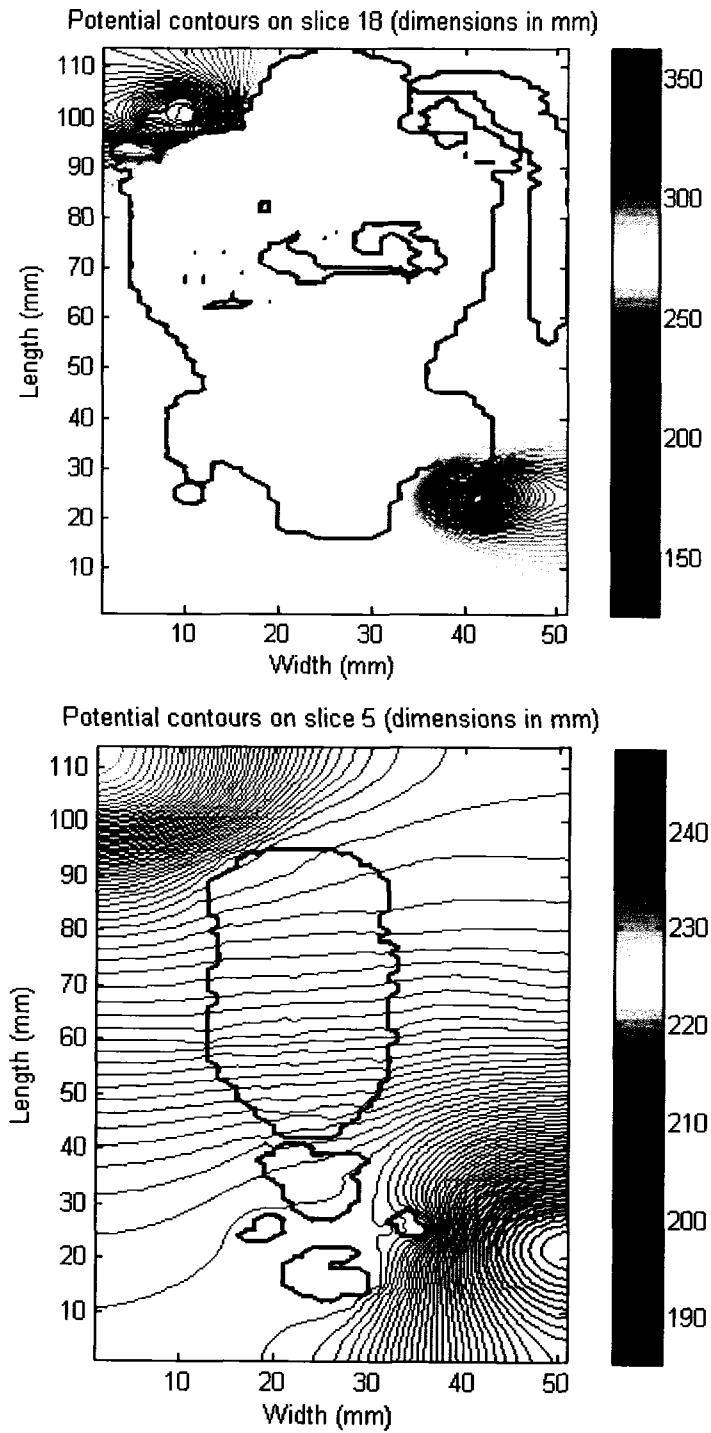


**Fig. 4.12:** Simulated potential profile at two slices in the XY plane (a) 18mm depth, and (b) 5 mm depth.

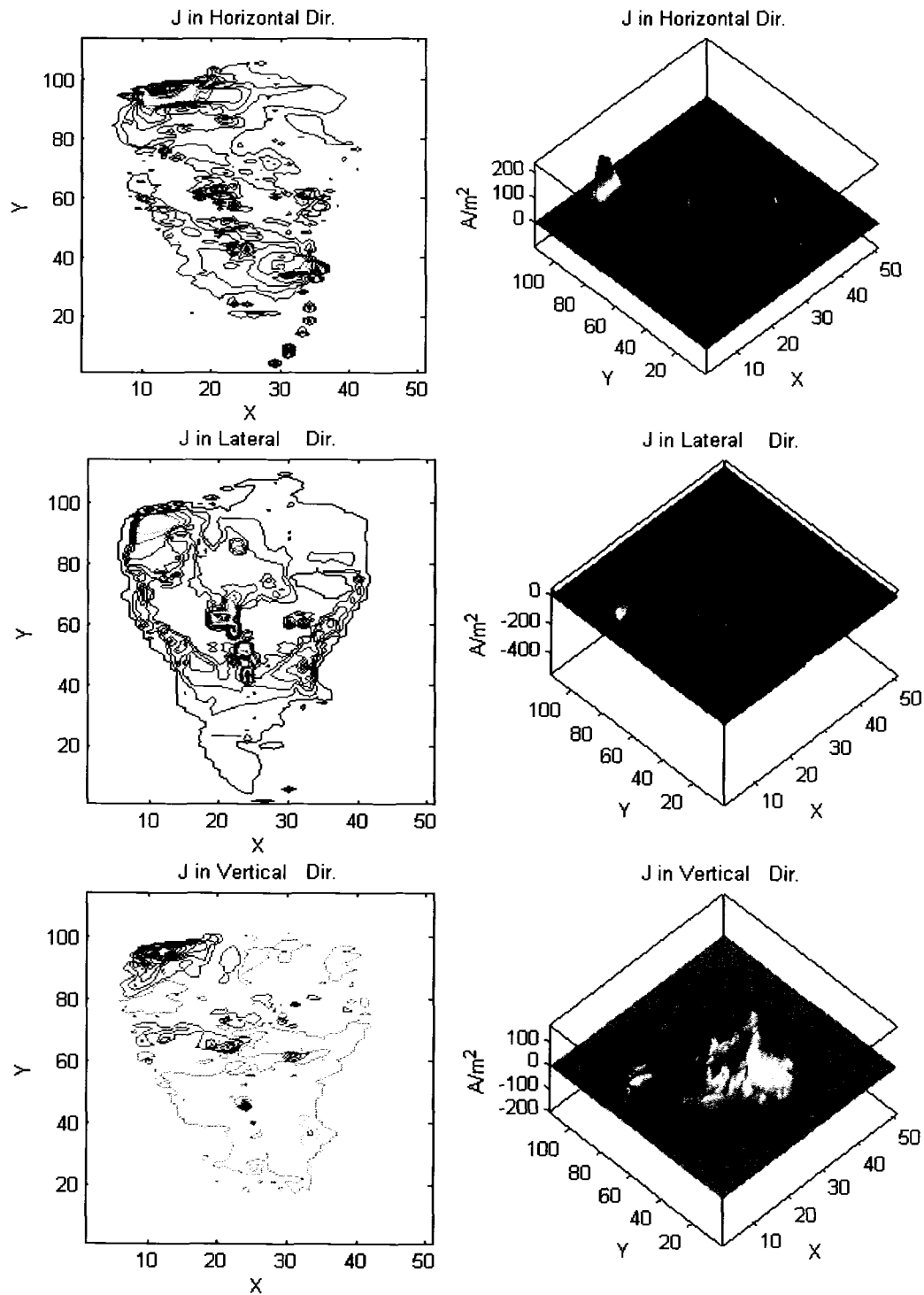


**Fig. 4.13:** Computed conduction current density in each direction for layer 11 in the XY plane of the rat model shown in figure 4.10.



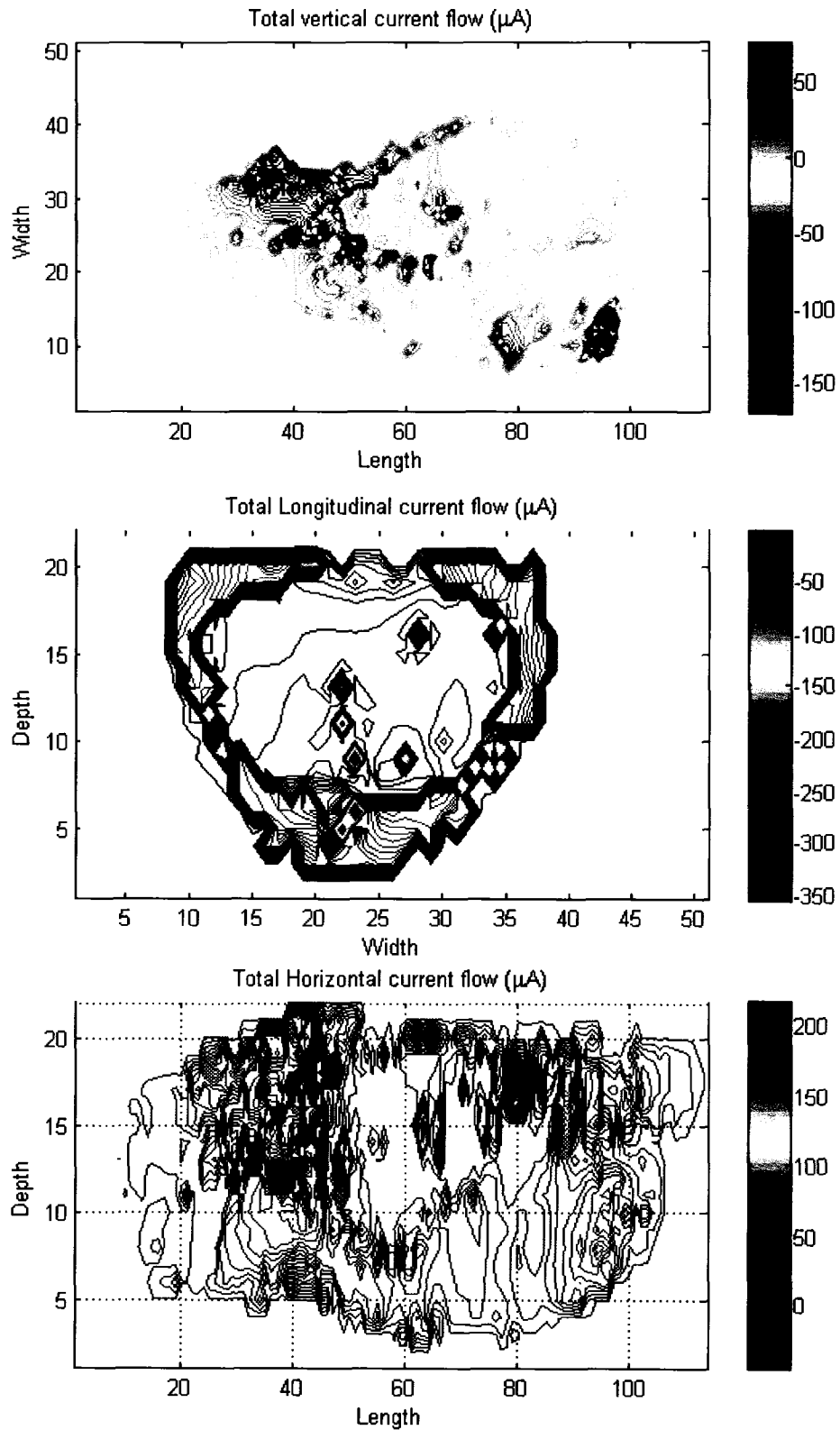


**Fig. 4.14:** Computed total conduction current in each direction across the central slice in each orientation.

#### 4.1.6.2 Monkey head with planar electrodes.

At the beginning of this chapter, it was mentioned that different tissue models tend to have extremely large dimensions. This can dramatically increase the number of grid nodes and the computational size. This underscores one of the advantages of distributed full-body modeling from a shared computational resources standpoint. The previous case discussed was for a rat model with 127,908 nodes. In this section, some results are presented for a monkey head that is comprised of 1,594,656 nodes. The simulated experimental setup is shown in figure 4.15.

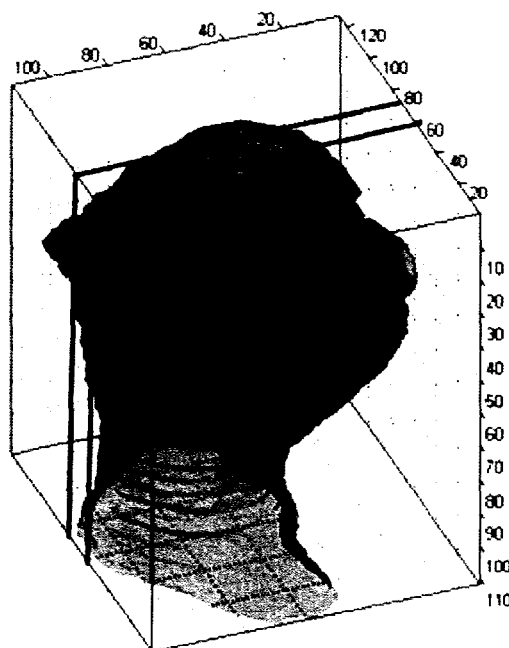


**Fig. 4.15:** A semi-transparent solid rendered plot showing the outer geometry in the monkey head model.

The two lines indicate Y-Z slices at  $x=65$  and  $75$  mm respectively. The Anode and Cathode were the planar surfaces (Y-Z) at  $X=1$  and  $X=126$ .

Figure 4.15 also shows two lines at  $X=60$  and  $X=75$ mm which indicate two different Y-Z slices along which the computed potential is presented. The applied pulse was identical to that shown in figure 4.10. The resulting potential profile is shown, using contours, in figure 4.16. In figure 4.16(a) the potential contours over the Y-Z slice at  $x=65$ mm are shown, while figure 4.16(b) shows them for the  $X=75$  layer. A localized enhancement of the electric field (closer spaced potential contours) at the base of the neck near the spine is evident. This can potentially have implications for the electrical stimulation of nerves at the spine, leading to “pain control” and/or temporary incapacitation. From both of these figures, it immediately becomes apparent that the

potential profile accurately mimics the physical tissue boundaries. The surrounding air regions are shown in cooler shades. Since the snapshot was taken during the negative swing of the applied potential, the cooler shades actually represent values closer to the positive level. Moreover, even though the total nodes increased by a factor of  $\sim 12$ , the computation duration per time step increased only by a factor of  $\sim 3$ . This highlights the other significant advantage of this distributed full-body modeling scheme.

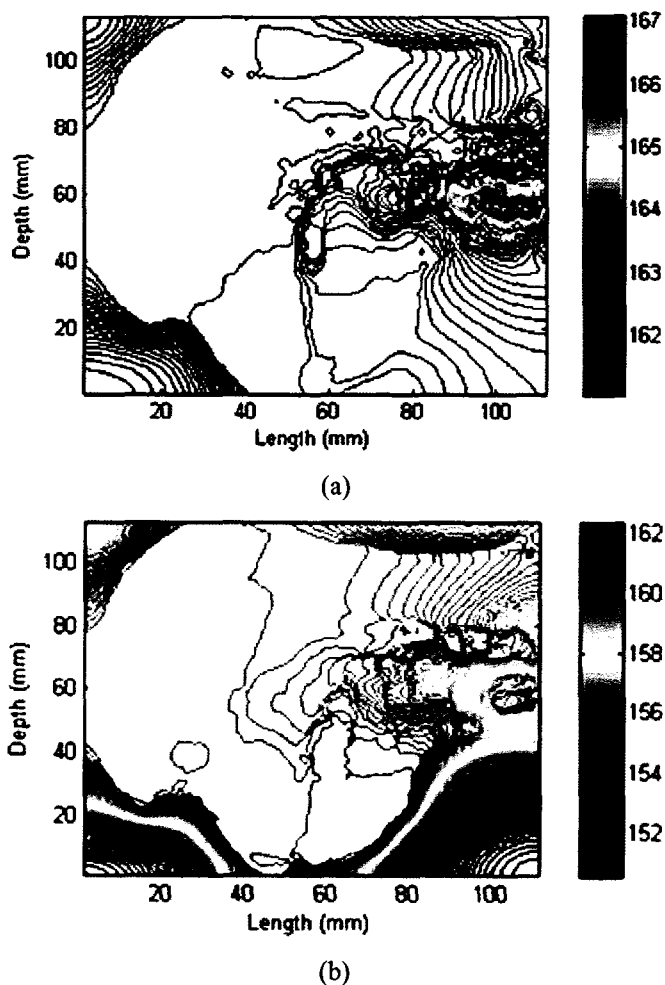


**Fig. 4.16:** (a) Potential Contours at  $X=65$  mm. The applied potential was  $-236$  VV. (b) The potential contours for  $X=75$  mm.

At this juncture, it should be mentioned that, using the modeling scheme of section 3.1, the time and memory required for the solution of this 1,594,656 node model defined the upper limit of our simulation capability based on the available computational resources. We now present some results for a 6.7 million node, *larger rat model* that was made possible by a

modification to the modeling scheme. Essentially, the matrix representing the underlying equations was converted from an asymmetric form to a symmetric one. This modification involved in converting the asymmetric coefficient matrix  $[M]$  to a symmetric matrix  $[N]$  will be discussed briefly. This will be followed by a comparison of the timing improvements between the asymmetric and the symmetric versions. The mathematical changes that allow this change are presented in appendix A.2.

#### 4.1.6.3 Significantly larger rat model.

In section 4.1.6.1, the rat model simulated had only 127,908 nodes. Though, not a small problem size by any means, it certainly does not compare with a typical real world model size. This “small problem size” was due to the relatively course grid spacing. The next monkey head with 1,594,656 nodes is certainly larger and presents a better test of the computational scheme. However, in terms of size, another rat model with a much finer spatial resolution was also available. This “larger rat model” had 6,639,732 nodes. It was used to test the simulation algorithm and its computational speed. For the purpose of simulation, the anode was a pin located at  $X=131$ ,  $Y=117$  and between  $Z=1-20$  mm. The cathode was a planar surface spanning the entire  $X$ - $Y$  surface at  $Z=105$  mm. This was done to ensure that there were at least some points where the rat paws were actually grounded. This was an issue, given that this particular model contained air between  $Z=106$  and  $Z=108$  mm. The two slices shown are  $X$ - $Y$  sections taken at  $Z=100$  and  $Z=75$  mm.

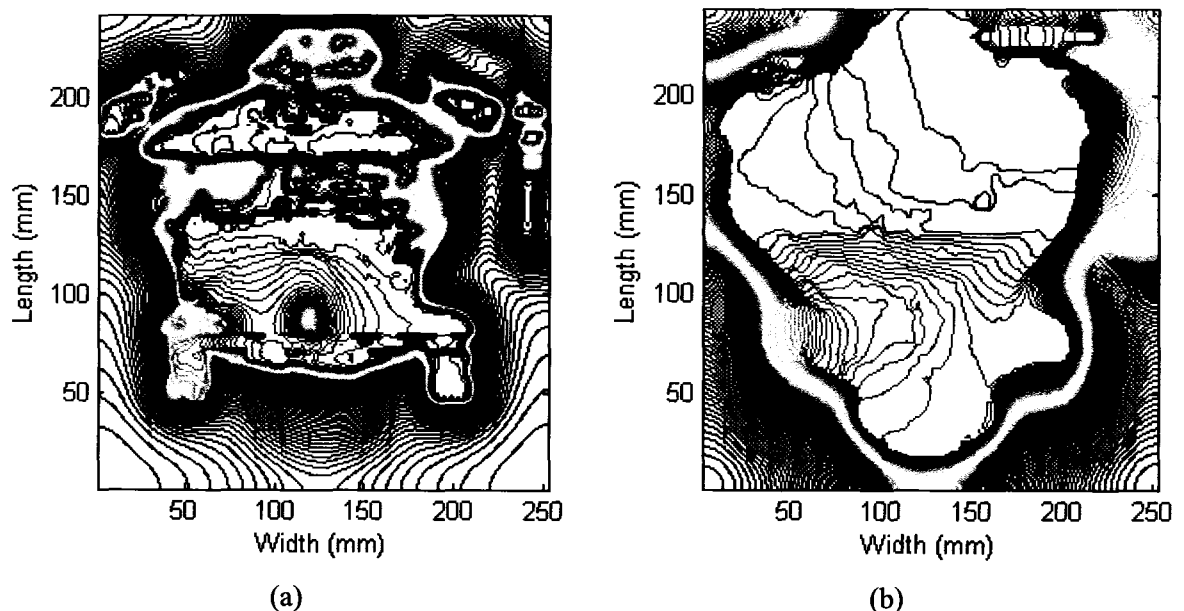


**Fig. 4.17: (a)** Potential Contours at  $Z=100$  mm. The applied potential was  $-236V$ . **(b)** The potential contours for  $Z=75$  mm.

#### 4.1.7 Comparing the symmetric and asymmetric modeling schemes.

Since positive definite symmetric matrices can be factorized using the Cholesky factorization [51], to perform this and the subsequent “forward-and-backward” solve operations. These “forward-and-backward” solve operations were performed for the asymmetric case previously discussed, as well. Here, we used the MULTifrontal Massively Parallel sparse direct Solver (MUMPS) [122]. Our decision to employ MUMPS to perform the symmetric computation was driven by two primary reasons: (a) MUMPS is written completely in FORTRAN 90 which allows for easier integration without developing our own F90 routines. This eliminates the problems usually associated with subroutine name mangling at the “compile and link” times. (b) The package has been designed to perform most of the requisite tasks (such as selection of reordering method, scaling scheme) automatically. It also features adaptive process grid load balancing depending upon real time statistics as obtained during the analysis phase performed prior to the factorization phase. In figure 4.18, we present the timing diagram for the 127,908 rat model as well as that for the 1,594,656 node monkey head model.

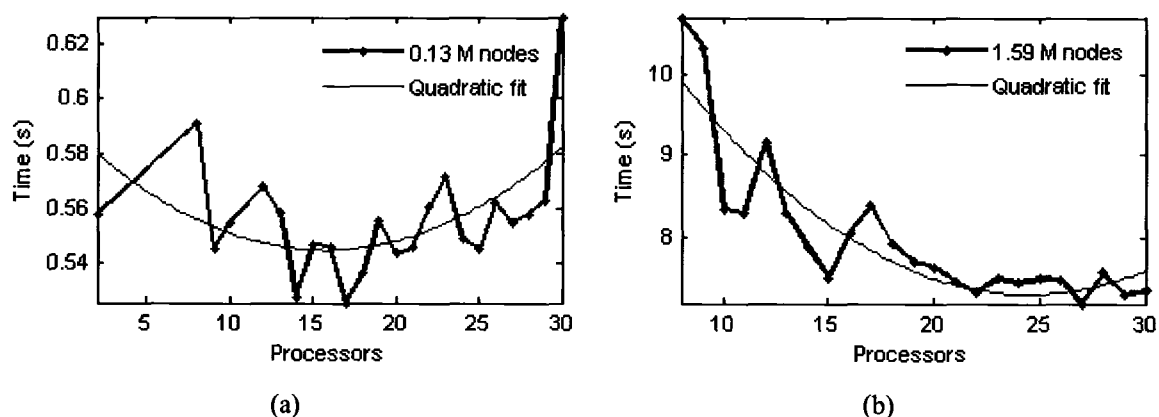


**Fig. 4.18:** Average computation time per time iteration for (a) 127908 node model (b) 1594656 node model.

Overlaid in each panel of figure 4.18 is a quadratic best-fit curve. If we compare figure 4.18(a) with 4.9(b) (which is for the same rat configuration but using an asymmetric solution scheme), the first thing we notice is that the solve time per iteration is lower with the symmetric scheme. If we look at the solve time required using 12 processors for the asymmetric case, it is roughly 1.8 sec. Comparing that with figure 4.18(a), the required solve time was ~0.56 seconds. This is almost a 3X speed-up in the computation. The next point to note is that in any distributed computation, if the number of processors allocated for a problem exceeds an optimal number, the communication overhead starts becoming significant. This slows down the overall process. Even though the variation in timing shown in figure 4.18(a) is quite small, a clear trend

exists can be seen in the figure. A quadratic data fit line was used and it was superimposed on the figure. It shows the trend in timing vis-à-vis, the processor grid. Figure 4.18(a) also shows that the optimal size for this problem size using the symmetric solution is 16 processors compared to 12 for the asymmetric case. In order to see a more distinct and rapid decline in the solve time with increase in number of processors, a larger problem set, as shown in Figure 4.18(b) is needed. Given the memory requirement, we could not run this model using less than 8 processors. A similar trend in timing drop and then an upward swing was observed, though not shown here. However, in this case the timing drop was more pronounced than the rise (if we continue to use the trend line). As mentioned earlier, one of the most critical physical resources that limit the overall size of the problem is the physical memory. The primary reason why we were able to push the limit on simulation size using the symmetric solution scheme, was due to the fact that only *one half of* the coefficient matrix needs to be stored. Furthermore, only one (*either* the upper *or* the lower) triangular matrix resulting from the factorization needed to be computed and/or stored. Furthermore, since the order of the symmetric coefficient matrix  $[N]$  is less than the order of the asymmetric coefficient matrix  $[M]$ , which leads to even more memory savings. For the sake of completeness, we now present some computational, run-time statistics reported for the symmetric solution scheme. Table 4.2 shows these details for the three main bio-models that have been presented and discussed in this dissertation.

**Table 4.2** Computational statistics for the symmetric solution scheme

<b>NODES →</b>	<b>127908</b>	<b>1594656</b>	<b>6639732</b>
<b>Non-zero entries</b>	456006	6236820	26136862
<b>Factor entries</b>	24882906	1276769145	8774111213
<b>Fill-in ratio</b>	194	204.7	335.6
<b>Factorization time (s)</b>	5.3055	845	9514
<b>Total OOC memory required (MB)</b>	261	34700	147874
<b>Av. time/Iteration (s)</b>	0.55	8	30

If we look at the average time per iteration, there is an almost linear relationship between the number of nodes and the average iteration time. This is expected given that the number of “forward and backward floating operations” post factorization, do not change, irrespective of the solution scheme. Also notable are the fill-in factors. Even though the fill-in factor for the 127,908-node model is 194, since we only need to store half of the factors, the storage overhead is only 96 times. Comparing this to Table 4.1, we see that it is slightly more

than when reordering is used. This slight increase is most probably due to the difference in ordering schemes (METIS versus the default option used in MUMPS). Finally, the transition from the 127,908-node model to the 6,639,732-node model represents an increase by a factor of  $\sim 52$ . A comparison between the average time per iteration for these two models yields a ratio of roughly  $30/0.55 = 54.5$ . Thus, the computational problem seems to scale with the number, "N", of nodes. This is a significant advantage and of a practical utility.

## 4.2 Nerve segment modeling and action potential (AP) block.

So far, the full-body modeling aspects were presented that included data visualization along with simulation results of bio-responses to stimuli from different electrode shapes and placements. However, once such spatial potential are computed, the real goal is to study the behavior of underlying nerves, which are embedded within these large contiguous tissue sections. These are eventually the primary pathways for electrical signals that elicit responses from the organs and/or limbs and muscles. The potentials and voltages at the various locations within the biological full-body will act as the driving forces for bringing about change in the neural signaling. It is hypothesized here that the localized electrical potentials created by the external pulsing could work to modify or even block the propagation of action potentials (i.e. neural traffic) through nerves.

Towards this end, the remainder of this chapter will present the salient aspects from the nerve modeling and signal conduction block schemes. To avoid redundancy, whether addressing unmyelinated or myelinated nerve segments, the nerve schema will not be presented. The following assumptions will hold for all cases:

- Node implies discretized point (unmyelinated case) or the Nodes of Ranvier (myelinated case);
- All diameters refer to the core axonal diameter;
- Unless explicitly mentioned otherwise, all potential values will be in mV;
- All segments simulated are terminated by resistive connections (equaling segmented axonal resistance) to the ground.

### 4.2.1 Visualizing the action potential.

Since the basic premise of this part of this research targets the action potential (AP) and its propagation and blockage, it is only prudent that the common forms of AP visualization be presented at the onset. Figure 4.19 shows three forms of representing AP in a nerve segment  $23.8\mu\text{m}$  in radius. The segment consists of 23 nodes with a  $0.5\mu\text{A}$  excitation being applied to node 11 (the central node) for initiation of the AP. Figure 4.19a shows a 3-d view of the effective trans-membrane potential, which is the more conventional form of representing the AP. The symmetrical bi-directional propagation of the AP (as expected) is also visible. Figure 4.19b shows the same 3-d view in color format as seen from the top. This is the most common representation that shall be employed in the subsequent sections. The color component of this figure also highlights the refractory period. This will also be better for highlighting conduction blocks and AP self-launch possibilities. Figure 4.19c shows the standard two-dimensional plots



for the membrane potential at three salient nodes downstream from the excitation point. The nodes are plotted as 13 (N13), 14 (N14) and 15 (N15). The temporal shift is clearest in this particular figure. It also allows for the computation of propagation velocity of the AP by using the peak timing at different nodes and the inter-nodal distances. Velocity computation is not particularly important for the end AP block method that will be explored. However, it does play a significant role when addressing the problems with some of the proposed AP block methods involving AC current injection. Figure 4.19d shows the change in the ionic channel gating functions over the simulation period. Referring to equations 3.2.7 ~ 3.2.9, this figure highlights two key effects.

- Sodium channel (governed by the  $m$ ,  $h$  functions) has the fastest change.
- The “n” and “h” channels are significantly slower and combined with the flat-lined  $m$  function explain the refractory period following a successful AP.

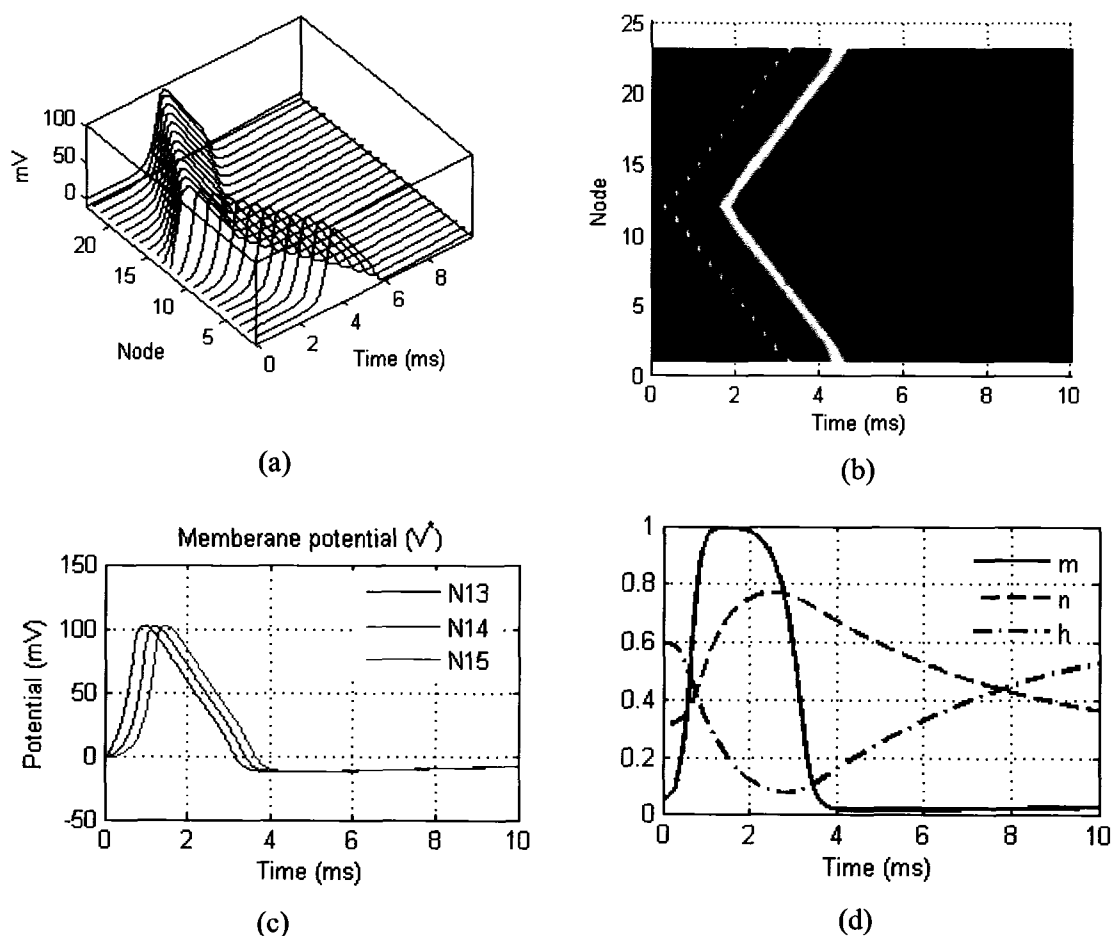


**Fig. 4.19:** Three forms of visual representation of the action potential (AP) in nerve segments and the variation of ionic gating functions for a randomly picked node (in this case 13).

#### 4.2.2 AP propagation velocity.

As mentioned in the previous sub-section, computation of AP propagation velocity, though not vital, is necessary for the following reasons:

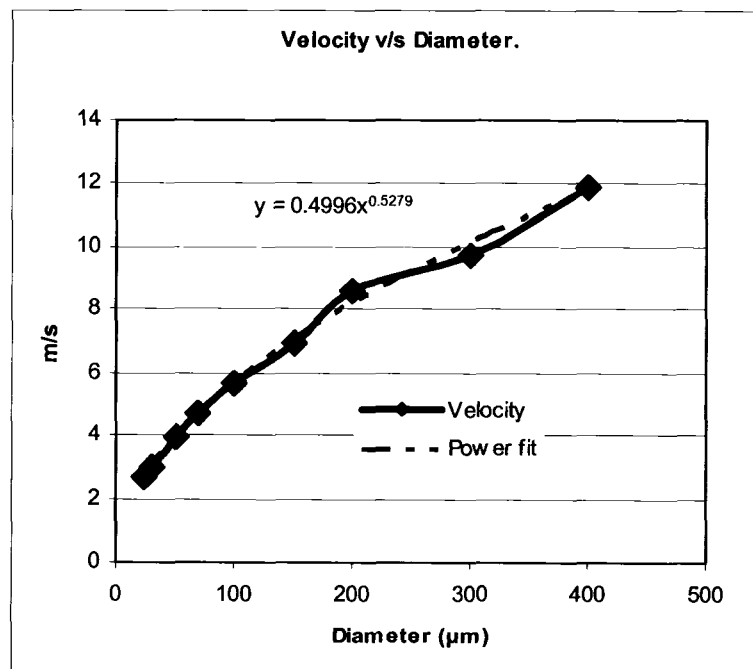
1. As a validity check of the intrinsic modeling scheme for the nerve segments.
2. It is an important element for explaining the inherent problems with AC current based conduction block interruption schemes.

Figure 4.20 shows the variation of the propagation velocity as a function of the unmyelinated axon diameter. The figure also shows the superimposed power fit using the axon diameter as the variable. The resulting best-fit relationship is given by equation(4.1).

$$v = 0.5d^{0.5279} \quad , \quad (4.1)$$

where,  $v$  is the velocity (m/s) and  $d$  is the axon diameter ( $\mu\text{m}$ ). This agrees very well with the established relationship of  $v \propto \sqrt{d}$  [123] for the unmyelinated nerve segments. The computed velocity relationship (not shown in the figure) for the myelinated nerve segments is given by equation (4.2) which *also* agrees very well with the known  $v \propto d$  relationship [71].

$$v = 2243d^{1.0879} \quad . \quad (4.2)$$



**Fig. 4.20:** Computed velocity dependence upon the axon diameter for unmyelinated nerves.

#### 4.2.3 Conduction block using continuous electric stimuli (DC/AC).

As mentioned in chapter two, most of the currently explored methods for achieving the conduction block in nerve segments involve electric stimulus (particularly AC/DC current injection). The reasons were also mentioned in chapters two and three, but are being summarized here to underscore the significance. AP is a systematically and progressively moving potential build-up at successive nodes. It resembles a wave front. Therefore, in order to prevent the next node downstream from being excited, it is imperative that there be an extraction of the charge (electrical energy) from a preceding nerve membrane out into the surrounding medium which can be considered as ground. Extraction of charge implies some form of current application, either a fixed voltage or an alternating interrupt signal. However, the main problems with such conventional methods include (but are not limited to):

- Tissue damage due to excessive joule heating when employing DC interruption currents;
- Very strong possibility of the interrupt signals launching *their own AP*;
- More susceptible to deviations in location of application;
- Interrupt signal timing is not known *a-priori* (for AC signals);
- Very narrow effective frequency bandwidth (for a given axon diameter) in the case of AC signals;
- Amplitude of the interrupt signal also not known *a priori*.

In this subsection, we highlight some of these scenarios by way of simulations serve to validate our modeling schemes and are in line with those reported elsewhere. Figure 4.21 shows the simulation of AP conduction block by using a DC pulse. The nerve segment is  $23.8 \mu\text{m}$  in radius. The excitation is applied at node 2 and the interrupt signal ( $-0.4\mu\text{A}$ ) is applied at node 13. The DC pulse was applied for 1.8 ms starting at 2.9 ms. Figure 4.21a shows a successful AP block with these parameters. However, if we just vary the interrupt amplitude from  $-0.4\mu\text{A}$  to  $-0.35\mu\text{A}$ , with other parameters kept the same, the AP block is incomplete – as shown in figure 4.21b. Only a slight, temporary delay occurs. Upon keeping the interrupt amplitude at  $-0.4\mu\text{A}$  and varying the interrupt pulse width from 1.8ms to 2.5ms, we notice that the AP is again not blocked. This is highlighted in figure 4.21c. If that is not enough variability, merely changing the start time of the interrupt pulse from 2.9 to 3.0 ms causes a failure of AP block and is shown in figure 4.21(d). It should also be pointed out that the interrupt signal amplitude was determined using a heuristic approach and not analytically. One way of circumventing the problem of figuring out the start and stop times for the DC interrupt pulse is to keep the pulse applied for the entire simulation time. However, this has a significant disadvantage of injecting

an unreasonable amount of energy that could, in turn, potentially cause permanent tissue damage (nerve and surrounding area) due to localized heating.

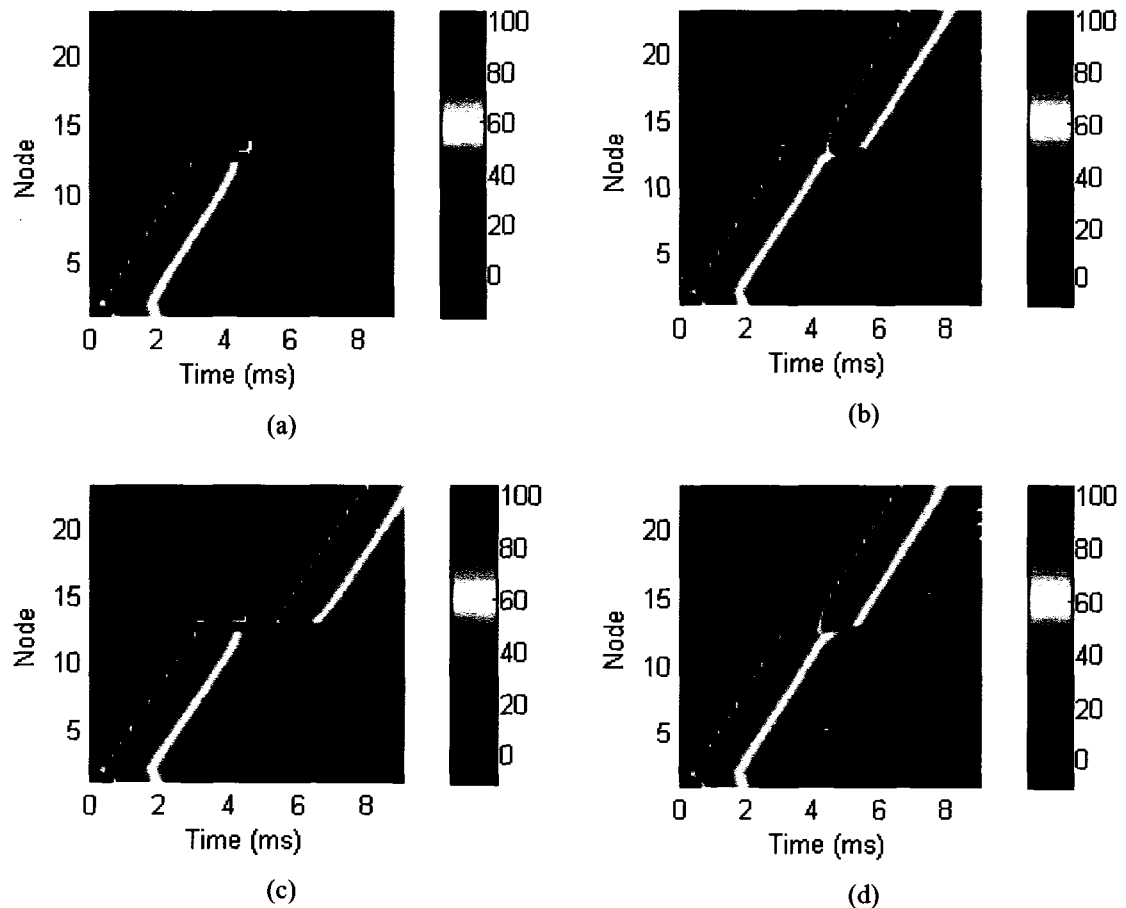


**Fig. 4.21:** AP block with DC pulse. Different panels show the problems in achieving a robust block due to extreme sensitivity of the method to different pulse parameters.

Use of an AC interrupt scheme alleviates the heating related tissue damage possibility. However, it is also wrought with its own set of problems. The next set of figures highlight the same. The axon diameter used in the next set of results is  $24 \mu\text{m}$ . A  $9\text{kHz}$  interrupt signal with  $4\mu\text{A}$  amplitude is used. The signal is applied from start to  $7.9\text{ms}$  time period and a clean AP block is observed as shown in figure 4.22(a). However, despite the fact that the energy content delivered by the AC signal is low, it does not allow for the application of the interrupt signal beyond a preset stop time. This is seen in figure 4.22(b) where the interrupt signal was kept on for a few milliseconds more. As is evident, the initial AP is blocked; however, the interrupt signal launches its own AP. Even in the absence of an actual excitation, the interrupt signal is

capable of generating the unwanted AP signals as is shown in figure 4.22(c). The initial AP is blocked by the AC signal but launches its own AP at a later time.

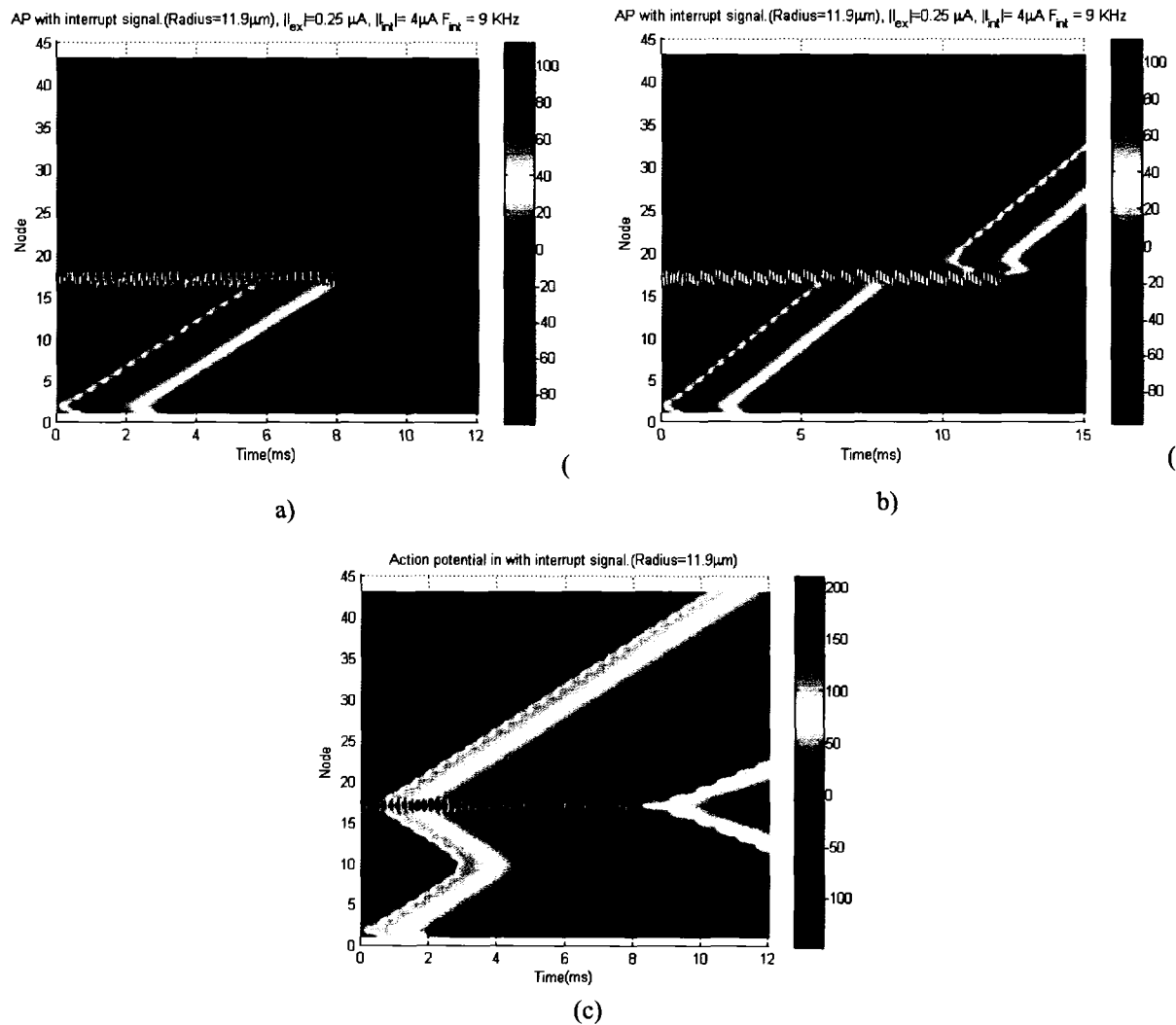


**Fig. 4.22:** AP block with AC interrupt signal. Different panels show the problems in achieving a robust block due to extreme sensitivity of the method to different pulse parameters.

The frequency bandwidth limitations were highlighted in chapter 2, Table 2.1 in which the start, stop and frequency of the signal required for a clean AP block were tabulated for axons at a few different diameters. Again, it must be noted that the values mentioned in Table 2.1 were not obtained by some analytical formulation. They were determined heuristically and will require several test simulations for another set of axon diameters. Regardless, most important to remember is that even though electrical methods of conduction block are the most common ones being explored and employed, they are wrought with problems. There is a clear need for an alternative that is more robust. In the following sections of this research, details of such an

electrical alternative for achieving AP block without the disadvantages of the conventional schemes will be illustrated and discussed.

#### 4.2.4 Modifying the shunt conductance.

In figure 3.11, the modification proposed to the existing electrical schematic of the nerve segment has already been presented. However, before we explored the possibility that electroporation can be used to achieve this, it was more appropriate to determine whether modifying the shunt conductance would *actually* be a successful proposition. In order to test this, several simulations were performed to evaluate the minimum shunt conductance required to block the AP in nerve segments of varying diameters. The resulting values are shown in figure 4.23a and 4.23b.

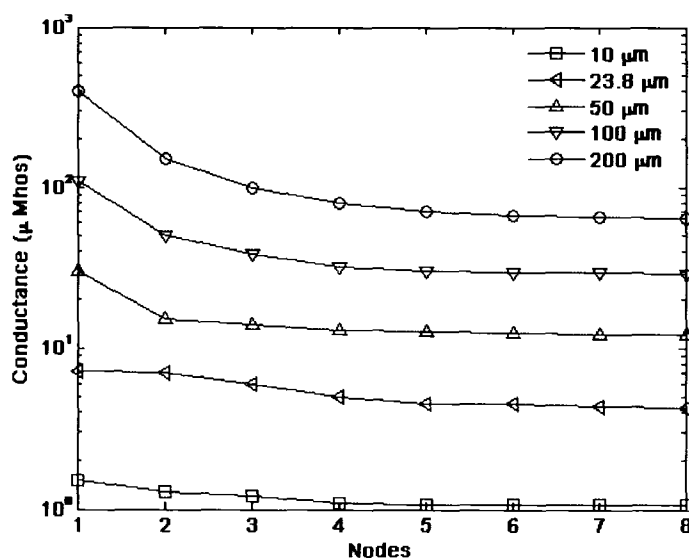


**Fig. 4.23a:** Minimum shunt conductance required for AP block in unmyelinated nerve segments as a function of number of nodes where the conductance was modulated.

Figure 4.23a shows that the shunt conductance required for an axon of higher diameter is also high. This seems logical since an axon of larger diameter has a lower longitudinal inter-nodal resistance. So in order to rapidly leak out the propagating charge before the membrane potential can build up, the shunt conductance also needs to be high.

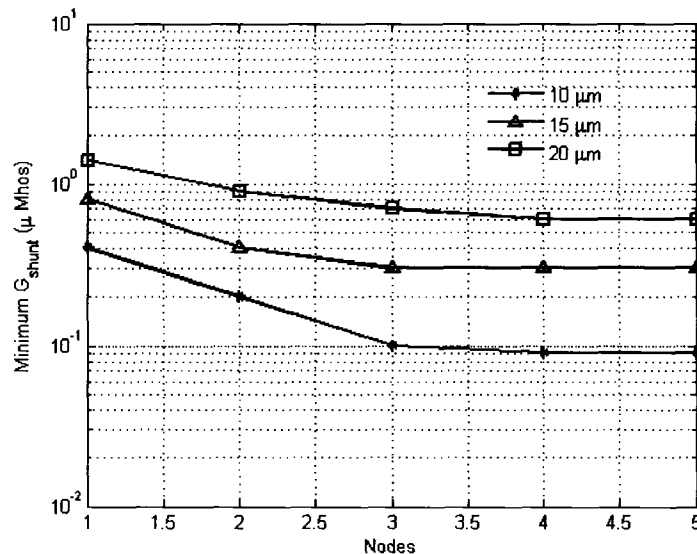
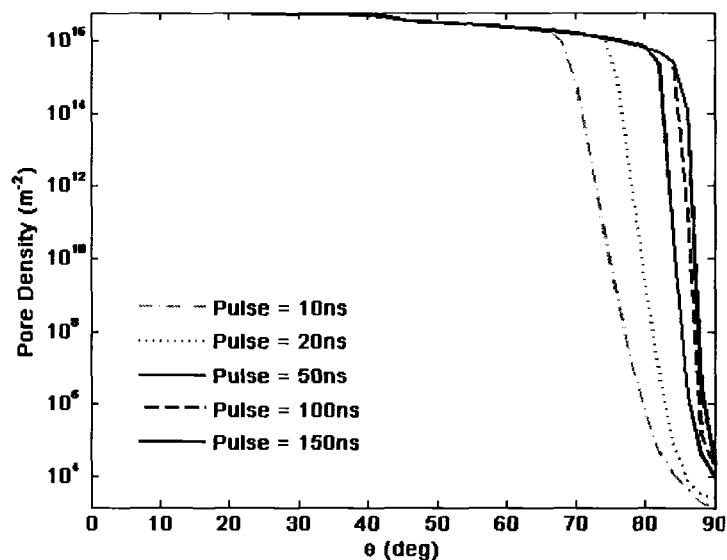


**Fig. 4.23b:** Minimum shunt conductance required for AP block in myelinated nerve segments as a function of number of nodes where the conductance was modulated.

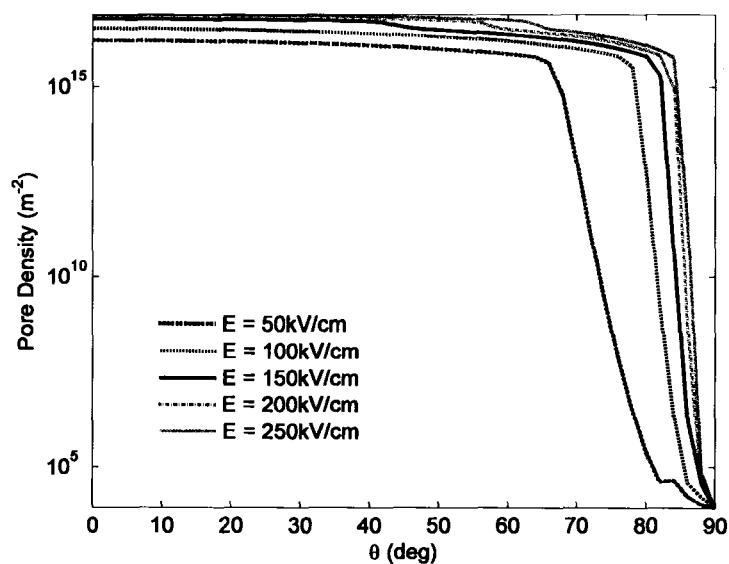
The other point revealed in figure 4.23(a) is that if more than one node were to be affected, the shunt conductance required for AP blockage would drop till it eventual saturation. This again seems intuitively correct since the load of draining out the AP charge is now collectively shared by several nodes. For the sake of completeness, the shunt conductance variation for myelinated nerve segments is shown in figure 4.23(b). From figure 4.23(b), we also notice that the shunt conductance requirement for myelinated segments is  $\sim 5$  times lower than those for the unmyelinated case. This might be because in such nerve fibers, the AP conduction is saltatory in nature, i.e. the AP “jumps” from node to node. In effect the shunt conductance for a given diameter needs to be high enough to merely prevent the myelin capacitance from not charging completely.

In chapter three, section 3.2.3, it was shown that given a pore-density, the resulting shunt conductance could be computed using the relationship given in equations (3.2.22) – (3.2.24). For the above minimum shunt conductance needed for AP block, the next task is then to evaluate the pore-density levels obtainable using the short electrical pulses. Figures 4.24(a) and 4.24(b) show the pore density as a function of the angular deviation, computed when the duration and amplitude of the external electrical pulse was varied. In figure 4.24(a), a 150kV/cm electric field was applied for different pulse durations. The two key aspects of this figure are that for a given amplitude, the initial pore density for in the region close to  $\theta=0^0$  is the same irrespective of the pulse duration. Obviously, this can only hold at high voltage

amplitudes, well above the threshold for electroporation. However, higher pulse durations allow for the pores to progressively appear in the region further away from the polar caps.



(a)



(b)

**Fig. 4.24:** Angular pore density variation to E fields of: (a) varying pulse width at 150 kV/cm, and (b) varying amplitude.

A similar effect is observed when the pulse amplitude is varied. The difference in amplitude is manifest in the change in the pore density level and the angular deviation in the porated regions. Despite the information conveyed, these figures still do not provide the real information of



interest being sought here, i.e., the conductance values that such pulses could achieve. Table 4.3 highlights the values computed for some typical pulse amplitude – pulse width combinations. The nanosecond durations and amplitudes are characteristic of the pulsars developed and in use at Old Dominion University’s Center for Bioelectrics (ODU-CBE).

**Table 4.3:** Resulting shunt conductance with standard Electric field and pulse width combinations

Maximum amplitude (kV/cm)	Pulse duration (ns)	Conductance (S)	AP Block?
100.0	20.0	$3.0777 \times 10^{-4}$	Yes
100.0	50.0	$3.8265 \times 10^{-4}$	Yes
100.0	100.0	$4.3744 \times 10^{-4}$	Yes
150.0	20.0	$5.9528 \times 10^{-4}$	Yes
150.0	50.0	$7.0608 \times 10^{-4}$	Yes
150.0	100.0	$7.8385 \times 10^{-4}$	Yes
200.0	20.0	$7.7152 \times 10^{-4}$	Yes
200.0	50.0	$9.0424 \times 10^{-4}$	Yes

Looking at the conductance values in this table and comparing this with those in figures 4.23(a) and 4.23(b), we notice that the values are much higher than the minimum required for a singular node electroporation.

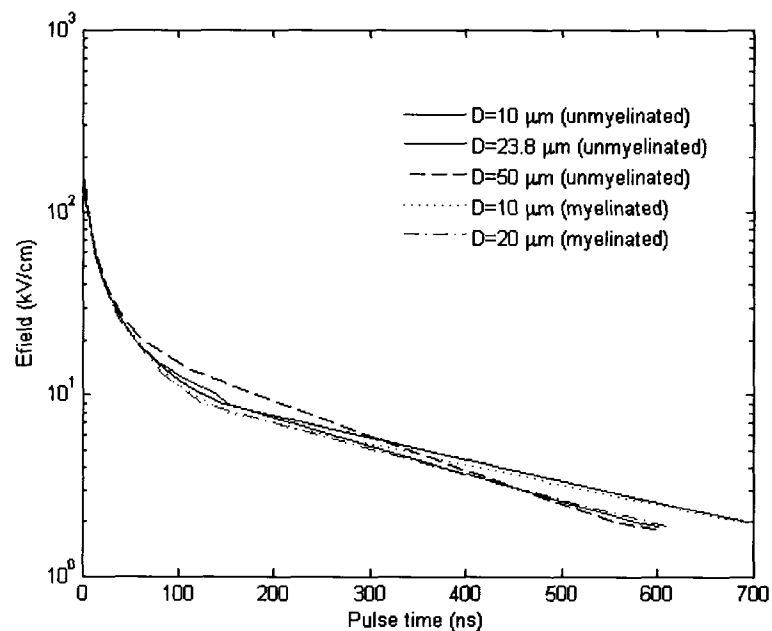


**Fig. 4.25:** Strength-duration curves for axon of different diameters for achieving minimum  $G_{shunt}$ .

This implies that the pulses should be able to cause sufficient poration and hence, the requisite change in conductance. The results also lead to the following question – what is the *minimum* pulse with and/or E-field amplitude necessary to achieve the shunt conductance required for a given axon diameter. This is answered by the strength-duration curve shown in figure 4.25.

Comparing this figure with the values in table 4.3 and considering a  $20\mu\text{m}$  axon diameter, we notice that in order to generate enough pores to attain the required shunt conductance, a  $1.7\text{kV/cm}$  electric field is required for  $600\text{ns}$ . That is a fairly low electric field, especially when compared to amplitudes as high as  $100\text{ kV/cm}$  routinely achieved at ODU-CBE. These results look promising and bode well for AP blockage of neural signals through electrical pulsed stimulation. It bears repeating that for myelinated axons, the conductance requirements are lower by a factor of  $\sim 5$ .

#### 4.2.5 Application to multi-branch nerve segments

So far, the results presented in section 4.2 have dealt with singular nerve segments. To ensure that the proposed AP block scheme also works when the nerve segment branches, it was imperative that simulations be performed where a realistic branching of the nerve segment was simulated. Figure 4.26 shows a branched nerve system where the main segment branches at two levels. At each successive level the axon diameter reduces by a factor of two.

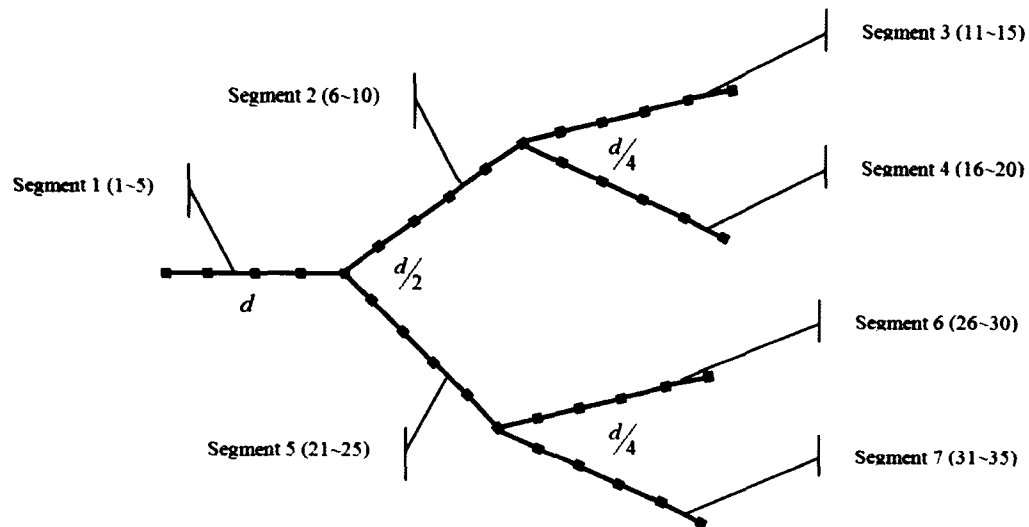


**Fig. 4.26:** A sample multi-branch layout.

In figure 4.26, the main axon segment (1) has a diameter  $d$ . The second level branches (segments 2 and 5) have a diameter of  $d/2$ . The third level branches (segments 3, 4, 6, 7) have a diameter of  $d/4$ . Each segment has been discretized to have 5 nodes. The main segment has a diameter of  $23.8 \mu\text{m}$ . The excitation is provided at node 2.

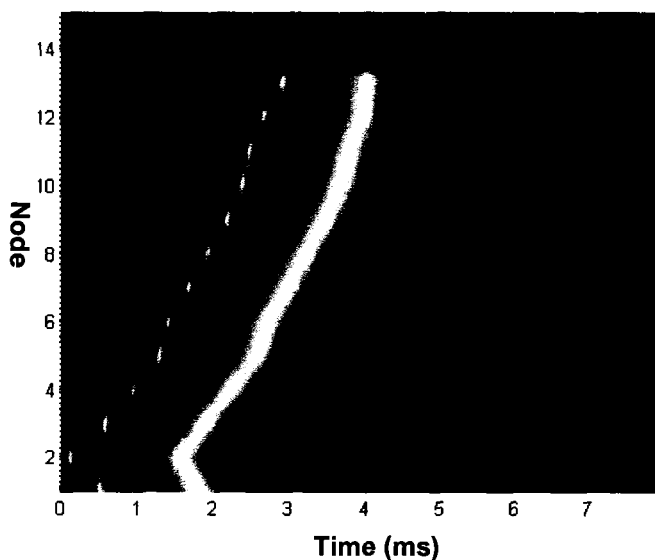


**Fig. 4.27:** AP initiation and block using electroporation in a multi-segment unmyelinated nerve.

For simplicity in book keeping, the electroporation was simulated at node 14. The resulting AP propagation and block is shown in figure 4.27. From figure 4.27, the change in AP velocity is clearly visible. Also visible is a clean AP block at node 14. Since the AP was initiated at node 2, we can also see its propagation in the other direction (towards node 1). The essential exercise of this simulation was to ensure that the proposed AP block scheme employing the high intensity, ultra short pulses was viable for multi-branch nerve segments as well.

#### 4.2.6 Experimental AP inhibition and validation.

So far in this chapter, each result presented has been that from a simulation study. While such results are good to support a hypothesis – it is always better if experimental results can also be incorporated and explained. This lends credibility and realism to the numerical predictions. However, given the lack of experimental studies, only one specific result is presented here. It is discussed and explained using the simulation schemes presented so far.

In this section, we compare an actual experimental observation of neuro-muscular disruption on a rat with our simulation scheme, and attempt to explain the phenomenon based on high intensity, short duration pulse (HISDEP) generated electroporation of the nerve network. The experiments have been discussed in detail elsewhere [124]. These were conducted to study the possibility of neuromuscular disruption by the application of ultra short electrical pulses. The subject was a male Sprague-Dawley rat. In order to elicit a “muscular twitch” from the rear right paw, the cortical motor region in the left hemisphere was stimulated using two separate electrodes. Another set of electrodes were connected to the left hind paw and the right back side, to provide a cross pathway for the interrupting HISDEP. The interrupt high voltage (HV) stimulus was a 600ns pulse with variable amplitude (1.3~16kV). In these experiments, twitch inhibition for pulse amplitude of ~15kV (or more) and energy content of ~30mJ (or more), were observed. It was thus shown that the application of a 600 ns electrical stimulation could achieve the objective of blocking the neural traffic.

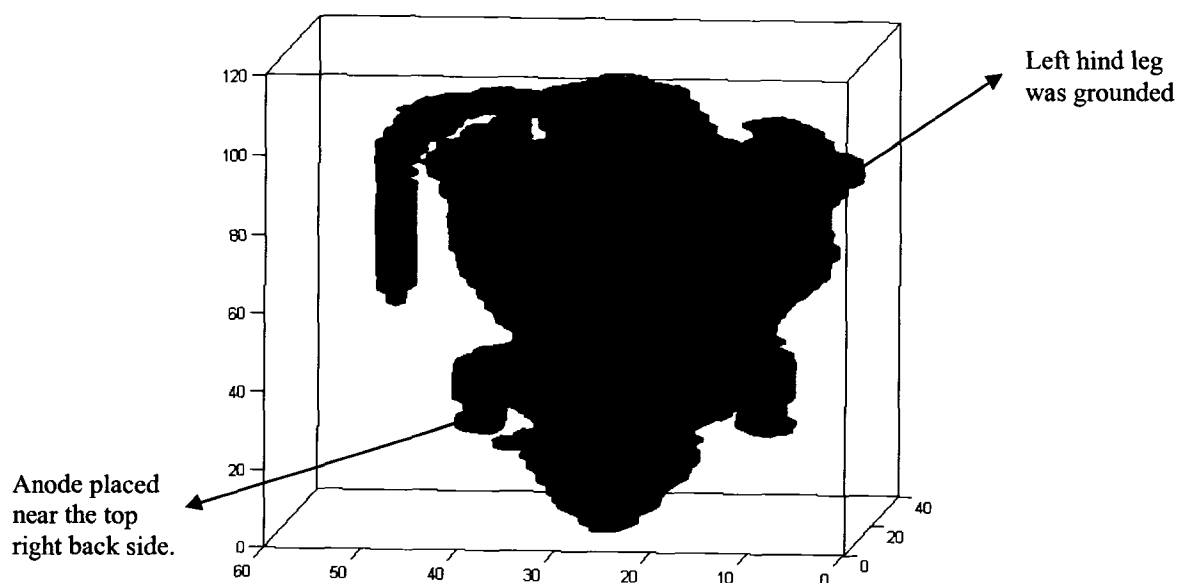


**Fig. 4.28:** Volumetric rendering of the simulated rat model. The electrode placement is also shown. The axes represent length (Y), width (X) and depth (Z). The spinal region was approximated to be running along the length between  $X=24\sim 26$  mm and the between  $Z=4\sim 6$  mm.

In order to simulate this experimental setup, the whole body of a similar rat with two electrodes “placed” as the experimental locations was simulated. The applied anode voltage was taken to be 16 kV, 600 ns rectangular pulse applied at  $x=27$ mm,  $y=33$ mm, and  $z$  between 3-

5mm. Thus, the anode was a thin vertical wire of 1 mm square cross-section, inserted about 2 mm into the rat. The cathode was the left hind paw spanning  $x=8-12\text{mm}$ ,  $y=97-101\text{mm}$  and  $z=22\text{ mm}$ . The rat model had a total height of 22 mm, with  $z=0$  denoting the top and  $z=22$  the ground plane. The rendered model of the simulated rat is shown in figure 4.28. The dimensions were: 114 mm (length along  $y$ -axis), width of 51 mm (along  $x$ ), and a depth of 22 mm along the  $z$ -axis. The resulting spatial potential distribution and time-dependent electric field profiles were computed. The electric fields were computed in the region defined by  $x=25\text{ mm}$  along the entire length (parallel to the  $y$ -axis) of the rat model at all times. The resultant electric field is shown in figures 4.29(a)-4.29(b).

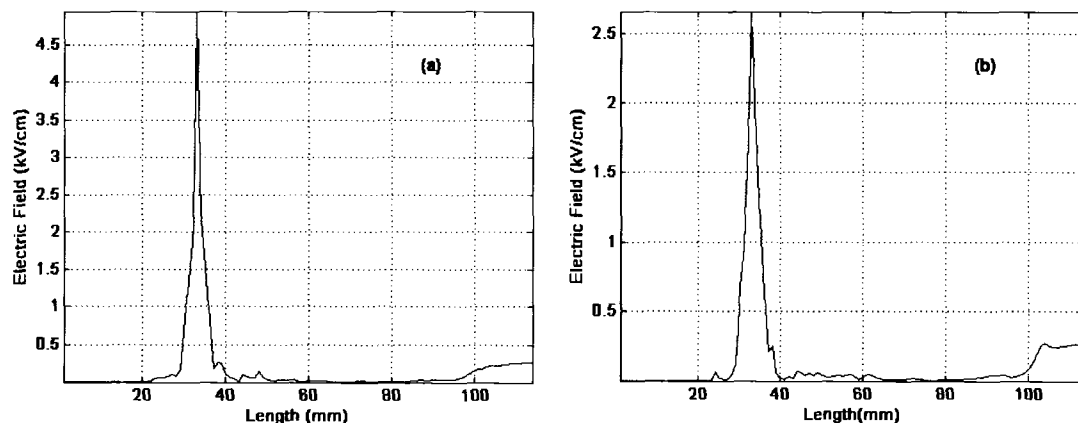


**Fig. 4.29:** Computed electric field along the spinal region along the entire length of the rat model. The plots correspond to two vertical planes, (a)  $z=4\text{ mm}$ , and (b)  $z=5\text{ mm}$ .

The two figures correspond to profiles across the  $z=4\text{ mm}$  and  $z=5\text{ mm}$  slices with  $x=25\text{ mm}$ . Assuming the spine to lie below the skin, the  $z = 6\text{mm}$  slice would be close to the spinal section. The peak value in Fig. 4.29(b) is seen to be slightly above  $2.5\text{kV/cm}$ . For the spinal column to be located in this area and to have an effective diameter of  $\sim 20\text{ }\mu\text{m}$ , the minimum shunt conductance from figure 4.21b required to affect a complete AP block is  $\sim 1.4\text{ }\mu\text{Mhos}$ . More specifically, figure 4.23(b) reveals that for a  $20\text{ }\mu\text{m}$  diameter, myelinated nerve fiber (since the spinal column is comprised mostly of myelinated nerve fibres), and the electric field required to fashion  $1.4\text{ }\mu\text{Mhos}$  conductance via electroporation is about  $1.7\text{ kV/cm}$  for the 600 ns pulse. This value is in very close agreement with the peak field predicted in Fig. 4.29(b) near the rat's spine location for the external 16 kV, 600 ns excitation. Hence it is logical make the hypothesis that perhaps the primary pathway for stimulating the hind leg is via the spinal column and that the HISDEP interrupts this movement by electroporating a section of the spine.

This membrane breakdown due to formation of localized nano-pores is temporary, but it effectively results in a complete leakage of the stimulating energy propagating from the cortex. It should also be pointed out that in the very *likely* scenario that more than one “node” or region of the spine being affected from this breakdown, the required shunt conductance for “twitch inhibition” would be lower and consequently could be achieved by a shorter HV pulse, or one of slightly lower amplitude.

#### 4.2.7 More recent observations that may support alternative AP block mechanisms

The present simulations and associated theory supports the above hypothesis of nerve electroporation. However, given the complexity of the biological system and the plurality of underlying mechanisms and processes, other explanations of the nerve conduction block arising from application of Ultra-short High Intensity pulses are possible. In this context, it must be mentioned that experimental work relating to HISDEP based bio-responses has been on-going at the Center for Bioelectrics within Old Dominion University (CBE-ODU) using patch-clamp methods. One of the phenomenon that have been observed in such patch-clamp experiments [A. G. Pakhomov, Private Communication] is that HISDEP application tends to severely inhibit the  $\text{Na}^+$  ion channel uptake across membranes. Since  $\text{Na}^+$  ion channels are also present in nerve segments, it is then possible that the observed AP blockage may arise from HISDEP effects on  $\text{Na}^+$  ion channels. Since AP launches and their propagation depend on the timed-triggering of both Na- and K-channels, any process that works to alter or disrupt such channels could be a pathway for signal blockage. Specifically, since AP generation is intimately connected to Na-channel activity, any adverse effect or destruction of this ion pathway would impede AP generation. It should also be mentioned that this recent finding becomes more pertinent in light of works published earlier by some researchers [125, 126]. They have tried to explain the Sodium gating function (i.e.  $m$ ) in the original HH model by attempting a more physically realistic representation. Some qualitative discussion of this aspect is included in possibilities for future research in the next chapter.

## Chapter V

### Conclusions and Suggestions for Future Work

#### 5.1 Introduction

Having presented all the aspects of this research work (as enumerated in the first chapter), this chapter presents a brief summary of this entire dissertation research effort, the overall implications and salient features, our unique contributions in this field, and finally some relevant and germane suggestions on how this work can be extended to broaden the present application and scope. Ideas relating to the proposed modeling schemes, action potential block methods and their analyses are also presented. Given that this dissertation so far has followed the structured approach of full body modeling, followed by neural segments and AP block schemes, the same format will be used for this concluding chapter.

The summarizing conclusions have been broken down, for convenience, into two broad categories that effectively address the various aspects of this dissertation research. These are: (a) Full body modeling, and (b) Modeling Action Potential propagation and the conduction block in nerves. These discussions are followed by scope for future work and extensions to micro-level systems such as cell clusters and tissues.

#### 5.2 Full body modeling

There were two key reasons why this part of the current research work came to be: (1) despite the dramatic surge in using simulation techniques – full body analysis is quite primitive at best; (2) in order to study macro (physiological response) or micro level (activation of neural pathways), it is necessary to compute the electric potentials in the surrounding tissues. As has been mentioned, full body imaging and examination methods such as MRI, CAT, etc. have existed for over two decades. However, these methods are no more than devices to peek into the living body. While practical application of such devices in order to “capture visual/ imaging” data is useful, it is more important to be able to perform analysis, perform computations for meaningful predictions, and draw meaningful conclusions from the raw data. Computations to perform any viable analysis involve:

- a) A robust algorithm
- b) Computation resources.

Though these two might not seem significant, issues such as physical memory and computation nodes become severe bottlenecks (as was discussed in chapters 3 and 4) when performing almost any numerical analyses.

Only with recent advances in computational science and the availability of electronic hardware, have some researchers started venturing into simulation analysis on small bio-volumes and localized tissues. The other reason for the relative scarcity of schemes for full body modeling and analysis is that tissue level complexity is extremely hard to capture (incorporate) in the computational process. Adequate incorporation also requires accurate and microscopic data mining, e.g., the electrical characteristics of the various tissues and organs that comprise the whole body. As mentioned earlier, volumetric imaging data does exist. However, that does not directly translate to usable electrical properties. When the attempt to develop a system to perform the full body analysis was initiated in this research, it was originally assumed that a sequential computational system would suffice. Given that the mathematical model for the bio-system in this research involved solution of linear, simultaneous equations that were coupled in time, some very critical lessons and requirements came to be recognized very rapidly. They were:

1. Decoupling these equations in time would not be feasible for any intent and purpose.
2. Deployment (applicability) of the simulation scheme would require a very large system of equations to be solved, associated with the fine spatial resolution of a three-dimensional volume into microscopic details.
3. The only way to perform such large scale computation was to develop a distributed approach for the numerical solution.
4. Furthermore, tissue model data has to be combed prior to being fed to the computation engine to prevent computation phase errors. To put this in perspective, one of the raw model files that were received consisted of tissue types that were listed to have *negative* conductivity.
5. Standard pulse shapes such as trapezoidal, rectangular, etc. were too restrictive. The ability to incorporate excitation from arbitrarily shaped potential pulses was essential.
6. In order to address real world processes such as ablation, the ability to provide current stimuli, in addition to external voltage driving responses, had to be provided.
7. Different electrodes (size and shape) present a completely different response, as does their placement. Consequently, generalization pertaining to electrode placements, geometry had to be adequately incorporated.



8. Real world volumetric datasets can have different discretization lengths in each dimension in order to eliminate unnecessary resolution in a particular plane. This meant that the numerical system also needed to be flexible enough to accommodate such events.
9. Last but not least, there is a need to perform visualization of the computational results both during and after the entire computations are complete. For example, visualization of the applied pulse and the responses during a specific time interval may be desired. This means that the output form of this system would need to allow in-situ visualization and post-analysis.

The full body modeling scheme that was developed in this research addressed all the above listed issues. Additionally, the following aspects were also included:

- The results were validated using different bio-model shaped and electrode geometries.
- The nuances involving visualization of results were also highlighted.
- The system allowed for arbitrarily shaped bio-models (bodies) to be simulated without loss of edge points by maintaining a systematic Cartesian simulation volume. The additional overhead of incorporating the air region was definitely worthwhile in view of the following advantages offered:
  - i. Applicability to any model shape, and
  - ii. Avoidance of unnecessary complexity in the algorithm which makes it faster than the alternative schema.
- This modeling scheme did not make any assumptions about the shape of the input data set. Hence, just a part of the whole body could also be simulated, if present as a separate bio-model file.
- Since the resulting output contained the computed potential values for each discretized point over EVERY time step, post analysis including those listed below (but not limited to) could be performed:
  - i. Different orientation potential visualization.
  - ii. E-Field calculation (over different slices in each orientation).
  - iii. Current density along a slice or a line

We have published a few salient points of our distributed full body modeling scheme [127] and its experimental application [128]. However, there is definitely room for extending the

capabilities of this system, and these will be listed in the last section of this chapter. That said, it is certainly hoped that this research work will serve to address a void that currently exists in the simulation community. This work should also find application in: (a) clinical studies, and (b) development and design of better, non-lethal directed energy devices and several other applications as listed in chapter 2.

### **5.3 Modeling Action Potential and Conduction Block**

Starting with the original HH model, many researchers have been exploring possible methods for action potential conduction block. This is of importance given the vast number of potential applications in therapeutic, physiological and other areas. However, as discussed in the background review in chapter 2, almost all the methods that have been proposed involve either some form of relatively long current injection and/or chemical introduction. There are distinct drawbacks with each method. This research work has attempted to address the existing deficiencies by contributing to the development and understanding of a novel approach to electrically-activated conduction blockage. In particular, our proposed method alleviates the following problems that are intrinsic to other proposed methods:

- Possibility for tissue damage due to excessive energy injection – as could happen with continuous DC and AC pulse based methods;
- Variability in successful conduction block by AC pulses arising from frequency and timing issues

The method discussed in this dissertation provides robust conduction blocks through the application of nano-second pulses. In addition, the refractive period intrinsic to each AP passage would seem to allow for the application of these interrupt pulses in a discrete manner. This further enhances the viability of their usage.

A modified lumped parameter cable model was proposed to account for electroporative effects. Application of high intensity pulses has been explored fairly extensively, especially with regards to their effects on membranes. Therefore, it seemed only logical to explore the possibility of modulating the trans-membrane conductance by applying ultra-short electrical pulses. The main mechanism was shown to be membrane conduction modulation arising from electroporation. Despite the novel simulation work and concepts developed here, there is however, room for further improvements and the consideration of other mechanisms. These possible aspects and mechanisms are briefly discussed here under scope for future work.

Despite the extremely common adoption of the HH model by many researchers, there has been some progress [125, 126, 129, 130] towards creating more physically plausible models

of  $\text{Na}^+$  channel gating. As mentioned in section 4.2.7, some recent experimental observations at CBE-ODU have shown possible destruction of  $\text{Na}^+$  channels, which did not recover for extended periods. Since AP block could also be caused by Na-channel destruction, a closer look at a physical model for  $\text{Na}^+$  channels perhaps becomes necessary. For this purpose, the model as proposed in [125] is now briefly re-visited.

The Edmonds research work [124] essentially proposes a two system, dipole cluster model, which controls the state (open/close) of the Sodium channels. One of these two systems, identified as system “N” consists of dipoles that can move only parallel to the membrane plane. The other dipole/charge cluster system is believed to function normal to the membrane plane and is the one that actually reacts directly to any applied electric potential across the membrane. This system is called the “Q” system. The opening and closing of the channel can then be explained on the basis of these “Q” and “N” clusters, in the following manner.

Referring to figure 5.1, in the rest state the two systems are oriented such that the charged Q-system (shown as positive in Fig. 5.1) lies at the bottom end of the membrane. The N-system, containing charges of the same polarity lie at the opposite end of the membrane (say the top.) The channel in this state is closed (shown in the left panel of the figure). Upon application of a positive potential across the membrane, the Q system starts to move and transition into a configuration wherein some of the positive charges get translated towards the top end of the membrane.

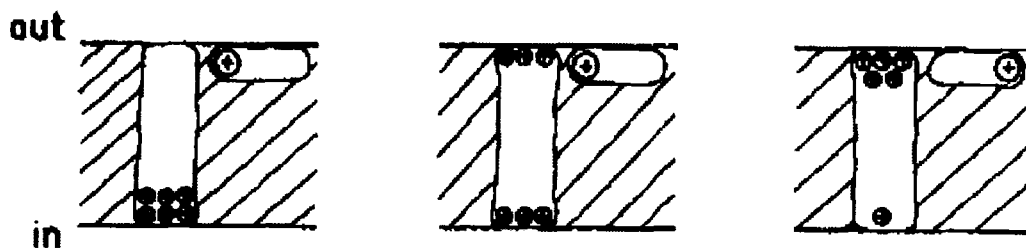


**Fig 5.1:** The two systems (Q, N) represented to highlight, the closed (left), intermediate (centre) and open channel (right) of the membrane. [125]

Once enough charge has accumulated there, the N system (which can ONLY interact electrostatically with the Q system charges) is repelled. This causes a transition (flip) in its default resting state, and eventually the channel opens as shown in the right most panel of the figure. The central section of the figure shows an intermediate stage between closed and open states. Thus, in this model, the application of an external field causes a state transition (or configurational change). As the author of this model notes, *“It is very simple and in particular*

*much simpler than the  $m^3$  model usually employed.*” Obviously, this mechanism does not require the initial bottom membrane Q-charge to be positive. Negative charges at both the Q and N-sites would work equally well. In practice, the existence of molecules such as phosphatidylserine (PS) naturally imparts a net negative charge to the inner membrane.

The reason for highlighting this model was to show the role of electrically driven conformational changes in driving the transitions in a voltage-gated channel through charge displacement. However, the above model does not consider the possible role of electroporation. In principle, though, the use of high-intensity electric fields could not only create pores at sites close to such protein-based  $\text{Na}^+$  channels, but also widen the inner diameter of existing protein structures. The next result would then be the possibility for “mobile charge” outfluxes from within the inner side of the membrane to the exterior portion. Such “externalization” through electro pores, has been demonstrated both experimentally [26] and through theoretical Molecular Dynamics simulations [27, 85, 94, 131] recently, in response to large externally applied fields. A similar process of charge migration could occur through the protein channels.

In any event, the process of applying high-voltage pulses then opens up the possibility to drag charge and alter its relative placement on the overall membrane structure. Thus, the protein channels located near such charge translocation would be affected and change their state, as outlined in Fig. 5.1 of the Edmonds model. The more mobile charges (e.g., PS) present initially at the inner membrane could even diffuse out and strongly populate sites on the outer membrane. Due to the electrostatic repulsion between charges, such charge translocation would require energy and take a long time to recover to its original state. During such time, the state of the protein channels would stay in their altered state. Hence, conceivably, this would be a physical mechanism of altering the channel “destruction” and preventing it from “normal” operation following strong voltage-pulsing.

The above mechanism might be an alternative response pathway. It would explain AP blockage and also the observed deviation from voltage-controlled behavior in patch-clamp experiments.

#### **5.4 Scope for future work and extension**

So far some summarizing observations about the current research work have been presented. These essentially highlight the current capabilities and novel features of this research. However, there is definitely scope for improvement and extension of this overall technique. Some of these ideas include:

- A symmetric version of the algorithm (which is presented in the appendix) has been implemented on a distributed system. Even though a lot of code optimization has been performed, there still exists room for more.
- For the purpose of this research, the full body modeling scheme was developed using a very specific format of volumetric data provided by the Brooks Air Force Base. However, it could be modified (with minimal overhead) to use other forms of volumetric data sets such as those from MRI, etc. The caveat is that tissue characteristics would need to be mapped out based on imagery analysis. That would not only extend this system to be truly bio-model independent but could also conceivably allow for studying the possible electro-chemical response of bio-subjects in real time.
- It is also possible to perform the full body modeling using a “segmented approach” wherein each anatomical section is simulated independently. However, this is not as trivial as it seems, given that nodes are coupled to each other spatially as well as in time. Nevertheless, it will definitely extend the simulation capability of this work several fold for the same given computation resources.
- The distributed computation model for the full body modeling scheme could be made more interactive by providing a GUI front-end that would allow the end user to dynamically specify the electrode points, define input pulse shapes, specify other geometric entities, and output file format. Currently, all this is done at the command line using several scripts written in MATLAB® and F90.
- In the process of this research work, both the myelinated and unmyelinated nerve segment systems were validated. It was mentioned earlier that discrete pulses for the purpose of AP block could be employed. However, a more detailed study needs to be undertaken to clearly identify the refractory period in different nerve segment configurations.
- Even though modeling studies have been performed on myelinated nerve segments, the basic assumption made was that the shunt conductance modulation occurs only at the Nodes-of-Ranvier – i.e. the unmyelinated segments. Though such an assumption does not violate or critically compromise the end result, a more realistic system would also allow for the possibility of myelin sheath electroporation.
- Based on the simulation studies and background studies, it has been shown that refractory periods for single nerve segments can be as long as ~50 ms. However, it should be mentioned that this value does vary for branched systems and also for those

segments that may have variable diameters. A more detailed study is in order to explore these aspects.

- Focused application of electroporating pulses at the nerve locations is an assumption that was made for the sake of partial simplicity. However, in real-world applications, it may be more prudent to also incorporate modulation/attenuation of the applied pulse owing to the surrounding tissue where the nerve is embedded.
- Electroporation of a nerve membrane was shown to be a plausible basis for AP blockage. However, there could be other explanations and intrinsic processes that could conceivably be responsible for the AP block. For example, sodium channels embedded within nerve membranes could be destroyed or inactivated by a sudden electrical jolt arising from the application of a high-intensity, nanosecond pulse. Preliminary experimental data obtained at CBE-ODU is indicative of such sodium-channel effects. Since AP launch and propagation is intimately linked to sodium-channel activity, it is quite likely that any detrimental effect of voltages on such channels would lead to AP blockage. Such phenomena merit detailed study, and should be modeled to evaluate alternative pathways and mechanisms. It is very likely that multiple processes are at work, each dominant and operative over different regimes. In the interest of quantification and for clarifying the relative role of such competing mechanisms, a more detailed study of the voltage-induced, channel related bio-electric phenomena is warranted in the near future.

One of the more latent objectives of this research work was to provide a “suite” of models that would address the entire spectrum of tissue systems. The full body modeling system was designed to provide a “macro” level analyses capability of the tissue response. The nerve segments and branches were studied because they are the primary pathways of consequent physiological changes. While the focus was on voltage-induced nerve membrane phenomena, the numerical simulation methods developed could easily be extended for the analysis of micro-level tissue systems and cell clusters. For instance, membrane poration and the time dependent voltage changes in cell clusters placed within a suspension medium, due to pulses of varying strengths could be examined. A brief description of an application of the current modeling scheme to probe the response of cell clusters is therefore presented for completeness. It is a topical extension of the same general theme.

### 5.5 Extending to micro-level systems (e.g., cell clusters)

Single cells have been the focus of many recent experimental studies – especially with respect to modulating the membrane structure for drug delivery, etc. [1, 31, 133]. However, most of the work that has been done is for single cells and does not provide good time dependent analysis or a higher level of resolution to incorporate cell clusters. In order to include the granular and random size aspects of cells in tissues and clusters, the bio-material can be modeled in terms of a random, two-dimensional, Voronoi [134] network. The Voronoi structure is set up by generating  $N$  random seeds that correspond to  $N$  locations  $(x_i, y_i)$  within the entire simulation region. Polygons are then formed by the intersection of perpendicular bisectors from lines that connect neighboring seeds. The above includes granularity, and variations in the internal disorder can be controlled through the positions of the  $N$  random seeds. Two parameters, (i) the disorder length “ $d$ ” ( $d > 0$ ) and (ii) an angle  $\theta$  ( $0 \leq \theta \leq 2\pi$ ) vary the heterogeneity. Figure 5.2 shows Voronoi networks with different values of the disorder parameter  $d$ . For very small values of  $d$  (e.g.,  $d=0$ ), a completely ordered honey-comb pattern results. In this manner, a collection of cells of random size and shape can be modeled. In addition, gaps between cells can also be represented easily by designating an arbitrarily desired fraction of polygons to be the extra-cellular medium. The electrical characteristics such as conductivity and dielectric permittivity of such cell gaps would be those of the fluid medium. The boundary of each polygon represents a cell wall; hence, it is electrically very resistive under normal conditions. If the electric field across any segment exceeds a critical threshold (typically amounting to a trans-membrane potential difference of  $\sim 1V$ ), then physically, the local conductivity would rise dramatically. It is thus important to compute the transmembrane voltages at each time step, and then make dynamic modifications to local membrane conductivity. Electrically, current flow through the entire volume (including both the cells and extra-cellular fluid) is best represented in terms of a distributed circuit model consisting of capacitive and conductive elements. This approach has been used previously in bio-electrics [96, 135]; however, cell clusters were not incorporated at the time.

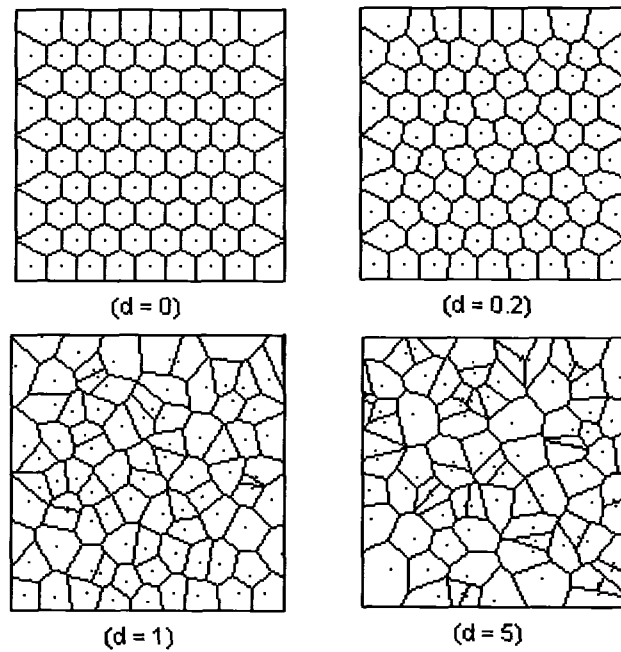


Fig 5.2: Voronoi networks with different disorder parameter "d".

In this scheme, voltages at the center of each polygon could be calculated. This could be done by applying the Kirchhoff current law (KCL) and treating each polygon center as the  $i^{\text{th}}$  node of an N-node circuit.

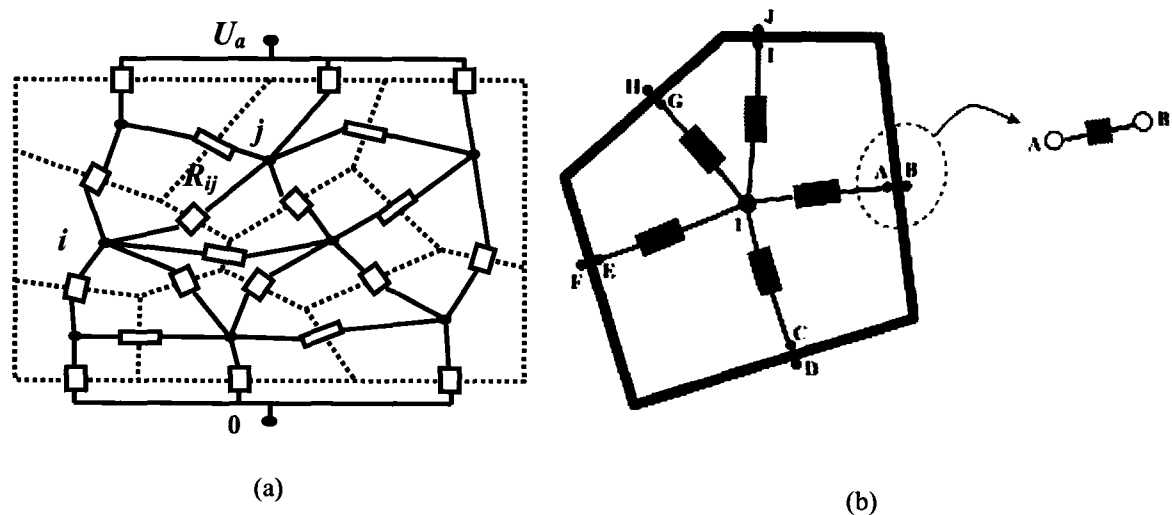


Fig. 5.3. Distributed representation for the electrical analysis. (a) Circuit schematic for nodal analysis, and (b) various R-C electrical elements between nodes.

Figure 5.3 shows the cellular level details and accounts for the resistances of both the fluid and the membrane for a case with  $d \ll 0$ . The resistive elements ( $R$ ) can be obtained from a specification of the material resistivity ( $\rho$ ) and the geometry [i.e.,  $R = \rho L/A$ ]. Representing the



voltage at the node of interest  $V_i$  and all the surrounding “N” membrane nodes as  $V_A, V_B, \dots, V_N$ , one can write the KCL equations as discussed in our previous work [127]. Evaluations of tissue heterogeneity and the role of cell cluster density could be included by assigning appropriate and different permittivity and conductivity parameters to the cells. This is shown in fig. 5.4(a) which depicts an “all-tissue” simulation region, while fig. 5.4(b) has a heterogeneous set of cells placed within a surrounding extra-cellular medium of conductivity  $\rho_{fe}$ . Some of the salient results from this ongoing modeling work are presented hereafter.

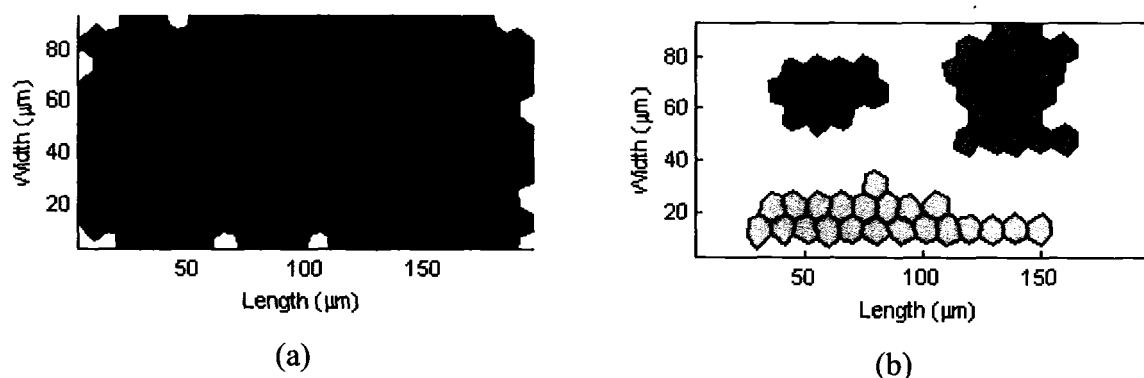


Fig. 5.4. (a) Simulation schematic showing an all-tissue representation for  $d=0$ , and (b) A heterogeneous set of cell clusters separated by extra-cellular fluid for  $d=0$ .

### 5.5.1 Low intensity electric field cases

As an initial test simulation, a completely dense, homogeneous tissue segment taken to be 0.02 cm by 0.01 cm was used with 10  $\mu\text{m}$  cell sizes. For simplicity, a regular honeycomb structure (i.e.,  $d=0$ ) was assumed. The applied pulse was 20V (relatively low amplitude) with rise and fall times of 20ns and an ON time of 2000 ns. In Fig. 5.5(a), a linear potential drop from anode to cathode placed on either side of the simulated tissue segment is seen, as expected due to cell uniformity. Figure 5.5(b) shows the electric field across *every membrane*. Two distinct E-field levels are seen and arise due to the two distinct orientations of the hexagonal cell structure with respect to the symmetrically applied longitudinal external field. Since a potential difference of  $\sim 1\text{V}$  is required to porate a membrane [1, 2, 136], this translates roughly to an electric-field of 2000kV/cm for a 5 nm membrane thickness. Given that the maximum field in Fig. 5.5(b) is only 71.85 kV/cm, none of the cells are predicted to lose structural integrity at the 20 ns instant shown.

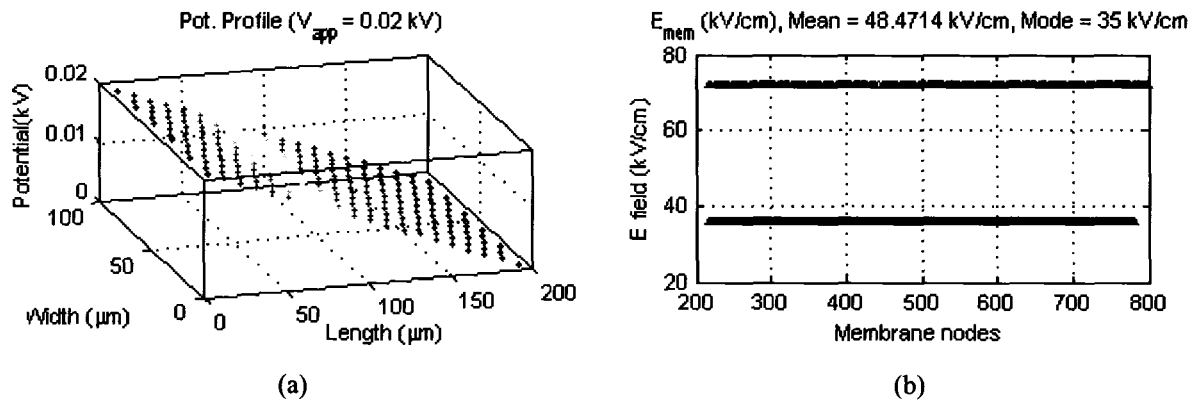


Fig. 5.5: (a) Longitudinal potential at 20 ns, and (b) electric field values at the various membranes.

Having discussed a simple case, results are now presented for a single cluster with different shapes based on varying the “d” parameter. The relative cluster volume fraction with respect to

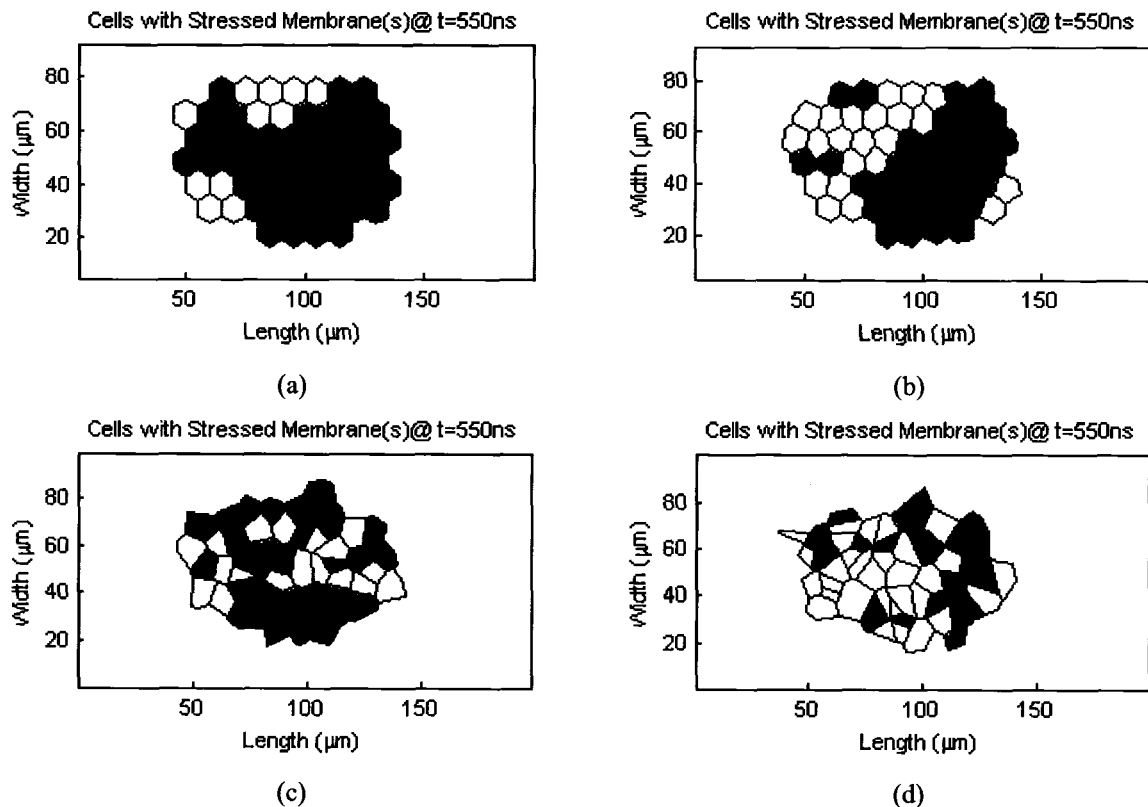


Fig. 5.6. A 550 ns snapshot of the simulated structures indicating porated cells (in grey) for distortion factors of: (a)  $d=0$ , (b)  $d = 0.2$ , (c)  $d = 0.8$ , and (d)  $d=5$ .

the simulation region was 0.275. Figure 5.6 shows a 550 ns snapshot for four different “d” values. This snapshot also indicates the cells predicted to electroporate for membrane fields above the threshold value. The applied voltage was a 20 V unit-step with a 10 ns rise time.

Looking at figure 5.6, it becomes apparent that as the distortion factor increases, there is a progressive reduction in the electroporated cell fraction, shown in grey. This predicted trend can be explained by the fact that as membranes begin to have multiple angular orientations with increasing “d” values, the normal component of the electric field across any membrane segment is more likely to decrease. Only a few “lucky” cells would have membrane segments oriented perpendicular (or nearly so) to the direction of the applied field. It should also be mentioned that as electroporation sets in over time (assuming a sufficiently large external voltage was applied), the voltage drop across the affected cells reduces, and this provides a larger field acting over the remaining cells. The probability and/or rate of electroporation is then dynamic and increases with time. Hence, the difference between regularly shaped and the more irregular cells, is expected to reduce somewhat at later times.

### 5.5.2 High intensity electric field cases

So far the electroporative effects of a relatively low voltage amplitude pulse have been presented. In general, for practical applications, it would be beneficial and fruitful to optimize the pulse-width at a given external voltage for achieving the highest effect for a desired cell type or tissue composition. Such variable pulsar systems can be built as reported recently [137] to enable variations in duration and/or voltage amplitude. *For example, total electrical energy levels from the external pulsing sources similar to those generated over micro-second ranges, can be delivered in a significantly shorter (~ nanosecond) duration.* It therefore becomes relevant and important to consider the pulse-width aspect and evaluate the underlying “strength-duration (S-D)” curves for various tissue parameters and shapes. Traditionally, the S-D curve plots the threshold voltage (or current) necessary for the onset of an electrically activated bio-response as a function of the pulse duration [138, 139]. The interest, in this context, is to obtain the threshold voltage (or average electric field) required to electroporate at a given pulse duration for a specified distortion factor  $d$  and intra-cellular parameters. The results are highlighted in Figure 5.7 for a homogeneous tissue cluster (similar to those in Figs. 5.6) with 0.275 volume fraction. The fraction is computed as a ratio of proper cells compared to those that are generated in the entire simulation volume. For comparison, the S-D curve for a single cell is also plotted. In the curves of Fig. 5.7, the intra-cellular conductivity and permittivity was chosen to be 0.13 S/m and  $60\epsilon_0$ , respectively, and the membrane permittivity was  $4\epsilon_0$ .

In keeping with general trends of S-D characteristics, a dramatic increase in requisite pulse duration is predicted as the applied electric field magnitudes are lowered. Clearly, with a lower electrical driver, more time is necessary for charging the membranes to their

electroporative threshold. Furthermore, with increasing random orientations of the membrane segments with respect to a given axis (i.e., the applied field direction; for instance), there is a lower probability of reaching the threshold for the collective population. Hence, the threshold field increases with cell irregularity (i.e. the  $d$  parameter).

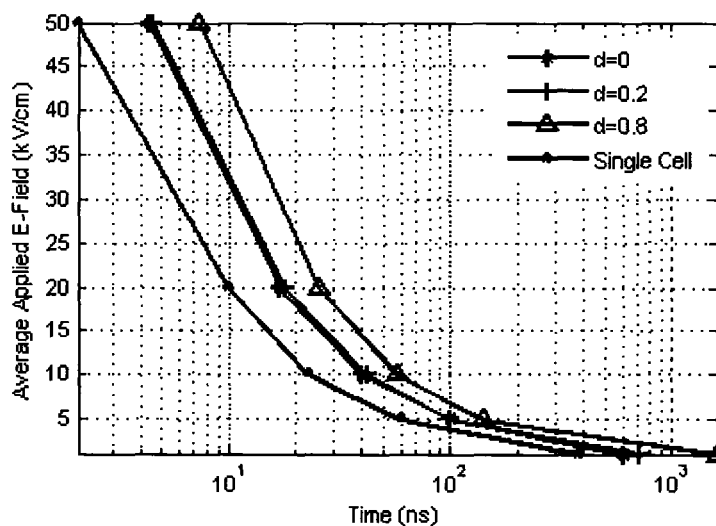


**Fig. 5.6.** S-D curves for cell clusters with various distortion parameters and that for a single spherical cell.

### 5.5.2 Summarizing the cell cluster

It should be mentioned that an extremely brief presentation of the details pertaining to the micro-level simulations, in particular, for cell clusters has been presented here. Nevertheless, the results *do* demonstrate the following aspects.

- First, clusters typically would need larger voltage amplitudes than a single cell, especially for the ultra-short nanosecond regime.
- For a given extra-cellular conductivity parameter, the disparity between single cell and clusters is predicted to increase as the intracellular conductivity reduces.
- A strong selectivity for membrane poration is indicated within heterogeneous tissues. Hence, it should be possible to set the voltage amplitude for chosen pulse duration for preferentially porating only the higher internal conductivity clusters, without any damage to the remaining tissue.
- This selectivity would be stronger within tissues having more irregularly shaped cells.

Section 5.5 and its sub-sections were meant to provide a preview of how the proposed modeling schema of this research contribution could be extended to micro-level systems. It should also be

pointed out that given the similarity of the underlying mathematics involved, these models can be *trivially* extended to utilize distributed computation resources, thus extending the population and diversity of these cell clusters.

## References

- [1] K. H. Schoenbach, R. P. Joshi, J. F. Kolb, N. Chen, M. Stacey, P. F. Blackmore, E. S. Buescher, and S. J. Beebe, "Ultrashort electrical pulses open a new gateway into biological cells," *Proceedings of the IEEE*, vol. 92, pp. 1122-1137, 2004.
- [2] U. Pliquet, R. Elez, A. Piiper, and E. Neumann, "Electroporation of subcutaneous mouse tumors by rectangular and trapezium high voltage pulses," *Bioelectrochemistry*, vol. 62, pp. 83-93, Apr 2004.
- [3] M. P. Rogers, J. H. Merritt, J. C. Comeaux, C. T. JKuhnel Jr., D. F. Moreland, D. G. Teltschik, J. H. Lucas, and M. R. Murphy, "Strength-duration curve for an electrically excitable tissue extended down to near 1 nanosecond," *IEEE Trans Plasma Sci.*, vol. 32, pp. 1587-1599, 2003.
- [4] F. Rattay, "Analysis of models for external stimulation of axons," *IEEE Trans Biomed Eng*, vol. 33, pp. 974-7, Oct 1986.
- [5] F. Rattay, *Electrical Nerve Stimulation: Theory, Experiments and Applications*. New York: Springer-Verlag, 1990.
- [6] B. Frankenhaeuser and A. F. Huxley, "The Action Potential in the Myelinated Nerve Fiber of *Xenopus Laevis* as Computed on the Basis of Voltage Clamp Data," *J Physiol*, vol. 171, pp. 302-15, Jun 1964.
- [7] C. Tai, W. C. de Groat, and J. R. Roppolo, "Simulation of nerve block by high-frequency sinusoidal electrical current based on the Hodgkin-Huxley model," *IEEE Trans Neural Syst Rehabil Eng*, vol. 13, pp. 415-22, Sep 2005.
- [8] C. Tai, W. C. de Groat, and J. R. Roppolo, "Simulation analysis of conduction block in unmyelinated axons induced by high-frequency biphasic electrical currents," *IEEE Trans Biomed Eng*, vol. 52, pp. 1323-32, Jul 2005.
- [9] R. Stampfli, "Reversible electrical breakdown of the excitable membrane of a Ranvier node.," *An. Acad. Brasil. Ciens.*, vol. 30, pp. 57-63, 1958.
- [10] P. H. Veltink, J. A. van Alste, and H. B. Boom, "Simulation of intrafascicular and extraneural nerve stimulation," *IEEE Trans Biomed Eng*, vol. 35, pp. 69-75, Jan 1988.
- [11] N. Bhadra, E. A. Lahowetz, S. T. Foldes, and K. L. Kilgore, "Simulation of high-frequency sinusoidal electrical block of mammalian myelinated axons," *J Comput Neurosci*, Jan 3 2007.
- [12] N. Bhadra and K. L. Kilgore, "Direct current electrical conduction block of peripheral nerve," *IEEE Trans Neural Syst Rehabil Eng*, vol. 12, pp. 313-24, Sep 2004.
- [13] M. Manfredi, "Differential block of conduction of larger fibers in peripheral nerve by direct current," *Arch Ital Biol*, vol. 108, pp. 52-71, Jan 1970.
- [14] A. G. Brown and W. C. Hamann, "DC-polarization and impulse conduction failure in mammalian nerve fibres," *J Physiol*, vol. 222, pp. 66P-67P, Apr 1972.
- [15] A. S. Paintal, "Block of conduction in mammalian myelinated nerve fibres by low temperatures," *J Physiol*, vol. 180, pp. 1-19, Sep 1965.
- [16] S. Schumacher, S. Bross, J. R. Scheepe, C. Seif, K. P. Junemann, and P. Alken, "Extradural cold block for selective neurostimulation of the bladder: development of a new technique," *J Urol*, vol. 161, pp. 950-4, Mar 1999.
- [17] I. A. Chang and U. D. Nguyen, "Thermal modeling of lesion growth with radiofrequency ablation devices," *Biomed Eng Online*, vol. 3, p. 27, Aug 6 2004.
- [18] W. M. Wells and A. C. F. Colchester, *Medical image computing and computer-assisted intervention--MICCAI '98 : first international conference, Cambridge, MA, USA, October 11-13, 1998 : proceedings*. Berlin ; New York: Springer, 1998.

- [19] L. Sontag and D. E. Axelrod, "Evaluation of pathways for progression of heterogeneous breast tumors," *Journal of Theoretical Biology*, vol. 232, pp. 179-189, 2005.
- [20] E. Neumann and K. Rosenheck, "Permeability changes induced by electric impulses in vesicular membranes," *J Membr Biol*, vol. 10, pp. 279-90, Dec 29 1972.
- [21] E. Neumann and J. Bernhardt, "Physical chemistry of excitable biomembranes," *Annu Rev Biochem*, vol. 46, pp. 117-41, 1977.
- [22] I. P. Sugar, W. Forster, and E. Neumann, "Model of cell electrofusion. Membrane electroporation, pore coalescence and percolation," *Biophys Chem*, vol. 26, pp. 321-35, May 9 1987.
- [23] E. Neumann, S. Kakorin, and K. Toensing, "Membrane electroporation and electromechanical deformation of vesicles and cells," *Faraday Discuss*, pp. 111-25; discussion 137-57, 1998.
- [24] K. H. Schoenbach, S. J. Beebe, and E. S. Buescher, "Intracellular effect of ultrashort electrical pulses," *Bioelectromagnetics*, vol. 22, pp. 440-8, Sep 2001.
- [25] S. J. Beebe, P. F. Blackmore, J. White, R. P. Joshi, and K. H. Schoenbach, "Nanosecond pulsed electric fields modulate cell function through intracellular signal transduction mechanisms," *Physiol Meas*, vol. 25, pp. 1077-93, Aug 2004.
- [26] P. T. Vernier, Y. Sun, L. Marcu, S. Salemi, C. M. Craft, and M. A. Gundersen, "Calcium bursts induced by nanosecond electric pulses," *Biochem Biophys Res Commun*, vol. 310, pp. 286-95, Oct 17 2003.
- [27] R. P. Joshi, Q. Hu, R. Aly, K. H. Schoenbach, and H. P. Hjalmarson, "Self-consistent simulations of electroporation dynamics in biological cells subjected to ultrashort electrical pulses," *Phys Rev E Stat Nonlin Soft Matter Phys*, vol. 64, p. 011913, Jul 2001.
- [28] T. Y. Tsong, "Electroporation of cell membranes," *Biophys J*, vol. 60, pp. 297-306, Aug 1991.
- [29] M. Pavlin, T. Slivnik, and D. Miklavcic, "Effective conductivity of cell suspensions," *IEEE Trans Biomed Eng*, vol. 49, pp. 77-80, Jan 2002.
- [30] M. Pavlin, N. Pavselj, and D. Miklavcic, "Dependence of induced transmembrane potential on cell density, arrangement, and cell position inside a cell system," *IEEE Trans Biomed Eng*, vol. 49, pp. 605-12, Jun 2002.
- [31] M. Pavlin, V. Leben, and D. Miklavcic, "Electroporation in dense cell suspension--theoretical and experimental analysis of ion diffusion and cell permeabilization," *Biochim Biophys Acta*, vol. 1770, pp. 12-23, Jan 2007.
- [32] P. J. Bassar and B. J. Roth, "New currents in electrical stimulation of excitable tissues," *Annu Rev Biomed Eng*, vol. 2, pp. 377-97, 2000.
- [33] J. P. Reilly, *Electrical Stimulation and Electropathology*. Cambridge: Cambridge Press, UK, 1992.
- [34] B. J. Roth, "Mechanisms for electrical stimulation of excitable tissue," *Crit Rev Biomed Eng*, vol. 22, pp. 253-305, 1994.
- [35] P. S. Eriksson, E. Perfilieva, T. Bjork-Eriksson, A. M. Alborn, C. Nordborg, D. A. Peterson, and F. H. Gage, "Neurogenesis in the adult human hippocampus," *Nat Med*, vol. 4, pp. 1313-7, Nov 1998.
- [36] E. Gould, A. J. Reeves, M. S. Graziano, and C. G. Gross, "Neurogenesis in the neocortex of adult primates," *Science*, vol. 286, pp. 548-52, Oct 15 1999.
- [37] D. M. Durand, "Electrical Stimulation of Excitable Tissue," in *Biomedical Engineering Handbook*, J. D. Bronzino, Ed. Boca Raton: CRC Press, 1995.
- [38] K. P. Esselle and M. A. Stuchly, "Neural stimulation with magnetic fields: analysis of induced electric fields," *IEEE Trans Biomed Eng*, vol. 39, pp. 693-700, Jul 1992.
- [39] L. Heller and D. B. van Hulsteyn, "Brain stimulation using electromagnetic sources: theoretical aspects," *Biophys J*, vol. 63, pp. 129-38, Jul 1992.

- [40] P. J. Basser and B. J. Roth, "Stimulation of a myelinated nerve axon by electromagnetic induction," *Med Biol Eng Comput*, vol. 29, pp. 261-8, May 1991.
- [41] J. H. Meier, W. L. Rutten, A. E. Zoutman, H. B. Boom, and P. Bergveld, "Simulation of multipolar fiber selective neural stimulation using intrafascicular electrodes," *IEEE Trans Biomed Eng*, vol. 39, pp. 122-34, Feb 1992.
- [42] B. L. Cobb, J. R. Jauchem, P. A. Mason, M. P. Dooley, S. A. Miller, J. M. Ziriaux, and M. R. Murphy, "Neural and behavioral teratological evaluation of rats exposed to ultra-wideband electromagnetic fields," *Bioelectromagnetics*, vol. 21, pp. 524-37, Oct 2000.
- [43] J. R. Jauchem, M. R. Frei, K. L. Ryan, J. H. Merritt, and M. R. Murphy, "Lack of effects on heart rate and blood pressure in ketamine-anesthetized rats briefly exposed to ultra-wideband electromagnetic pulses," *IEEE Trans Biomed Eng*, vol. 46, pp. 117-20, Jan 1999.
- [44] Vijayalaxmi, R. L. Seaman, M. L. Belt, J. M. Doyle, S. P. Mathur, and T. J. Prihoda, "Frequency of micronuclei in the blood and bone marrow cells of mice exposed to ultra-wideband electromagnetic radiation," *Int J Radiat Biol*, vol. 75, pp. 115-20, Jan 1999.
- [45] S. A. Miller, M. E. Bronson, and M. R. Murphy, "Ultrawideband radiation and pentylenetetrazol-induced convulsions in rats," *Bioelectromagnetics*, vol. 20, pp. 327-9, 1999.
- [46] R. P. Joshi, F. Chen, and W. R. Rogers, "Modeling Electrode-Based Stimulation of Muscle and Nerve by Ultra-Short Electric Pulses," *IEEE Trans Plasma Sci.*, vol. 32, pp. 1687-1695, 2004.
- [47] R. P. Joshi, Q. Hu, and K. Schoenbach, "Modeling Studies of Cell Response to Ultrashort, High-Intensity Electric Fields – Implications for Intracellular Manipulation," *IEEE Trans Plasma Sci.*, vol. 32, pp. 1677-1686, 2004.
- [48] K. H. Schoenbach, F. E. Peterkin, R. W. Alden, III, and S. J. Beebe, "The effect of pulsed electric fields on biological cells: experiments and applications," *IEEE Trans. Plasma Sci.*, vol. 25, pp. 284-292, 1997.
- [49] E. Murray, "OKC police release video in Taser death case," in *The Wichita Eagle*, 2007.
- [50] D. B. Dunson, C. Holloman, C. Calder, and L. H. Gunn, "Bayesian modeling of multiple lesion onset and growth from interval-censored data," *Biometrics*, vol. 60, pp. 676-83, Sep 2004.
- [51] S. Pissanetzky, *Sparse Matrix Technology*. Orlando, FL: Academic Press Inc., 1984.
- [52] A. George, J. W. H. Liu, and E. Ng, "Communication results for parallel sparse Cholesky factorization on a hypercube," *Parallel Computing*, vol. 10, pp. 287-298, 1989.
- [53] T. Imamura, "An estimation of complexity and computational costs for vertical block-cyclic distributed parallel LU factorization," *The Journal of Supercomputing*, vol. 15, pp. 95-110, 2000.
- [54] D. Kaya and K. Wright, "Parallel algorithms for LU decomposition on a shared memory multiprocessor," *Applied Mathematics and Computation*, vol. 163, pp. 179-192, 2005.
- [55] J. M. Conroy, S. G. Kratzer, R. F. Lucas, and A. E. Aaron, "Parallel sparse LU factorization," *SIAM Journal on Scientific Computing*, vol. 19, pp. 584-604, 1998.
- [56] K. Shen, T. Yang, and X. Jiao, "Efficient 2D sparse LU factorization on parallel machines," *SIAM Journal on Matrix Analysis and Applications*, vol. 22, pp. 282-305, 2001.
- [57] M. Hahad, "A parallel sparse LU Decomposition with Application to Semiconductor Device Simulation," *Lecture Notes in Computer Science*, vol. 1300, pp. 848-872, 1997.
- [58] P. Chen, H. Runesha, D. T. Nguyen, P. Tong, and T. Y. P. Chang, "Sparse algorithms for indefinite system of linear equations," *Computational Mechanics*, vol. 25, pp. 33-42, 2000.



- [59] D. R. McNeal, "Analysis of a model for excitation of myelinated nerve," *IEEE Trans Biomed Eng*, vol. 23, pp. 329-37, Jul 1976.
- [60] N. A. Carlson, *Foundations of Physiological Psychology*. Needham Heights, MA.: Simon & Schuster, 1992.
- [61] R. Fitzhugh, "Computation of impulse initiation and saltatory conduction in a myelinated nerve fiber," *Biophys J*, vol. 2, pp. 11-21, Jan 1962.
- [62] A. L. Hodgkin and A. F. Huxley, "A quantitative description of membrane current and its application to conduction and excitation in nerve," *J Physiol*, vol. 117, pp. 500-544, Aug 1952.
- [63] A. L. Hodgkin and A. F. Huxley, "A quantitative description of membrane current and its application to conduction and excitation in nerve," *J Physiol*, vol. 117, pp. 500-44, Aug 1952.
- [64] J. P. Reilly, V. T. Freeman, and W. D. Larkin, "Sensory effects of transient electrical stimulation--evaluation with a neuroelectric model," *IEEE Trans Biomed Eng*, vol. 32, pp. 1001-11, Dec 1985.
- [65] F. Rattay, "High frequency electrostimulation of excitable cells," *J Theor Biol*, vol. 123, pp. 45-54, Nov 7 1986.
- [66] K. W. Altman and R. Plonsey, "Point source nerve bundle stimulation: effects of fiber diameter and depth on simulated excitation," *IEEE Trans Biomed Eng*, vol. 37, pp. 688-98, Jul 1990.
- [67] M. J. Gutnick and W. E. Crill, *The Cortical Neuron as an electrophysiological unit*. New York: Oxford University Press, 1995.
- [68] G. M. Shepherd, *The synaptic organization of the brain*, 4th ed. New York: Oxford University Press, 1998.
- [69] H. R. Wilson, "Simplified dynamics of human and mammalian neocortical neurons," *J Theor Biol*, vol. 200, pp. 375-88, Oct 21 1999.
- [70] D. Takeshita, Y. D. Sato, and S. Bahar, "Transitions between multistable states as a model of epileptic seizure dynamics," *Phys Rev E*, vol. 75, pp. 051925-1 2007.
- [71] J. W. Moore, R. W. Joyner, M. H. Brill, S. D. Waxman, and M. Najjar-Joa, "Simulations of conduction in uniform myelinated fibers. Relative sensitivity to changes in nodal and internodal parameters," *Biophys J*, vol. 21, pp. 147-60, Feb 1978.
- [72] R. J. MacGregor and R. M. Oliver, "A model for repetitive firing in neurons," *Kybernetik*, vol. 16, pp. 53-64, 1974.
- [73] M. Huss, A. Lansner, P. Wallen, A. El Manira, S. Grillner, and J. H. Kotaleski, "Roles of ionic currents in lamprey CpG neurons: a modeling study," *J Neurophysiol*, vol. 97, pp. 2696-711, Apr 2007.
- [74] J. H. Caldwell, K. L. Schaller, R. S. Lasher, E. Peles, and S. R. Levinson, "Sodium channel Na(v)1.6 is localized at nodes of ranvier, dendrites, and synapses," *Proc Natl Acad Sci U S A*, vol. 97, pp. 5616-20, May 9 2000.
- [75] W. F. Agnew and D. B. McCreery, *Neural Prosthesis: Fundamental Studies*. Englewood Cliffs: Prentice Hall, 1990.
- [76] J. C. Petruska, C. H. Hubscher, and R. D. Johnson, "Anodally focused polarization of peripheral nerve allows discrimination of myelinated and unmyelinated fiber input to brainstem nuclei," *Exp Brain Res*, vol. 121, pp. 379-90, Aug 1998.
- [77] J. G. Whitwam and C. Kidd, "The use of direct current to cause selective block of large fibres in peripheral nerves," *Br J Anaesth*, vol. 47, pp. 1123-33, Nov 1975.
- [78] M. Cattell and R. W. Gerard, "The "inhibitory" effect of high-frequency stimulation and the excitation state of nerve," *J Physiol*, vol. 83, pp. 407-15, Mar 15 1935.
- [79] S. W. Kuffler and R. W. Gerard, "The small-nerve motor system to skeletal muscle," *J Neurophysiol.*, vol. 10, pp. 383-394, 1947.

- [80] M. Ishigooka, T. Hashimoto, I. Sasagawa, K. Izumiya, and T. Nakada, "Modulation of the urethral pressure by high-frequency block stimulus in dogs," *Eur Urol*, vol. 25, pp. 334-7, 1994.
- [81] S. J. Tsai, H. L. Lew, E. Date, and L. I. Bih, "Treatment of detrusor-sphincter dyssynergia by pudendal nerve block in patients with spinal cord injury," *Arch Phys Med Rehabil*, vol. 83, pp. 714-7, May 2002.
- [82] R. Baratta, M. Ichie, S. K. Hwang, and M. Solomonow, "Orderly stimulation of skeletal muscle motor units with tripolar nerve cuff electrode," *IEEE Trans Biomed Eng*, vol. 36, pp. 836-43, Aug 1989.
- [83] Z. P. Fang and J. T. Mortimer, "A method to effect physiological recruitment order in electrically activated muscle," *IEEE Trans Biomed Eng*, vol. 38, pp. 175-9, Feb 1991.
- [84] N. Accornero, G. Bini, G. L. Lenzi, and M. Manfredi, "Selective Activation of peripheral nerve fibre groups of different diameter by triangular shaped stimulus pulses," *J Physiol*, vol. 273, pp. 539-60, Dec 1977.
- [85] R. P. Joshi, Q. Hu, K. H. Schoenbach, and H. P. Hjalmarson, "Improved energy model for membrane electroporation in biological cells subjected to electrical pulses," *Phys Rev E Stat Nonlin Soft Matter Phys*, vol. 65, p. 041920, Apr 2002.
- [86] A. J. H. Sale and W. A. Hamilton, "Effects of high electric fields on micro-organisms: I. Killing of bacteria and yeast.  
Effects of high electric fields on microorganisms : II. Mechanism of action of the lethal effect.," *Biochimica et Biophysica Acta.*, vol. 148, pp. 781-800, 1967.
- [87] K. Schoenbach, R. P. Joshi, R. H. Stark, F. C. Dobbs, and S. J. Beebe, "Bacterial decontamination of liquids with pulsed electric fields," *IEEE Trans. Dielectrics & Electrical Insulation*, vol. 7, pp. 637-645, 2000.
- [88] R. Nuccitelli, U. Pliquett, X. Chen, W. Ford, R. James Swanson, S. J. Beebe, J. F. Kolb, and K. H. Schoenbach, "Nanosecond pulsed electric fields cause melanomas to self-destruct," *Biochem Biophys Res Commun*, vol. 343, pp. 351-60, May 5 2006.
- [89] M. Stacey, J. Stickleby, P. Fox, V. Statler, K. Schoenbach, S. J. Beebe, and S. Buescher, "Differential effects in cells exposed to ultra-short, high intensity electric fields: cell survival, DNA damage, and cell cycle analysis," *Mutat Res*, vol. 542, pp. 65-75, Dec 9 2003.
- [90] R. Nuccitelli, "Endogenous electric fields in embryos during development, regeneration and wound healing," *Radiat Prot Dosimetry*, vol. 106, pp. 375-83, 2003.
- [91] M. Zhao, B. Song, J. Pu, T. Wada, B. Reid, G. Tai, F. Wang, A. Guo, P. Walczysko, Y. Gu, T. Sasaki, A. Suzuki, J. V. Forrester, H. R. Bourne, P. N. Devreotes, C. D. McCaig, and J. M. Penninger, "Electrical signals control wound healing through phosphatidylinositol-3-OH kinase-gamma and PTEN," *Nature*, vol. 442, pp. 457-60, Jul 27 2006.
- [92] Z. Vasilkoski, A. T. Esser, T. R. Gowrishankar, and J. C. Weaver, "Membrane electroporation: The absolute rate equation and nanosecond time scale pore creation," *Phys Rev E Stat Nonlin Soft Matter Phys*, vol. 74, p. 021904, Aug 2006.
- [93] J. C. Neu and W. Krassowska, "Modeling postshock evolution of large electropores," *Phys Rev E Stat Nonlin Soft Matter Phys*, vol. 67, p. 021915, Feb 2003.
- [94] R. P. Joshi, Q. Hu, and K. Schoenbach, "Dynamical Modeling of Cellular Response to Short-Duration, High-Intensity Electric Fields," *IEEE Trans. Dielectrics & Electrical Insulation*, vol. 10, pp. 778-787, 2003.
- [95] Q. Hu, R. P. Joshi, and K. H. Schoenbach, "Simulations of nanopore formation and phosphatidylserine externalization in lipid membranes subjected to a high-intensity, ultrashort electric pulse," *Phys Rev E Stat Nonlin Soft Matter Phys*, vol. 72, p. 031902, Sep 2005.

- [96] Q. Hu, S. Viswanadham, R. P. Joshi, K. H. Schoenbach, S. J. Beebe, and P. F. Blackmore, "Simulations of transient membrane behavior in cells subjected to a high-intensity ultrashort electric pulse," *Phys Rev E Stat Nonlin Soft Matter Phys*, vol. 71, p. 031914, Mar 2005.
- [97] D. P. Tieleman, H. Leontiadou, A. E. Mark, and S. J. Marrink, "Simulation of pore formation in lipid bilayers by mechanical stress and electric fields," *J Am Chem Soc*, vol. 125, pp. 6382-3, May 28 2003.
- [98] G. Guidotti, "Membrane proteins," *Annu Rev Biochem*, vol. 41, pp. 731-52, 1972.
- [99] E. Neumann, M. Schaefer-Ridder, Y. Wang, and P. H. Hofschneider, "Gene transfer into mouse lyoma cells by electroporation in high electric fields," *Embo J*, vol. 1, pp. 841-5, 1982.
- [100] D. P. Tieleman, "The molecular basis of electroporation," *BMC Biochem*, vol. 5, p. 10, Jul 19 2004.
- [101] L. Monticelli, K. M. Robertson, J. L. MacCallum, and D. P. Tieleman, "Computer simulation of the KvAP voltage-gated potassium channel: steered molecular dynamics of the voltage sensor," *FEBS Lett*, vol. 564, pp. 325-32, Apr 30 2004.
- [102] K. Ohuchi, Y. Fukui, I. Sakuma, N. Shibata, H. Honjo, and I. Kodama, "A dynamic action potential model analysis of shock-induced aftereffects in ventricular muscle by reversible breakdown of cell membrane," *IEEE Trans Biomed Eng*, vol. 49, pp. 18-30, Jan 2002.
- [103] Y. Suemitsu and S. Nara, "A solution for two-dimensional mazes with use of chaotic dynamics in a recurrent neural network model," *Neural Comput*, vol. 16, pp. 1943-57, Sep 2004.
- [104] M. E. Brandt and C. Guanrong, "Feedback control of pathological rhythms in two models of cardiac activity," 1997, pp. 219-223 vol.2.
- [105] G. Karypsis and V. Kumar, "METIS - A Software Package for Partitioning Unstructured Graphs, Partitioning Meshes, and Computing Fill-Reducing Orderings of Sparse Matrices.," Minneapolis, MN, 1998.
- [106] X. S. Li and J. W. Demmel, "SuperLU-DIST: A scalable distributed memory sparse direct solver for unsymmetric linear systems," *ACM Trans. on Mathematical Software*, vol. 29, pp. 110-140, 2003.
- [107] J. W. Cooley and F. A. Dodge, Jr., "Digital computer solutions for excitation and propagation of the nerve impulse," *Biophys J*, vol. 6, pp. 583-99, Sep 1966.
- [108] J. C. Weaver, "Electroporation theory. Concepts and mechanisms," *Methods Mol Biol*, vol. 55, pp. 3-28, 1995.
- [109] J. C. Weaver, "Molecular basis for cell membrane electroporation," *Ann N Y Acad Sci*, vol. 720, pp. 141-52, May 31 1994.
- [110] V. F. Pastushenko and A. Chizmadzhev Iu, "[Theory of electric clamp of lipid bilayer membranes. Splitting of the energy barrier]," *Biofizika*, vol. 27, pp. 475-9, May-Jun 1982.
- [111] V. F. Pastushenko and A. Chizmadzhiev Iu, "[Electric breakdown of lipid vesicles]," *Biofizika*, vol. 28, pp. 1036-9, Nov-Dec 1983.
- [112] A. Barnett, "The current-voltage relation of an aqueous pore in a lipid bilayer membrane," *Biochim Biophys Acta*, vol. 1025, pp. 10-4, Jun 11 1990.
- [113] S. A. Freeman, M. A. Wang, and J. C. Weaver, "Theory of electroporation of planar bilayer membranes: predictions of the aqueous area, change in capacitance, and pore-pore separation," *Biophys J*, vol. 67, pp. 42-56, Jul 1994.
- [114] M. Winterhalter and W. Helfrich, "Effect of voltage on pores in membranes," *Physical Review A*, vol. 36, pp. 5874-5876, Dec 15 1987.
- [115] E. Neumann, A. E. Sowers, and C. A. Jordan, *Electroporation and electrofusion in cell biology*. New York: Plenum Press, 1989.

- [116] J. T. Rubinstein, "Threshold fluctuations in an N sodium channel model of the node of Ranvier," *Biophys J*, vol. 68, pp. 779-85, Mar 1995.
- [117] R. W. Glaser, S. L. Leikin, L. V. Chernomordik, V. F. Pastushenko, and A. I. Sokirko, "Reversible electrical breakdown of lipid bilayers: formation and evolution of pores," *Biochim Biophys Acta*, vol. 940, pp. 275-87, May 24 1988.
- [118] L. V. Chernomordik, S. I. Sukharev, S. V. Popov, V. F. Pastushenko, A. V. Sokirko, I. G. Abidor, and Y. A. Chizmadzhev, "The electrical breakdown of cell and lipid membranes: the similarity of phenomenologies," *Biochim Biophys Acta*, vol. 902, pp. 360-73, Sep 3 1987.
- [119] J. E. Hall, "Access resistance of a small circular pore," *J Gen Physiol*, vol. 66, pp. 531-2, Oct 1975.
- [120] B. Hille, "Pharmacological modifications of the sodium channels of frog nerve," *J Gen Physiol*, vol. 51, pp. 199-219, Feb 1968.
- [121] G. Karypis and V. Kumar, "A Software Package for Partitioning Unstructured Graphs, Partitioning Meshes, and Computing Fill-Reducing Orderings of Sparse Matrices," University of Minnesota/Army HPC Centre, Minneapolis, MN, 1998.
- [122] P. R. Amestoy, I. S. Duff, and J.-Y. L'Excellent, "Multifrontal parallel distributed symmetric and unsymmetric solvers.," *Computational Methods in Applied Mechanical Engineering.*, vol. 184, pp. 501-520, 2000.
- [123] C. B. Muratov, "A quantitative approximation scheme for the traveling wave solutions in the Hodgkin-Huxley model," *Biophys J*, vol. 79, pp. 2893-901, Dec 2000.
- [124] A. G. Pakhomov, J. F. Kolb, R. P. Joshi, K. H. Schoenbach, T. Dayton, J. C. Comeaux, J. Ashmore, and C. Beason, "Neuromuscular disruption with ultrashort electrical pulses," *Proceedings of SPIE - The International Society for Optical Engineering*, vol. 6219, pp. 621903-621910, 2006.
- [125] D. T. Edmonds, "A physical model of sodium channel gating," *Eur Biophys J*, vol. 14, pp. 195-201, 1987.
- [126] D. T. Edmonds, "Electrostatic models for ion channels and pumps," *Biochem Soc Symp*, vol. 50, pp. 1-10, 1985.
- [127] A. Mishra, R. P. Joshi, K. H. Schoenbach, and C. D. Clarke III, "Parallelized Computational Approach Based on Sparse LU Factorization for Predictions of Spatial and Time-Dependent Currents and Voltages in Full-Body Bio-Models," *IEEE Trans Plasma Sci.*, vol. 34, pp. 1431-1440, 2006.
- [128] R. P. Joshi, A. Mishra, Q. Hu, K. H. Schoenbach, and A. G. Pakhomov, "Self-consistent analyses for potential conduction block in nerves by an ultrashort high-intensity electric pulse," *Phys Rev E*, vol. 75, pp. 061906-17, June, 2007 2007.
- [129] D. T. Edmonds, "The alpha-helix dipole in membranes: a new gating mechanism for ion channels," *Eur Biophys J*, vol. 13, pp. 31-5, 1985.
- [130] C. M. Armstrong, "Sodium channels and gating currents," *Physiol Rev*, vol. 61, pp. 644-83, Jul 1981.
- [131] R. P. Joshi, Q. Hu, and K. H. Schoenbach, "Dynamical modeling of cellular response to short-duration, high-intensity electric fields.," *IEEE Trans Dielectrics and Electrical Insulation*, vol. 10, pp. 778- 787, 2003.
- [132] J. A. George and W. H. Liu, *Computer Solution of Large Sparse Positive Definite Systems*. Englewood Cliffs, NJ: Prentice-Hall, USA, 1981.
- [133] M. Pavlin, M. Kanduser, M. Rebersek, G. Pucihar, F. X. Hart, R. Magjarevic, and D. Miklavcic, "Effect of cell electroporation on the conductivity of a cell suspension," *Biophys J*, vol. 88, pp. 4378-90, Jun 2005.
- [134] D. Weaire and N. Rivier, "Soap, cells and statistics – random patterns in two-dimensions," *Contemp. Phys.*, vol. 25, pp. 59-99, 1984.

- [135] K. C. Smith, T. R. Gowrishankar, A. T. Esser, D. A. Stewart, and J. C. Weaver, "The spatially distributed transmembrane voltage of cells and organelles due to 10-ns pulses: meshed transport networks.," *IEEE Trans Plasma Sci.*, vol. 34, pp. 1394-1404, 2006.
- [136] D. P. Tieleman, "Computer simulations of transport through membranes: passive diffusion, pores, channels and transporters," *Clin Exp Pharmacol Physiol*, vol. 33, pp. 893-903, Oct 2006.
- [137] K. H. Schoenbach, R. P. Joshi, R. H. Stark, F. C. Dobbs, and S. J. Beebe, "Bacterial decontamination of liquids with pulsed electric fields " *IEEE Trans Dielectrics and Electrical Insulation*, vol. 7, pp. 637-645, 2000.
- [138] H. A. Blair, "On the intensity-time relations for stimulation by electric currents, I.," *J. Gen. Physiol.*, vol. 15, pp. 709-721, 1932.
- [139] H. A. Blair, "On the intensity-time relations for stimulation by electric currents, II," *J. Gen. Physiol.*, vol. 15, pp. 731-755, 1932.

## Appendix

### A.1 Converting index to Coordinates:

While dealing with binary data files, it is necessary to understand which coordinate a particular entry listed serially in the binary format corresponds to. Towards that end, the following subroutine was written to perform the conversion. Given:

---

```

Total Nodes in X Dimension = Xnodes
Total Nodes in Y Dimension = Ynodes
Total Nodes in Z Dimension = Znodes
Index of Current entry in file = IND

IF IND > XNODES*YNODES
{
    IF MODULUS (IND, XNODES*ZNODES) = 0
        {
            Y← IND/XNODES/ZNODES
        }
    ELSE
        {
            Y← IND/XNODES/ZNODES +1
        }
}
ELSE
{
    Y←1
}

TEMP← IND-(XNODES*ZNODES)*(Y-1)
IF MODULUS (TEMP, XNODES) =0
{
    X←XNODES
    Z←TEMP/XNODES
}
ELSE
{
    X←MODULUS (TEMP, XNODES)
    Z←FIX (TEMP/XNODES) +1
}

```

---

It should also be noted that this a coordinate for a given index will also depend upon the scanning schema used. For example, in this particular research, all raw files used, were scanned X-Z-Y format. That means, first along X, then along Z; then once the entire first X-Z plane (at Y=1) was scanned, the next X-Z slice at Y=2 was scanned.

## A.2 Symmetric modeling scheme:

In section 3.1.2 the modeling details employing the intrinsic asymmetric nature of the coefficient matrix were detailed. The system can be converted to a symmetric one and would yield faster performance. However, it could not be deployed at the clusters here, due to lack of appropriate solver routines on all the nodes. Nevertheless, the pertinent equations are provided here for completeness. Figure 3.4 from chapter 3 is again presented here.

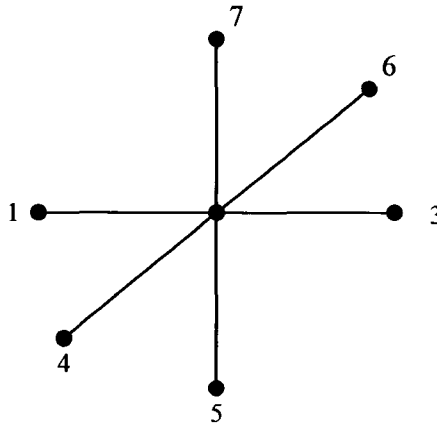


**Figure A.1:** Simplified schematic to highlight the nodal links and node indexing.

Assuming that node 2 is of current interest and that node 1 is an anode location, while node 6 is a cathode. The initial set of equations is given by (using equation 3.1.5 as the starting point):

$$\begin{aligned}
 & V_2^n \left[ \sum_i \left( \frac{C_{2i}}{\Delta t} + \frac{1}{2R_{2i}} \right) \right] - V_1^n \left[ \frac{C_{21}}{\Delta t} + \frac{1}{2R_{21}} \right] - V_3^n \left[ \frac{C_{23}}{\Delta t} + \frac{1}{2R_{23}} \right] - \dots \\
 & V_4^n \left[ \frac{C_{24}}{\Delta t} + \frac{1}{2R_{24}} \right] - V_5^n \left[ \frac{C_{25}}{\Delta t} + \frac{1}{2R_{25}} \right] - V_6^n \left[ \frac{C_{26}}{\Delta t} + \frac{1}{2R_{26}} \right] - V_7^n \left[ \frac{C_{27}}{\Delta t} + \frac{1}{2R_{27}} \right] = \\
 & (V_1^o - V_2^o) \left[ \frac{1}{2R_{21}} - \frac{C_{21}}{\Delta t} \right] + (V_3^o - V_2^o) \left[ \frac{1}{2R_{23}} - \frac{C_{23}}{\Delta t} \right] + (V_4^o - V_2^o) \left[ \frac{1}{2R_{24}} - \frac{C_{24}}{\Delta t} \right] + \dots \\
 & (V_5^o - V_2^o) \left[ \frac{1}{2R_{25}} - \frac{C_{25}}{\Delta t} \right] + (V_6^o - V_2^o) \left[ \frac{1}{2R_{26}} - \frac{C_{26}}{\Delta t} \right] + (V_7^o - V_2^o) \left[ \frac{1}{2R_{27}} - \frac{C_{27}}{\Delta t} \right]
 \end{aligned} \tag{A.1}$$

$$\begin{aligned}
k_1 &= \left[ \frac{C_{21}}{\Delta t} + \frac{1}{2R_{21}} \right]; k_3 = \left[ \frac{C_{23}}{\Delta t} + \frac{1}{2R_{23}} \right]; \\
k_4 &= \left[ \frac{C_{24}}{\Delta t} + \frac{1}{2R_{24}} \right]; k_5 = \left[ \frac{C_{25}}{\Delta t} + \frac{1}{2R_{25}} \right]; \\
k_6 &= \left[ \frac{C_{26}}{\Delta t} + \frac{1}{2R_{26}} \right]; k_7 = \left[ \frac{C_{27}}{\Delta t} + \frac{1}{2R_{27}} \right]
\end{aligned}$$

and the following for those on the right hand side( RHS):

$$\begin{aligned}
m_1 &= \left[ \frac{1}{2R_{21}} - \frac{C_{21}}{\Delta t} \right]; m_3 = \left[ \frac{1}{2R_{23}} - \frac{C_{23}}{\Delta t} \right]; \\
m_4 &= \left[ \frac{1}{2R_{24}} - \frac{C_{24}}{\Delta t} \right]; m_5 = \left[ \frac{1}{2R_{25}} - \frac{C_{25}}{\Delta t} \right]; \\
m_6 &= \left[ \frac{1}{2R_{26}} - \frac{C_{26}}{\Delta t} \right]; m_7 = \left[ \frac{1}{2R_{27}} - \frac{C_{27}}{\Delta t} \right].
\end{aligned}$$

Since  $V_1^n$  is known, and  $V_6^n = V_6^o = 0$ ; Equation (A.1) can then be recast in the following form:

$$\begin{aligned}
&V_2^n [k_3 + k_4 + k_5 + k_7] - \dots \\
&V_3^n k_3 - V_4^n k_4 - V_5^n k_5 - V_7^n k_7 = \\
&V_1^o m_1 + V_3^o m_3 + V_4^o m_4 + V_4^o m_4 + V_5^o m_5 + V_7^o m_7 - \dots \\
&V_2^o [m_1 + m_3 + m_4 + m_5 - m_6 + m_7] + V_1^n k_1
\end{aligned} \tag{A.2}$$

The basic reason why the coefficient matrix is not symmetric is because if there are a total of  $E$  electrode points, it now has a dimension of  $P \times P$ , where:

$$P = (nx \times ny \times nz) - E \tag{A.3}$$

i.e. the potentials are not computed for any node that is connected to an electrode. What this implies is that the node numbering changes for the calculation purposes but, not at the time of writing the result of each iteration to the result file. Needless to say, the bookkeeping involved also increases significantly.



### A.3 Sparse Matrix Storage (Compressed Row Format)

In the development process of this algorithm there is a need for storing the coefficient matrix, which is extremely sparse. Towards that end, the compressed row storage (CSR) format is employed, which apart from being a transpose of the Compressed Column format (as will become evident later), it is also required for the SuperLU solve routines. Here an example of CRS format is presented. Consider the following asymmetric matrix:

$$\begin{bmatrix} 10 & 0 & 0 & 0 & -2 & 0 \\ 9 & 4 & 0 & 0 & 0 & 1 \\ 0 & 0 & 1 & 0 & 5 & 0 \\ 3 & 0 & 0 & 4 & 0 & 1 \\ 0 & 11 & 0 & 0 & 7 & 0 \\ 0 & 0 & 0 & 0 & 8 & 3 \end{bmatrix}$$

To represent this matrix in CRS format there are three vectors required. They are:

1. Row Pointer (ROW\_PTR)
  - ROW\_PTR stores the starting element number for each row. ROW\_PTR(1) is always equal to 1. Consequently, ROW\_PTR(i+1)-ROW\_PTR(i) = Number of elements in row  $i$ . Also, ROW\_PTR(N+1) - ROW\_PTR(1) = Total number of non zero elements in the matrix. This also leads to the fact that ROW\_PTR has a dimension of (N+1\*1) where N is the number of rows in the original matrix.
2. Column Index (COL\_IND)
  - COL\_IND stores the column number of each element as they are transversed row-wise.
3. Value (VAL)
  - VAL contains the actual real (floating point entry at the given location of the matrix).

Based on all of this the above matrix can be completely expressed by:

$$\text{ROW\_PTR} = [1, 3, 6, 8, 11, 13, 15]$$

$$\text{COL\_IND} = [1, 5, 1, 2, 6, 3, 5, 1, 4, 6, 2, 5, 5, 6]$$

$$\text{VAL} = [10, -2, 9, 4, 1, 1, 5, 3, 4, 1, 11, 7, 8, 3]$$

It should be noted that the CRS format for a matrix  $\mathbf{A}$  is the same as Compressed Column Storage (CCS) of  $\mathbf{A}^T$ . Also, to note is that typically while building up the coefficient

matrix, COL\_IND and VAL might not be ordered. What that means is that column entries for a given row might not be in ascending order. However, before any solver routine accepts these vectors, these values need to be sorted. ROW\_PTR does not need to be altered as it only indicates the *number* of entries present in a given row. Anyway, to order a sparse matrix in the CRS format, two successive calls to a transpose subroutine that operates on sparse matrices, will achieve this task.

#### A.4 The Coefficient Matrix in Compressed Row Format

Since the setup of the coefficient matrix is the most important part, the pseudo-code of the process as implemented for the full body modeling scheme is presented here. It is assumed that PELE and GELE are vectors that contain the anode and cathode indices (nodes). Also assumed is that all the vectors have been initialized. The pseudo-code is a very close derivative of the FORTRAN90 code actually used (i.e. contains explanations where deemed necessary).

```
Initialize: ISRCOUNT →1, ICOLCOUNT→1; IROW →0
ISR (ISRCOUNT)←1;
ISRCOUNT →ISRCOUNT+1
```

```
Do WHILE (INDEX < TOTALNODES)
```

```
{
  If (INDEX present in PELE or GELE)
  {
    ISR (ISRCOUNT)←ISR(ISRCOUNT-1)+1
    ISRCOUNT←ISRCOUNT+1
    ICOL (ICOLCOUNT) ← INDEX
    VAL (ICOLCOUNT)← 1.0
    ICOLCOUNT←ICOLCOUNT+1
    SET IROW← 1
  }
  If (IROW = 0)
  {
    [x, y, z] ← GET COORDINATES (INDEX)
    [NBR]←GET NEIGHBORS (x, y, z)

    ISR(ISRCOUNT)=ISR(ISRCOUNT-1) + NUMBER_OF_NEIGHBORS +1
    ISRCOUNT←ISRCOUNT+1

    DO WHILE (INDEX2 < NUMBER_OF_NEIGHBORS
    TEMP←0; SIGMA←0; EPSILON←0
    {
      SIGMA ←(SIGMA [NBR (INDEX2)] + SIGMA [INDEX]) * 0.5
      EPSILON ←(SIGMA [NBR (INDEX2)] + SIGMA [INDEX])*0.5
      VAL (ICOLCOUNT)←EPSILON+(dt/2.0 * SIGMA)
```

```

        ICOL (ICOLCOUNT)←NBR(INDEX2)
        ICOLCOUNT←ICOLCOUNT+1
        TEMP←TEMP – EPSILON – (dt/2.0 * SIGMA)
    }
    ICOL (ICOLCOUNT)←INDEX
    VAL (ICOLCOUNT)←TEMP
    ICOLCOUNT←ICOLCOUNT+1
}
}

```

Looking at the above pseudo-code, it can be seen that the ICOL and VAL will be un-ordered due to the fact that the electrode locations are parsed first, and then the regular (non electrode nodes). It should also be mentioned that since it is not possible to determine how many non zero entries will appear (since they are dependent on the number of electrode locations), ICOL and VAL are initially initialized to a size of 7\*TOTALNODES (as the structure of the coefficient matrix reveals a hepta-diagonal structure).

After the above setup is completed, ICOL and VAL are resized to the correct size, which equals: ISR (LASTVALUE) – 1.

## CURRICULUM VITA

**Ashutosh Mishra**6114, Granby St., Norfolk, VA 23505  
(757)515-4804  
[ashutosh.mishra@gmail.com](mailto:ashutosh.mishra@gmail.com)

## EDUCATION

Old Dominion University, Norfolk, VA**PhD, Electrical & Computer Engineering****2003-2007**

Dissertation: "Development Of Fast, Distributed Computational Schemes For Full Body Bio-Models And Their Application To Novel Action Potential Block In Nerves Using Ultra-Short, High Intensity Electric Pulses".

Old Dominion University, Norfolk, VA**MS, Electrical & Computer Engineering****2001-2003**

Thesis: "Automatic Speaker Identification using Reusable and Re-trainable Binary Pair Partitioned Neural Networks"

Mangalore University, KA, India**B.E. Electrical & Electronics Engineering****1995-1999**Major: Electrical Engineering; *Elective*: Bio-medical Devices

## AWARDS (1999 ~ present)

- **Outstanding Graduate Teaching award** (Dept. of Electrical & Computer Engineering) **2007**
- **Outstanding Graduate Instruction award** (College of Engineering & Technology) **2006**
- **Outstanding Graduate Instruction award** (College of Engineering & Technology) **2003**
- **Best Project Design – Senior Year** (adopted as an instructional tool by the department). **1999**

## TEACHING EXPERIENCE

Old Dominion University, Norfolk, VA**Graduate Instructor – "New PAGE"** (Freshman course on Environmental Aspects).**2004-2006**

- Part of a University level team that developed the course, instructed and evaluated the responses of over 2200 students.
- Developed the backup grade-reporting system for all the instructors involved.

**Graduate Instructor – Electronic Circuits** (Dept. of ECE).**2001-2004**H.B Technological Institute, Kanpur, India**Visiting Faculty (Dept. of Electrical Engineering)****1999-2001**

- Instructed two junior Level and one Final Year courses in Electrical Machines, Electrical Engineering Lab and Fundamentals of Electrical Engineering.

## RELATED EXPERIENCE

LML-Vespa Ltd., Kanpur, India**Sr. Engineer (R&D)**

- Developed the **first** (pre-fabrication) simulator for design and testing of A.C alternators for a range of vehicles manufactured.
- Led a 50 member team and developed the **first, in-house**, linear deflection tachometer for range of 100~11500 RPM and the digital instrument panel.

**1999-2001**

## PUBLICATIONS AND PRESENTATIONS

### Journal Publications

- “Model Assessment of Cell Membrane Breakdown in Clusters and Tissues under High-Intensity Electric Pulsing” (accepted for publication, IEEE Trans. on Plasma Sciences – special issue Aug. 2008)
- “Simulation Studies of Ultra-Short, High-Intensity Electric Pulse Induced Action Potential Block in Whole-Animal Nerve Segments”, (Accepted for publication, Oct. 2007 in IEEE Trans. On Biomedical Engineering), Vol. 55, No. 4, 2008.
- “Self-Consistent Analyses for Potential Conduction Block in Nerves by an Ultra-Short, High-Intensity Electric Pulse”, Physical Review (E), Vol. 75, 061906, June, 2007.
- “A Fast, Parallelized Computational Approach Based on Sparse LU Factorization for Predictions of Spatial and Time-Dependent Currents and Voltages in Full-Body Bio-Models” (*Invited Paper*), IEEE Trans. on Plasma Sc., Vol. 34, 1431-1440, 2006.
- “*Simulations of Distributed Voltages in Full-Body Bio-Models Using Symmetric Factorization with Massively Parallel Solvers in Response to External Pulsing*”, - in review, stage2, IEEE Trans. on Plasma Sciences.

### Conference and Poster presentations

- “Self Consistent Analyses for Potential Conduction Block in Nerves by Ultra Short, High Intensity Pulses”, PPS 2007, June 17~21, Albuquerque, NM.
- “Status of Field Marshal Project”, IVEC, May 2007, Kitakyushu, Japan.
- “BioSim” – A grid enabled application, Fall Internet2 Member Meeting, Dec 2006, Chicago, IL – 60616
- “Field Marshal Simulation Environment”, ICOPS 2006, Traverse City, MI, 2006.
- “Text Independent Speaker Identification using re-trainable and reusable BPP neural networks”, ICASSP 2002

## OTHER PROJECTS

- Human Fatigue Model scheme. *Developed an ANN based system to predict the fatigue level based on expected “wake” hours. Now being used as a module in a larger simulation environment. (Complete)*
- Part of the collaborative computation Field Marshal project.
- Automatic Configuration system for controlling Particle in Cell (PIC) simulations.

## INTERESTS

- High Performance Computation, Artificial Neural Networks, SVM, Computational Methods, Signal Processing, Algorithm development.
- Active contributor on the online MATLAB/FORTRAN help forums.
- Reading, writing.

## PROFICIENCY

- MATLAB®, FORTRAN, C/C++, Python, VB, MPI
- Long term experience with Win32/Linux